

2-9-2011

# All-optical metamaterial modulators : fabrication, simulation and characterization

Zahyun Ku

Follow this and additional works at: [https://digitalrepository.unm.edu/ece\\_etds](https://digitalrepository.unm.edu/ece_etds)

---

## Recommended Citation

Ku, Zahyun. "All-optical metamaterial modulators : fabrication, simulation and characterization." (2011).  
[https://digitalrepository.unm.edu/ece\\_etds/144](https://digitalrepository.unm.edu/ece_etds/144)

This Dissertation is brought to you for free and open access by the Engineering ETDs at UNM Digital Repository. It has been accepted for inclusion in Electrical and Computer Engineering ETDs by an authorized administrator of UNM Digital Repository. For more information, please contact [disc@unm.edu](mailto:disc@unm.edu).

**Zahyun Ku**

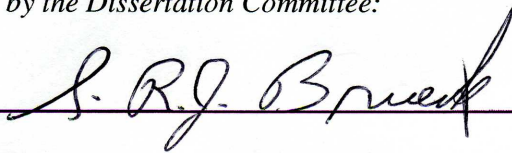
*Candidate*

**Electrical and Computer Engineering**

*Department*

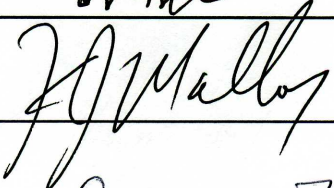
This dissertation is approved, and it is acceptable in quality and form for publication:

*Approved by the Dissertation Committee:*

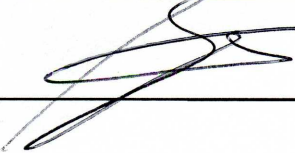
 \_\_\_\_\_, Chairperson

 \_\_\_\_\_

 \_\_\_\_\_

 \_\_\_\_\_

 \_\_\_\_\_

 \_\_\_\_\_

\_\_\_\_\_

\_\_\_\_\_

\_\_\_\_\_

**ALL-OPTICAL METAMATERIAL MODULATORS:  
FABRICATION, SIMULATION AND CHARACTERIZATION**

**BY**

**ZAHYUN KU**

B.S., Physics, Korea University, 1997  
M.S., Physics, Korea University, 1999  
M.S., EE, University of Southern California, 2004

DISSERTATION

Submitted in Partial Fulfillment of the  
Requirements for the Degree of

**Doctor of Philosophy  
Engineering**

The University of New Mexico  
Albuquerque, New Mexico

**December 2010**

*To My Parents, My Wife and My Son*



## ACKNOWLEDGMENTS

First and foremost, I would like to thank my advisor and dissertation chair, Prof. Steve R. J. Brueck, who provides me the great opportunity to pursue my study and complete my dissertation at University of New Mexico. I am deeply indebted to him for his enthusiasm, inspiration, guidance, encouragement, and patience, which helped me during my research and the writing of this dissertation, and for his assistance in my professional development. This dissertation would not have been possible without his support.

I would like to express my gratitude to Dr. Toni Taylor, Dr. Igal Brener, Prof. Mansoor Sheik-Bahae, Prof. Kevin Malloy, and Prof. Sanjay Krishna for their scientific advice and valuable comments on my dissertation.

I greatly appreciate the collaboration and support of my friends and colleagues at Center for High Technology Materials (CHTM), Los Alamos National Lab., and Sandia National Lab. Especially, I thank Dr. Sang Jun Lee (KRISS), Dr. Seung-Chang Lee (CHTM), Dr. Deying Xia (MIT), Dr. Shuang Zhang (University of Birmingham), Dr. Keshav Dani (LANL), Dr. Prashanth Upadhyaya (LANL), and Dr. Rohit Prasankumar (LANL) for kindly and patiently answering my questions. I benefited greatly from discussions with them on various research topics.

Finally, I wish to thank my parents and sister for their unconditional love, constant support and encouragement. And, to my wife Minjung and my son Benjaminn, your anticipation commitment patience and love are the strongest support for the fulfillment of this work.

**ALL-OPTICAL METAMATERIAL MODULATORS:  
FABRICATION, SIMULATION AND CHARACTERIZATION**

**BY**

**ZAHYUN KU**

**ABSTRACT OF DISSERTATION**

Submitted in Partial Fulfillment of the  
Requirements for the Degree of

**Doctor of Philosophy**

**Engineering**

The University of New Mexico  
Albuquerque, New Mexico

**December 2010**

# **All-Optical Metamaterial Modulators: Fabrication, Simulation and Characterization**

by

**Zahyun Ku**

**B.S., Physics, Korea University, 1997**

**M.S., Physics, Korea University, 1999**

**M.S., Electrical Engineering, University of Southern California, 2004**

**Ph.D., Engineering, University of New Mexico, 2010**

## **ABSTRACT**

Artificially structured composite metamaterials consist of sub-wavelength sized structures that exhibit unusual electromagnetic properties not found in nature. Since the first experimental verification in 2000, metamaterials have drawn considerable attention because of their broad range of potential applications. One of the most attractive features of metamaterials is to obtain negative refraction, termed left-handed materials or negative-index metamaterials, over a limited frequency band.

Negative-index metamaterials at near infrared wavelength are fabricated with circular, elliptical and rectangular holes penetrating through metal/dielectric/metal films. All three negative-index metamaterial structures exhibit similar figure of merit; however, the transmission is higher for the negative-index metamaterial with rectangular holes as a result of an improved impedance match with the substrate-superstrate (air-glass) combination.

In general, the processing procedure to fabricate the fishnet structured negative-index metamaterials is to define the hole-size using a polymetric material, usually by lithographically

defining polymer posts, followed by deposition of the constitutive materials and dissolution of the polymer (liftoff processing). This processing (fabrication of posts: multi-layer deposition: liftoff) often gives rise to significant sidewall-angle because materials accumulate on the tops of the posts that define the structure, each successive film deposition has a somewhat larger aperture on the bottom metamaterial film, giving rise to a nonzero sidewall-angle and to optical bianisotropy.

Finally, we demonstrate a nanometer-scale, sub-picosecond metamaterial device capable of over terabit/second all-optical communication in the near infrared spectrum. We achieve a 600 fs device response by utilizing a regime of sub-picosecond carrier dynamics in amorphous silicon and  $\sim 70\%$  modulation in a path length of only 124 nm by exploiting the strong nonlinearities in metamaterials. We identify a characteristic signature associated with the negative index resonance in the pump-probe signal of a fishnet structure. We achieve much higher switching ratios at the fundamental resonance ( $\sim 70\%$ ) relative to the secondary resonance ( $\sim 20\%$ ) corresponding to the stronger negative index at the fundamental resonance. This device opens the door to other compact, tunable, ultrafast photonic devices and applications.

## TABLE OF CONTENT

<b>ACKNOWLEDGMENTS</b> .....	<b>IV</b>
<b>ABSTRACT</b> .....	<b>VI</b>
<b>LIST OF FIGURES</b> .....	<b>XII</b>
<b>LIST OF TABLES</b> .....	<b>XVIII</b>
<b>PUBLICATIONS</b> .....	<b>XIX</b>
<b>CHAPTER 1 INTRODUCTION</b> .....	<b>1</b>
1.1 Concept of Negative-Index Metamaterials .....	2
1.1.1 Categorization of Metamaterials .....	3
1.1.2 Theory of NIMs .....	4
1.1.3 Characteristic of NIMs .....	5
1.1.3.1 Negative Refraction .....	5
1.1.3.2 Dispersive and Dissipative Natures of LHM .....	8
1.1.3.3 Phase velocity, Group velocity and Energy velocity .....	9
1.2 Realization of NIMs .....	12
1.2.1 SRRs and Thin Metal wires .....	13
1.2.1.1 Thin Metal wires for Effective Negative Permittivity .....	13
1.2.1.2 SRRs for Effective Negative Permeability .....	16
1.2.2 Single SRR (U-shaped SRR) .....	18
1.2.3 Cut-wire pairs .....	20
1.2.4 Fishnet structure .....	21
1.3 Outline of the Dissertation .....	23

1.4 References.....	25
<b>CHAPTER 2 FABRICATION.....</b>	<b>28</b>
2.1 Nanofabrication.....	28
2.1.1 Interferometric Lithography.....	28
2.1.2 IL setup .....	28
2.1.3 PR patterning with IL.....	30
2.2 Fabrication of a Single-functional layered Circular/Elliptical Negative-Index Metamaterial .....	31
2.3 Fabrication of a Single-functional layered Fishnet NIM .....	38
2.4 Fabrication of Multi-functional layered NIMs .....	43
2.5 Fabrication of Ultrafast Optical Switching device with NIM.....	45
2.6 References.....	50
<b>CHAPTER 3 COMPARISON OF STRUCTURAL IMPACT ON THE NEGATIVE-     INDEX METAMATERIALS .....</b>	<b>53</b>
3.1 Introduction.....	53
3.2 Design of Circular, Elliptical and Rectangular NIMs.....	54
3.3 Measurement and Simulation .....	56
3.4 Summary .....	63
3.5 References.....	65
<b>CHAPTER 4 BI-ANISOTROPIC EFFECTS DUE TO NON-ZERO SIDEWALL-     ANGLE IN NEGATIVE-INDEX METAMATERIALS .....</b>	<b>67</b>
4.1 Introduction.....	67

4.2 Numerical Demonstration .....	70
4.2.1 Design and Dimensions .....	70
4.2.2 Simulation .....	71
4.2.3 Analysis.....	76
4.3 Experimental Demonstration in Asymmetric medium .....	82
4.3.1 Design and Dimensions .....	82
4.3.2 Measurement, Simulation and Analysis .....	83
4.4 Experimental Demonstration in Symmetric medium .....	88
4.4.1 Design and Dimensions .....	88
4.4.2 Measurement, Simulation and Analysis .....	88
4.5 Summary .....	96
4.5 References.....	97

## **CHAPTER 5 ALL-OPTICAL SWITCHING DEVICE USING A NEGATIVE-INDEX**

<b>METAMATERIAL.....</b>	<b>100</b>
5.1 Introduction.....	100
5.2 First Experimental Demonstration.....	102
5.2.1 Design and Dimensions .....	102
5.2.2 Measurement and Simulation .....	103
5.3 Second Experimental Demonstration .....	111
5.3.1 Design and Dimensions .....	111
5.3.2 Measurement and Simulation .....	112
5.3.3 Pump-Probe Measurement.....	114
5.4 Summary .....	119

5.5 References.....	120
<b>CHAPTER 6 FUTURE WORK .....</b>	<b>123</b>
6.1 Infrared Focal Plane Array integrated with a Surface Plasmonic Structure .....	123
6.1.1 Design and Fabrication of Surface Plasmonic Structure .....	123
6.1.2 Measurement and Simulation to Find an Optimized SP structure .....	125
6.1.3 FPA integrated with SP.....	130
6.1.4 Measurement and Simulation of SP-FPA .....	131
6.2 Polarization-Dependent Dual-band Near-Infrared Metamaterial-Absorber .....	134
6.2.1 Basic idea .....	134
6.2.2 Dimension, Fabrication and SEM images .....	136
6.2.3 Measurement and Simulation .....	139
6.3 References.....	142



## LIST OF FIGURES

Figure 1.1. Classification of normal crystals, metamaterial and photonic crystals .....	3
Figure 1.2. The directions of electric field, magnetic field, wave vector and Poynting vector are illustrated in left-handed and right-handed medium .....	5
Figure 1.3. Schematic view of transmission, reflection and refraction at interface of two different media with positive/positive and positive/negative refractive indices.....	6
Figure 1.4. Schematic view of an array of thin metal wires with geometrical parameters and the direction of electric field along with thin metal wires .....	14
Figure 1.5. The plasma frequency is the function of structural geometry, $p/d$ .....	15
Figure 1.6. Schematic view of an array of SRRs.....	16
Figure 1.7. Real and imaginary parts of the effective permeability.....	17
Figure 1.8. Schematic view and SEM image of single SRR with geometrical parameters: gap, length, width and thickness.....	18
Figure 1.9. The length of single SRR is the function of the resonant wavelength with effective permittivity of three different materials in between the plates .....	20
Figure 1.10. Schematic view and side/top view SEM image of transition from single SRR to cut-wire pairs.....	21
Figure 1.11. Schematic view and SEM image of a fishnet NIM .....	22
Figure 2.1. Experimental arrangements of IL.....	29
Figure 2.2. SEM image of 1D grating in positive-tone PR.....	30
Figure 2.3. SEM images of a periodic circular posts (holes) in positive (negative) PR.....	31

Figure 2.4. Schematic view of fabrication procedure for a single-functional layered circular/elliptical NIM.....	32
Figure 2.5. SEM images of a periodic circular hole PR pattern .....	33
Figure 2.6. SEM images of BARC posts etched by anisotropic O <sub>2</sub> plasma RIE.....	35
Figure 2.7. SEM images of fabricated a single-functional layered circular NIM.....	36
Figure 2.8. SEM images of a periodic elliptical hole PR pattern and an array of circular/elliptical Ti disks atop the BARC layer .....	37
Figure 2.9. SEM images of BARC posts etched by anisotropic O <sub>2</sub> plasma RIE and fabricated elliptical NIM.....	38
Figure 2.10. Schematic view of fabrication procedure for a single-functional layered rectangular NIM.....	39
Figure 2.11. SEM images of fabrication procedure of one-functional layered rectangular NIM and fabricated samples .....	42
Figure 2.12. SEM images of fabrication procedure for multi-functional layered elliptical NIMs and fabricated samples .....	44
Figure 2.13. Schematic view of fabrication procedure for ultrafast optical switching device with a NIM.....	46
Figure 2.14. SEM images of fabrication procedure for ultrafast optical switching device with a NIM.....	48
Figure 3.1. Schematic view and SEM images of NIM structures with circular, elliptical and rectangular holes .....	55
Figure 3.2. FTIR measured/RCWA simulated transmission spectra for circular, elliptical and rectangular NIMs .....	58

Figure 3.3. Calculated effective refractive indices and FOMs for circular, elliptical and rectangular NIMs .....	60
Figure 3.4. Calculated effective impedance and permittivity for circular, elliptical and rectangular NIMs .....	62
Figure 3.5. Calculated effective permeability for circular, elliptical and rectangular NIMs.....	63
Figure 4.1. Schematic view of SWA formation mechanism .....	70
Figure 4.2. Schematic tilted view of the unit cell for 3-functional layered fishnet NIM with SWA with geometrical parameters, polarization and propagation direction.....	71
Figure 4.3. Transmission, reflectances and reflectivity difference depending on the direction of incident wave for one to up to five functional layered fishnet NIMs with SWAs (0°, 4°, 10°, 16°, 20°).....	73
Figure 4.4. Real parts of the effective parameters ( $n$ , $\mu$ ) for one- to five-functional layered fishnet NIMs with SWAs (0°, 4°, 10°, 16°, 20°) .....	77
Figure 4.5. Schematic depicting the electric and magnetic dipoles in an ideal/a realistic fishnet structures with a fabrication-induced SWA .....	78
Figure 4.6. Bi-anisotropic parameter ( $\xi$ ) for one to up to five functional layered fishnet NIMs with SWAs (0°, 4°, 10°, 16°, 20°) .....	79
Figure 4.7. $y$ -component of current density at specific frequency [ $\min\{\text{Re}(\mu_{\text{eff}})\}$ ] for 2, 3 FLs with SWA 0°, 20° .....	80
Figure 4.8. FOMs of 1- to 5-functional layered NIMs as a function of the SWA.....	81
Figure 4.9. Schematic view of structure and dimensions for two FLs elliptical NIM.....	83
Figure 4.10. SEM images of elliptical NIMs with one, two and three FLs .....	84
Figure 4.11. Measured/simulated spectra for eNIMs with one to three FLs .....	85

Figure 4.12. Effective parameters (refractive index, FOM, and permeability) for one to three FLs eNIMs .....	86
Figure 4.13. $\text{Re}(n_{\text{eff}})$ and $\text{Re}(\mu_{\text{eff}})$ in two FLs eNIMs with SWA $0^\circ$ and $13^\circ$ ... ..	87
Figure 4.14. Dimensions of two-functional-layered superstrate-elliptical NIM.....	88
Figure 4.15. Measured/simulated transmission, reflectance, and absorption for superstrate-elliptical NIMs, depending on the propagation direction .....	90
Figure 4.16. $n', \epsilon', \mu', \xi'$ , necessary/sufficient condition for negative refractive index for one- to three-functional-layered s-eNIMs with SWAs ( $4^\circ, 13^\circ, 22^\circ$ ) .....	91
Figure 4.17. $ J_y ,  H_x $ and $ E_x $ at a frequency of $\min[\text{Re}(\mu_{\text{eff}})]$ for one-functional-layered s-eNIM with SWAs ( $0^\circ, 22^\circ$ ) along lines at the edge of cut-wire structure, and $ J_y $ along the lines in edge of thin-metal wire structure .....	93
Figure 4.18. $ J_y ,  H_x $ and $ E_x $ at a frequency of $\min[\text{Re}(\mu_{\text{eff}})]$ for two-functional-layered s-eNIM with SWAs ( $0^\circ, 22^\circ$ ) along lines at the edge of cut-wire structure, and $ J_y $ along the lines in edge of thin-metal wire structure .....	94
Figure 5.1. Diagram and SEM image of fabricated ultrafast optical switching device with a negative-index metamaterial .....	102
Figure 5.2. Experimental/simulated normal incidence transmission spectra.....	104
Figure 5.3. The simulated magnetic field distribution ( $H_x$ ) for eNIM in the $x, y$ plane through the middle of the structure at the corresponding resonances .....	105
Figure 5.4. Comparison of device response for different probe polarization .....	106
Figure 5.5. Comparison of pump-probe signal decay times for the eNIM and an unstructured $\alpha$ -Si film (pump/probe wavelength 550/1180 nm) .....	107
Figure 5.6. eNIM pump-probe signal at different probe wavelength .....	111

Figure 5.7. Schematic view and SEM image of dual-band ultrafast optical switching device with a NIM.....	112
Figure 5.8. Experimental/simulated normal incidence transmission spectra and effective parameters .....	113
Figure 5.9. Pump-probe measurement setup.....	114
Figure 5.10. Measured pump-probe response versus pump-probe delay for different probe wavelengths around shorter/longer wavelength of negative index resonance.....	115
Figure 5.11. Experimental/simulated peak switching ratios at zero pump delay versus probe wavelength .....	116
Figure 5.12. Experimental/simulated normal incidence transmission spectra and effective parameters with polarization direction along the major axis of the ellipses.....	118
Figure 6.1. SEM image of PR pattern and fabricated SP structure.....	124
Figure 6.2. FTIR linear transmission of SP structures with variable pitches .....	125
Figure 6.3. SP mode at each interface (Air/Au or Au/Substrate) .....	126
Figure 6.4. Measured first/second order SP resonance wavelengths and calculated effective refractive index .....	128
Figure 6.5. FTIR measured/RCWA simulated transmission/absorption of 1.79 $\mu\text{m}$ pitch-SP structure and simulated $E_z$ field distribution.....	129
Figure 6.6. Quantum dot infrared photodetector (QDIP) structure with the absorption region consisting of 20 stacks of InAs QDs.....	130
Figure 6.7. Schematic view of the SP structure integrated with DWELL-FPA .....	131

Figure 6.8. Spectral response of the two halves of the SP-FPA, difference of spectral responses as well as simulated absorption curve and infrared image of the blackbody below, near, close, and above the (1,0) or (1,1) resonance.....	132
Figure 6.9. Enhancement of the spectral response owing to SP structure versus wavelength.....	133
Figure 6.10. Schematic view of proposed structure and the equivalent <i>LC</i> circuit .....	135
Figure 6.11. Sequence of schematic views of a changing shape and thickness of MAA depending on RIE processing .....	136
Figure 6.12. Schematic tilted view of the MAA with geometrical parameters .....	137
Figure 6.13. Schematic view of fabrication procedure .....	138
Figure 6.14. SEM images of MAA depending on O <sub>2</sub> plasma RIE processing .....	139
Figure 6.15. Measured/simulated reflectance spectra for MMA with polarization 0°, 90° and O <sub>2</sub> RIE processing .....	140

## LIST OF TABLES

Table 3.1. The geometrical parameters of circular, elliptical and rectangular NIMs .....	56
Table 4.1. NIM geometrical parameters .....	71
Table 6.1. MMA geometrical parameters .....	137

## PUBLICATIONS<sup>1</sup>

### Press Coverage

---

“Going negative for a fast switch”, *Photonics Spectra*, Nov. 2009

“Faster and smaller switches”, *Research Highlights in Nature Photonics* **3**, 606 2009

“New Highlights: Ultrafast communication, tracking *in-situ* ion irradiation damage, tracking malware”, *LANL today*, Los Alamos National Laboratory

### Publications

---

#### Published

- i. Deying Xia, Dong Li, Zahyun Ku, Ying Luo and S. R. J. Brueck, "Top-down Approaches to the Formation of Silica Nanoparticle Patterns", *Langmuir* 23(10) 5377-5385 (2007)
- ii. Zahyun Ku and S. R. J. Brueck, "Comparison of negative refractive index materials with circular, elliptical and rectangular holes", *Optics Express* **15**, 4515-4522 (2007)
- iii. Deying Xia, Zahyun Ku, Dong Li and S. R. J. Brueck, "Formation of Hierarchical Nanoparticle Pattern Arrays with Colloidal Lithography and Two-Step Self-Assembly: Microspheres atop Nanospheres", *Chemistry of Materials* 20, 1847-1854 (2008)
- iv. Zahyun Ku, Jingyu Zhang and S. R. J. Brueck, "Bi-anisotropy of multiple-layer fishnet negative-index metamaterials due to angled sidewalls", *Optics Express* **17**, 6782-6789 (2009)
- v. Zahyun Ku and S. R. J. Brueck, "Experimental Demonstration of Sidewall-Angle Induced Bi-anisotropy in Multiple-Layer Negative-Index Metamaterials", *Applied Physics Letter* **94**, 153107 (2009)
- vi. S. C. Lee, Z. Ku, W.-Y. Jang, J. H. Kim, C. Hains, S. Krishna and S. R. J. Brueck, "Mid-infrared transmission through a subwavelength circular aperture coupled to a surrounding concentric metal grating by surface plasmon excitation", *Phys. Status Solidi C* **6**, No. S1, S175-S178 (2009)
- vii. Zahyun Ku, Keshav M. Dani, Prashanth C. Upadhyaya and S. R. J. Brueck, "Bi-anisotropic negative-index metamaterial embedded in a symmetric medium", *Journal of the Optical Society of America B* **26**, B34-B38 (2009)
- viii. Keshav M. Dani, Zahyun Ku, Prashanth C. Upadhyaya, Rohit P. Prasankumar, S. R. J. Brueck and Antoinette J. Taylor, "Subpicosecond Optical Switching with a Negative Index Metamaterial", *Nano Letters* **9**, 3565-3569 (2009)

---

<sup>1</sup> Publications (journal and meeting presentation) directly relevant to this dissertation are typed in bold.

<sup>†</sup> Contributed equally.



- ix. J. H. Kim, C. G. Christodoulou, Z. Ku, C.-Y. Lin, Y.-C. Xin, N. A. Naderi and L. F. Lester, "Hybrid Integration of a bowtie slot antenna and a quantum dot mode-locked laser", *IEEE Antennas and Wireless Propagation Letters* 8, 1337-1340 (2009)
- x. John Montoya, Ajit Barve, Rajeev Sheno, Mikhail Naydenkov, Hasul Kim, Zahyun Ku, S. R. J. Brueck, Sanjay Krishna, Sang Jun Lee and Sam Kyu Noh, "Backside illuminated infrared detectors with plasmonic resonators", *Proceedings of SPIE* 7660, 76603P (2010)
- 

#### Accepted

- xi. Deying Xia, Zahyun Ku, Seung-Chang Lee and S. R. J. Brueck, "Nanostructures and Functional Materials Fabricated by Interference Lithography", Accepted for publication in *Advanced Materials* (Review Paper)
- xii. Svyatoslav Smolev, Zahyun Ku, S. R. J. Brueck, Igal Brener, Michael B. Sinclair, Gregory A. Ten Eyck, W. L. Langston and Lorena I. Basilio, "Resonant Coupling to a Dipole Absorber inside a Metamaterial: Anti-crossing of the Negative Index Response", Accepted for publication in *Journal of Vacuum Science and Technology B*
- 

#### Submitted

- xiii. **Sang Jun Lee<sup>†</sup>, Zahyun Ku<sup>†</sup>, Ajit Barve, John Montoya, Woo-Yong Jang, S. R. J. Brueck, Mani Sundaram, Axel Reisinger, Sanjay Krishna and Sam Kyu Noh, "A Monolithically Integrated Plasmonic Infrared Quantum Dot Camera"**
- xiv. Svyatoslav Smolev, Zahyun Ku, Steven R. J. Brueck, Igal Brener, Michael B. Sinclair, Gregory A. Ten Eyck, W. L. Langston and Lorena I. Basilio, "Resonant Coupling to a Dipole Absorber Inside a Metamaterial: Anti-crossing of the Negative Index Response"
- 

#### Preparation

- xv. **Zahyun Ku<sup>†</sup>, Jiangfeng Zhou<sup>†</sup> and S. R. J. Brueck, "Polarization-dependent Dual-band Near-infrared Metamaterial Absorber"**
- xvi. **Keshav M. Dani, Zahyun Ku, Prashanth C. Upadhy, Rohit P. Prasankumar, S. R. J. Brueck and Antoinette J. Taylor, "Dual-band ultrafast optical switching device with negative-index metamaterial"**
- xvii. Zahyun Ku, Keshav M. Dani, Prashanth C. Upadhy, Rohit P. Prasankumar, Antoinette J. Taylor and S. R. J. Brueck, "Analysis of Metamaterials with gap surface plasmon polaritons"
- xviii. J. Zhang, Zahyun Ku, D. Xia, L. Wang, S. Krishna, M. Sheik-Bahae and S. R. J. Brueck, "Enhanced second harmonic generation and photoluminescence from plasmon-coupled GaAs hole arrays"

## Meeting Presentation

---

- i. Deying Xia, Dong Li, Ying Luo, Zahyun Ku, Abani Biswas and S. R. J. Brueck, "Lithographically Templated and Defined Surface Structures of Nanoparticle Films and Arrays--A Combination of "Bottom-Up" and "Top-Down" Methods", *AVS New Mexico Chapter Meeting*, Albuquerque, NM 2006
- ii. Zahyun Ku and S. R. J. Brueck, "Comparison of negative refractive index materials with circular, elliptical and rectangular holes", *The OSA student chapter at UNM*, Albuquerque, NM 2007
- iii. Zahyun Ku and S. R. J. Brueck, "Experimental Comparison of Circular, Elliptical and Rectangular (Fishnet) Negative-Index Metamaterials", *QELS*, Baltimore, MD 2007
- iv. Deying Xia, Zahyun Ku, Dong Li and S. R. J. Brueck "Formation of Hierarchical Nanoparticle Patterns with Colloidal Lithography and Two-Step Self-Assembly", *EIPBN*, Denver, CO 2007
- v. S. C. Lee, Z. Ku, W.-Y. Jang, C. Hains, S. Krishna and S. R. J. Brueck, "Mid-infrared transmission through a single subwavelength circular aperture coupled to a surrounding concentric grating by surface plasmonic excitation", *ICOOPMA*, Edmonton, Canada 2008
- vi. J. H. Kim, C. G. Christodoulou, L. F. Lester, Y. Xin, N. A. Naderi and Z. Ku, "Quantum-Dot Laser Coupled Bowtie Antenna", *IEEE International Symposium on Antennas and Propagation and USNC/URSI National Radio Science Meeting*, San Diego, CA 2008
- vii. Jing Chen, Zahyun Ku, A. Smolyakov and Kevin J. Malloy, "Experimental verification of free space coupling to a novel leaky mode of a finite planar metal-insulator-metal plasmonic waveguide", *SPIE Symposium on NanoScience + Engineering*, San Diego, CA 2008
- viii. Zahyun Ku, Keshav M. Dani, Prashanth C. Upadhyaya, Rohit P. Prasankumar, D. Talbayev, Antoinette J. Taylor and S. R. J. Brueck, "High Speed Metamaterial Modulator", *Optical Metamaterials Workshop* (Funded by the National Science Foundation), Estes Park, CO 2008
- ix. Keshav M. Dani, Prashanth C. Upadhyaya, Rohit P. Prasankumar, Antoinette J. Taylor, Zahyun Ku and S. R. J. Brueck, "Sub-picosecond Optical Switching with a Negative Index Metamaterial", *The 2nd European Topical Meeting on Nanophotonics and Metamaterials (NANOMETA)*, Tirol, Austria 2009
- x. R. P. Prasankumar, Z. Ku, A. Gin, P. C. Upadhyaya, S. R. J. Brueck, and A. J. Taylor, "Ultrafast Optical Wide Field Microscopy", *CLEO*, Baltimore, MD 2009
- xi. Keshav M. Dani, Zahyun Ku, Prashanth C. Upadhyaya, Rohit P. Prasankumar, S. R. J. Brueck and Antoinette J. Taylor, "Sub-picosecond Optical Switching in the near-Infrared using Negative Index Metamaterials", *IQEC*, Baltimore, MD 2009
- xii. Rohit P. Prasankumar, Zahyun Ku, Aaron V. Gin, Prashanth C. Upadhyaya, Steven R. J. Brueck and Antoinette J. Taylor, "Ultrafast Optical Wide Field Microscopy", *Advances in Optical Sciences: OSA optics & Photonic Congress*, Honolulu, HI 2009

- xiii. Igal Brener, Hou-Tong Chen, Xomalin G. Peralta, Andrew Strikwerda, Richard D. Averitt, W. Padilla, Evgenya Smirnova, Abul K. Azad, Antoinette J. Taylor, John O'Hara, Steven Brueck, K. M. Dani, Zahyun Ku, Prashanth C. Upadhy, Rohit P. Prasankumar, Michael Cich, Clark Highstrete, Mark Lee, W. Liam, D. Mittleman and M. Wanke, "Active and Passive Metamaterials Research at CINT", *Nanoscale Science Research Centers (NSRCs) Contractors' Meeting*, Annapolis, MD 2009
- xiv. Zahyun Ku, Svyatoslav, Jingyu Zhang, S. R. J. Brueck, K. M. Dani, Prashanth C. Upadhy, Rohit P. Prasankumar, Antoinette J. Taylor, Igal Brener and M. Sinclair, "Linear and Nonlinear Properties of Large-Area Metamaterials", *Nanoscale Science Research Centers (NSRCs) Contractors' Meeting*, Annapolis, MD 2009
- xv. Igal Brener, Slava Smolev, Zahyun Ku, Steve Brueck, Michael Sinclair, Greg Ten-Eyck, William Langston and Lorena Basilio, "Resonant coupling to a dipole absorber inside a metamaterial: anti-crossing of the negative index response", *3rd International Congress on Advanced Electromagnetic Materials in Microwaves and Optics*, London, UK 2009
- xvi. Svyatoslav Smolev, Zahyun Ku, Steven R. J. Brueck, Igal Brener, Michael Sinclair, Gregory Ten-Eyck, W. Langston and L. Basilio, "Hybridization of the Negative Index Response by Resonant Coupling to a Dipole Absorber inside a Metamaterial", *QELS*, San Jose, CA 2010
- xvii. **Zahyun Ku, Keshav M. Dani, Prashanth C. Upadhy, Rohit P. Prasankumar, Antoinette J. Taylor and S. R. J. Brueck, "Ultrafast Dual-band Optical Switching Device with a Negative-Index Metamaterial", *QELS*, San Jose, CA 2010**
- xviii. Svyatoslav Smolev, Zahyun Ku, Steven Brueck, Igal Brener, Michael Sinclair, Gregory Ten Eyck, W Langston and Lorena Basilio, "Experimental Demonstration of Resonant Coupling to a Dipole Absorber Inside a Metamaterial: Hybridization of the Negative Index Response", *54<sup>th</sup> International Conference on Electron, Ion, Photon beam technology & Nanofabrication*, Anchorage, AK 2010
- xix. **Keshav M. Dani, Zahyun Ku, Prashanth C. Upadhy, Rohit P. Prasankumar, S. R. J. Brueck and Antoinette J. Taylor, "Ultrafast Pump-Probe Spectroscopy of a Dual-Band Negative-Index Metamaterial", *17<sup>th</sup> International Conference on Ultrafast Phenomena (UP)*, Snowmass, CO 2010**
- xx. S. J. Lee, J. Montoya, Z. Ku, N. Gautan, M. Naydenkov, E. Plis, Y. Sharma, J. O. Kim, S. R. J. Brueck, S. Krishna and S. K. Noh, "Response Selective in type-II InAs/GaSb superlattice infrared photo-detector with surface plasmonic structure", *30<sup>th</sup> International Conference on the Physics of Semiconductors*, Seoul, Korea 2010
- xxi. S. Smolev, Zahyun Ku, S. R. J Brueck, I. Brener, M.B. Sinclair, G. A. Ten Eyck, W. L. Langston and L.I. Basilio, "Magnetic Hybridization of an Electric Dipole Resonance: Anti-Crossing of a Metamaterial Negative Index Response", *International Workshop on Electromagnetic Metamaterials IV*, Santa Ana Pueblo, NM 2010

# Chapter 1 Introduction

Light is, in a sense, ‘one-handed’ when interacting with atoms of conventional materials. This is because from the two field components of light – electric and magnetic – only the electric ‘hand’ efficiently probes the atoms of a material, whereas the magnetic component remains relatively unused because the interaction of atoms with the magnetic field component of light is normally weak [1].

For the ultimate control of light, one needs to control both the electric and the magnetic components of the electromagnetic light wave. To achieve this control, normally one would think about modifying the microscopic electric and magnetic fields in a material. However, in most cases it is easier to average over the atomic scale and consider the material to be a homogeneous medium characterized by the electric permittivity  $\epsilon$  and the magnetic permeability  $\mu$ . These two quantities describe the electromagnetic response of a given material. More specifically, Veselago showed nearly 40 years ago that the combination  $\text{Re}(\epsilon) < 0$  and  $\text{Re}(\mu) < 0$  leads to a negative refractive index,  $\text{Re}(n) < 0$  [2,3].

His idea remained obscure because no such natural materials were known to exist at any frequency. Although electric resonances with  $\text{Re}(\epsilon) < 0$  do occur up to the visible and beyond, magnetic resonances typically die out at microwave frequencies. Moreover, the electric and magnetic resonances would need to overlap in frequency, which seemed improbable. However, artificial materials with rationally designed properties can allow both field components of light to be coupled to man-made atoms, enabling entirely new optical properties and exciting applications with such ‘two-handed’ light [1].

The word ‘meta’ means ‘beyond’ in Greek, and in this sense the name of ‘metamaterials’ refers to ‘beyond conventional materials’. Metamaterials are designed to have the structure that provides the optical properties not found in nature and thus metamaterials are expected to open a new gateway to unprecedented electromagnetic properties and functionality unattainable from naturally occurring materials [4-7]. One of the most exciting opportunities for metamaterials is the development of negative-index metamaterials (NIMs). These NIMs bring the concept of refractive index into a new domain of exploration and thus promise to create entirely new prospects for manipulating light, with revolutionary impacts on present-day optical technologies. Furthermore, the intense interest has been led by first demonstration exhibiting a negative index of refraction over a band of microwave frequencies [8,9].

## 1.1 Concept of Negative-Index Metamaterials

The term “left-handed material” (LHM) was first introduced by Veselago [3] in 1968, who predicted there exists such a medium in which the electric field ( $\vec{E}$ ), the magnetic field ( $\vec{H}$ ) and the wave vector ( $\vec{k}$ ) form a left-handed orthogonal set. The left-handed materials (LHMs), which in a wider sense, are also referred to as NIMs and negative refractive index materials (NRIs), must satisfy either sufficient condition,  $\text{Re}(\epsilon) < 0$  and  $\text{Re}(\mu) < 0$  or necessary condition,  $\text{Re}(\epsilon) \cdot \text{Im}(\mu) + \text{Re}(\mu) \cdot \text{Im}(\epsilon) < 0$  to achieve the negative refractive index over a common frequency band, where  $\epsilon$  and  $\mu$  are the complex permittivity and permeability.

### 1.1.1 Categorization of Metamaterials

The wavelength of light ( $\lambda$ ) is on the order of the lattice constants ( $a$ ) of a photonic crystal ( $\lambda a \sim 1$ ), whereas the wavelength is an order of magnitude much greater than the lattice constants of normal crystals ( $\lambda a \gg 1$ ) as shown in Fig. 1.1. As a result, the light field effectively averages over these normal crystals and sees an effective homogeneous medium [10].

Metamaterials lie in-between these two limits. They are artificial periodic structures with lattice constants that are still smaller than the wavelength of light ( $\lambda a \gg 1$  in radio frequency and  $\lambda a \sim 2$  in near infrared frequency regime) as shown in Fig. 1.1. Similarly, the light field again “sees” an effective homogeneous material. The “atoms”, however, are functional building blocks which are composed of many real atoms (mostly metallic). This allows for tailoring their electromagnetic properties by design in ways that would not be possible with real atoms, hence, for example, allowing realizing electric as well as magnetic dipoles at optical frequencies [10].

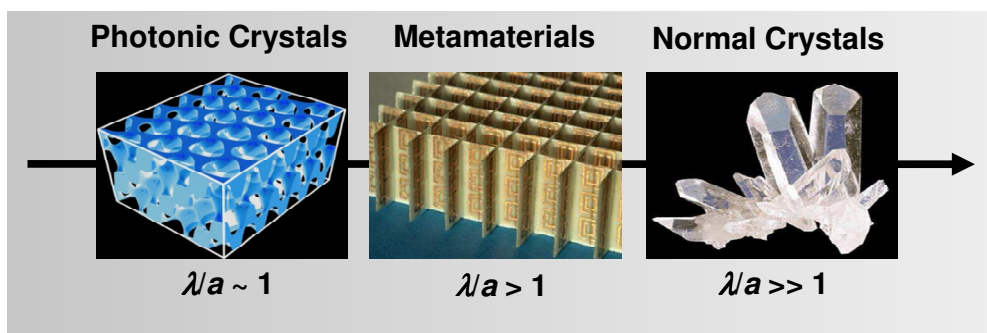


Fig. 1.1 Classification of normal crystals, metamaterials and photonic crystals by the ratio of wavelength of light to lattice constants ( $\lambda a$ ).

### 1.1.2 Theory of NIMs

In source-free ( $\vec{J} = \rho = 0$ ) homogeneous isotropic media, Maxwell's equations become

$$\begin{aligned}\nabla \times \vec{E} &= -\frac{\partial \vec{B}}{\partial t} \\ \nabla \times \vec{H} &= \frac{\partial \vec{D}}{\partial t} \\ \nabla \cdot \vec{H} &= 0 \\ \nabla \cdot \vec{E} &= 0\end{aligned}\tag{1.1}$$

and the constitutive relations are

$$\begin{aligned}\vec{B} &= \mu \vec{H} \\ \vec{D} &= \epsilon \vec{E}\end{aligned}\tag{1.2}$$

Maxwell's equations in Eq. (1.1) and vector identity ( $\nabla \times \nabla \times \vec{A} = \nabla(\nabla \cdot \vec{A}) - \nabla^2 \vec{A}$ ) are used to find the solution of plane wave equation, which is proportional to  $e^{i(\vec{k} \cdot \vec{r} - \omega t)}$ . Then the Maxwell's equations in Eq. (1.1) and (1.2) can be written as

$$\begin{aligned}\vec{k} \times \vec{E} &= \omega \mu \vec{H} \\ \vec{k} \times \vec{H} &= -\omega \epsilon \vec{E}\end{aligned}\tag{1.3}$$

It can be seen from Eq. (1.3) that  $\vec{E}$ ,  $\vec{H}$  and  $\vec{k}$  form a left-handed relation when both real parts of permittivity and permeability are negative. Thus, this unconventional material is called a left-handed material [3].

The Poynting vector ( $\vec{S}$ ) is given by  $\vec{S} = \vec{E} \times \vec{H}$ , which gives us the direction of energy flow. The Poynting vector always forms a right-handed coordinate system with  $\vec{E}$  and  $\vec{H}$ , i.e.  $\vec{S}$  is independent on the signs of  $\epsilon$  and  $\mu$ . Therefore, in a right-handed medium, the wave vector

$(\vec{k})$  is in the same direction of the energy flow ( $\vec{S}$ ), however, in a left-handed medium the wave vector ( $\vec{k}$ ) is in the opposite direction of the energy flow ( $\vec{S}$ ) as shown in Fig. 1.2.

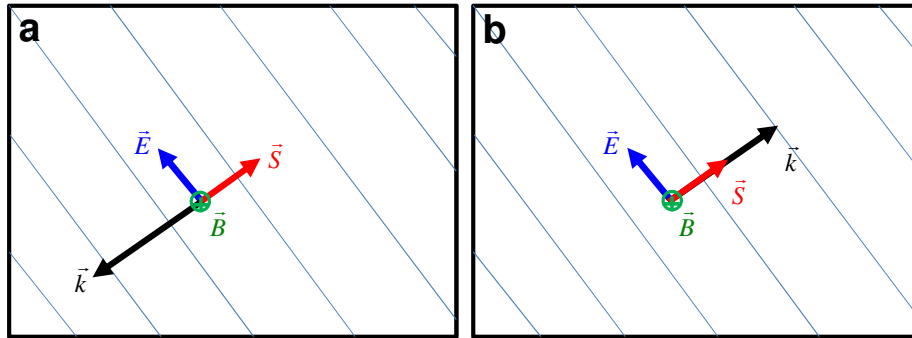


Fig. 1.2 The directions of electric field ( $\vec{E}$ ), magnetic field ( $\vec{H}$ ), wave vector ( $\vec{k}$ ) and Poynting vector ( $\vec{S}$ ) are illustrated in (a) left-handed. (b) right-handed medium, respectively. Specifically speaking,  $\vec{k} \times \vec{E} \parallel \vec{B}$  and  $\vec{S} = \vec{E} \times \vec{H} \parallel (\pm)\vec{k}$ , where  $- (+)$  sign represents the left (right)-handed material.

### 1.1.3 Characteristics of NIMs

#### 1.1.3.1 Negative Refraction

The transmission, reflection and refraction of light at an interface between two media of different positive refractive index ( $n_1 > 0, n_2 > 0$ ) are basic phenomena in optics as shown in Fig. 1.3 (a). These phenomena are well determined by Snell's law and Fresnel formula [11].



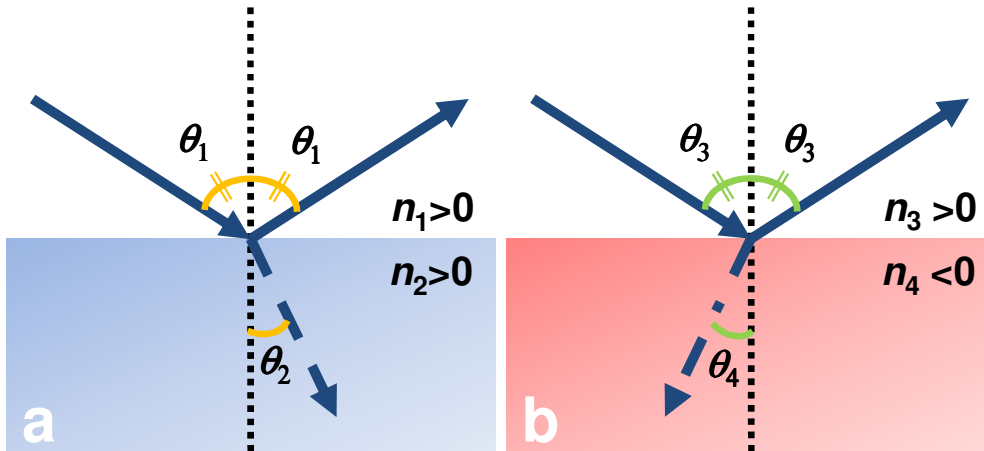


Fig. 1.3 Schematic view of transmission, reflection and refraction at interface of two different media with (a) positive/positive refractive indices ( $n_1, n_2 > 0$ ). (b) positive/negative refractive indices ( $n_3 > 0, n_4 < 0$ ).

As shown in Fig. 1.3 (a), let's consider incident and outgoing media with positive refractive indices ( $n_1 > 0, n_2 > 0$ ). As usual, the refracted light is bent on the opposite side of the surface normal away from the incident light, so that the momentum along the interface is conserved. On the other hand, Fig. 1.3 (b) shows that the refracted light is bent on the same side of surface normal from the incident light in the incident/outgoing media with positive/negative refractive index ( $n_3 > 0, n_4 < 0$ ), resulting from Snell's law below.

$$\frac{\sin(\theta_3)}{\sin(\theta_4)} = \frac{n_3}{n_4} = \frac{\sqrt{\epsilon_3 \cdot \mu_3}}{-\sqrt{\epsilon_4 \cdot \mu_4}} \quad (1.4)$$

where  $n_3, \epsilon_3$  and  $\mu_3$  are the refractive index, permittivity and permeability in the right-handed medium, respectively and  $n_4, \epsilon_4$  and  $\mu_4$  are corresponding quantities in the left-handed medium.

The refractive index ( $n$ ) is given by  $n^2 = \varepsilon \cdot \mu$  for an isotropic medium and can be written as

$$\begin{aligned} n^2 &= (n' + in'')^2 \\ &= (n'^2 - n''^2) + i(2n' \cdot n'') \end{aligned} \quad (1.5)$$

where  $n'$ ,  $n''$  are the real, imaginary part of complex refractive index, respectively. In addition, the complex refractive index ( $n$ ) can be written as

$$\begin{aligned} n^2 &= \varepsilon \cdot \mu \\ &= (\varepsilon' + i\varepsilon'') \cdot (\mu' + i\mu'') \\ &= \varepsilon' \cdot \mu' - \varepsilon'' \cdot \mu'' + i(\varepsilon' \cdot \mu'' + \varepsilon'' \cdot \mu') \end{aligned} \quad (1.6)$$

where  $\varepsilon'$  ( $\mu'$ ) and  $\varepsilon''$  ( $\mu''$ ) are the real, imaginary part of complex permittivity (permeability).

By equating the real and imaginary parts of Eq. (1.5) and (1.6), we get

$$\begin{aligned} \text{Re}[n^2 = \varepsilon\mu]: n'^2 - n''^2 &= \varepsilon' \cdot \mu' - \varepsilon'' \cdot \mu'' \\ \text{Im}[n^2 = \varepsilon\mu]: 2 \cdot n' \cdot n'' &= \varepsilon' \cdot \mu'' + \varepsilon'' \cdot \mu' \end{aligned} \quad (1.7)$$

The necessary condition ( $\varepsilon' \cdot \mu'' + \varepsilon'' \cdot \mu'$ ) to be negative refractive index ( $n' < 0$ ) solely determines the sign of real part of complex refractive index due to the causality ( $n'' > 0$ ). Moreover, there is another causality:  $\xi' > 0$ , where  $\xi$  (impedance) of a medium is defined

$$\text{as } \xi = \xi' + i\xi'' = \sqrt{\frac{\mu}{\varepsilon}}.$$

### 1.1.3.2 Dispersive and Dissipative Natures of LHM

The negative values of  $\epsilon$  and  $\mu$  can be realized simultaneously, only if the material has frequency dispersion. This can be seen immediately from the formula of the energy density of nondispersive media,

$$W = \epsilon E^2 + \mu H^2 \quad (1.8)$$

If  $\epsilon < 0$  and  $\mu < 0$ , the energy density ( $W$ ) would be negative. When there is frequency dispersion, i.e.  $\epsilon = \epsilon(\omega)$  and  $\mu = \mu(\omega)$ , the total energy density [12,13] is given by

$$W = \frac{\partial(\omega\epsilon)}{\partial\omega} \cdot E^2 + \frac{\partial(\omega\mu)}{\partial\omega} \cdot H^2 \quad (1.9)$$

$W$  is always positive if  $\frac{\partial(\omega\epsilon)}{\partial\omega} > 0$  and  $\frac{\partial(\omega\mu)}{\partial\omega} > 0$ . This clearly indicates that  $\epsilon$  and  $\mu$  can be simultaneously negative, given the medium is frequency dispersive and  $\epsilon + \omega \frac{\partial\epsilon}{\partial\omega} > 0$ ,  $\mu + \omega \frac{\partial\mu}{\partial\omega} > 0$  are satisfied. Therefore, NIMs must be dispersive.

Moreover, a medium with frequency dispersion is always dissipative. Following the causality principal, the real and imaginary parts of the permittivity [ $\epsilon(\omega) = \epsilon'(\omega) + i\epsilon''(\omega)$ ], are related by the Kramers-Kronig relations [11,13]:

$$\begin{aligned} \text{Re} \left\{ \frac{\epsilon(\omega)}{\epsilon_0} \right\} &= 1 + \frac{2}{\pi} P \int_0^\infty \frac{\omega' \text{Im} \frac{\epsilon(\omega')}{\epsilon_0}}{\omega'^2 - \omega^2} d\omega' \\ \text{Im} \left\{ \frac{\epsilon(\omega)}{\epsilon_0} \right\} &= -\frac{2\omega}{\pi} P \int_0^\infty \frac{\left[ \text{Re} \frac{\epsilon(\omega')}{\epsilon_0} - 1 \right]}{\omega'^2 - \omega^2} d\omega' \end{aligned} \quad (1.10)$$

where  $P$  stands for the principal value of the integration and is derived from

$$\frac{\varepsilon(\omega)}{\varepsilon_0} = 1 + \frac{1}{\pi i} P \int_{-\infty}^{\infty} \frac{\left[ \frac{\varepsilon(\omega')}{\varepsilon_0} - 1 \right]}{\omega' - \omega} d\omega' \quad (1.11)$$

Taking the real and imaginary part of Eq. (1.11),

$$\begin{aligned} \operatorname{Re} \left\{ \frac{\varepsilon(\omega)}{\varepsilon_0} \right\} &= \operatorname{Re} \left\{ 1 + \frac{1}{\pi i} P \int_{-\infty}^{\infty} \frac{\left[ \frac{\varepsilon(\omega')}{\varepsilon_0} - 1 \right]}{\omega' - \omega} d\omega' \right\} = 1 + \frac{1}{\pi} P \int_{-\infty}^{\infty} \frac{\operatorname{Im} \frac{\varepsilon(\omega')}{\varepsilon_0}}{\omega' - \omega} d\omega' \\ &= 1 + \frac{2}{\pi} P \int_0^{\infty} \frac{\omega' \operatorname{Im} \frac{\varepsilon(\omega')}{\varepsilon_0}}{\omega'^2 - \omega^2} d\omega' \\ \operatorname{Im} \left\{ \frac{\varepsilon(\omega)}{\varepsilon_0} \right\} &= \operatorname{Im} \left\{ 1 + \frac{1}{\pi i} P \int_{-\infty}^{\infty} \frac{\left[ \frac{\varepsilon(\omega')}{\varepsilon_0} - 1 \right]}{\omega' - \omega} d\omega' \right\} = -\frac{1}{\pi} P \int_{-\infty}^{\infty} \frac{\left[ \operatorname{Re} \frac{\varepsilon(\omega')}{\varepsilon_0} - 1 \right]}{\omega' - \omega} d\omega' \\ &= -\frac{2\omega}{\pi} P \int_0^{\infty} \frac{\left[ \operatorname{Re} \frac{\varepsilon(\omega')}{\varepsilon_0} - 1 \right]}{\omega'^2 - \omega^2} d\omega' \end{aligned}$$

The real and imaginary parts of permeability  $[\mu(\omega) = \mu'(\omega) + i\mu''(\omega)]$  follow the same relations.

Since the imaginary parts of the permittivity, permeability and the refractive index always coexist with the real parts in dispersive media, the left-handed material must be dissipative.

### 1.1.3.3 Phase velocity, Group velocity and Energy velocity

There are three velocities: phase velocity ( $\vec{v}_p$ ), energy velocity ( $\vec{v}_e$ ) and group velocity ( $\vec{v}_g$ ). Using the same definition as for right-handed medium, the phase velocity ( $\vec{v}_p$ ) in left-handed medium is given by

$$\vec{v}_p = \frac{\omega}{|\vec{k}|} \hat{k} \quad (1.12)$$

where  $\hat{k}$  is the unit vector along  $\vec{k}$  direction. The group velocity is defined as

$$\vec{v}_g = \frac{d\omega}{d|\vec{k}|} \hat{k} \quad (1.13)$$

The relation between phase velocity ( $\vec{v}_p$ ) and group velocity ( $\vec{v}_g$ ) can be written as

$$\vec{v}_g = \frac{d\omega}{d|\vec{k}|} \hat{k} = c_0 \left[ \frac{1}{|n| + \omega \frac{d|n|}{d\omega}} \right] \hat{k} = \frac{c_0}{|n|} \left[ \frac{1}{1 + \frac{\omega}{|n|} \frac{d|n|}{d\omega}} \right] \hat{k} = \frac{\vec{v}_p}{1 + \frac{\omega}{|n|} \frac{d|n|}{d\omega}} = \frac{\vec{v}_p}{\alpha} \quad (1.14)$$

where  $|\vec{k}| = \frac{\omega}{c_0} |n| \rightarrow \frac{d|\vec{k}|}{d\omega} = \frac{1}{c_0} \frac{d}{d\omega} (\omega \cdot |n|) = \frac{1}{c_0} \left( |n| + \omega \frac{d|n|}{d\omega} \right)$  and  $\alpha = 1 + \frac{\omega}{|n|} \cdot \frac{d|n|}{d\omega}$ . Next, we will

prove that  $\alpha$  has the same sign as  $n$ .

$$\begin{aligned} \alpha &= 1 + \frac{\omega}{|n|} \frac{d|n|}{d\omega} = 1 + \frac{d \ln |n|}{d \ln \omega} \\ &\left( \because \frac{d \ln |n|}{d \ln \omega} = \frac{d \ln |n|}{d |n|} \cdot \frac{d |n|}{d \omega} \cdot \frac{d \omega}{d \ln \omega} = \frac{1}{|n|} \cdot \frac{d |n|}{d \omega} \cdot \frac{1}{1/\omega} = \frac{\omega}{|n|} \cdot \frac{d |n|}{d \omega} \right) \\ &= 1 + \frac{d \ln |\sqrt{\epsilon \mu}|}{d \ln \omega} = 1 + \frac{1}{2} \cdot \frac{d \ln |\epsilon \mu|}{d \ln \omega} = 1 + \frac{1}{2} \cdot \left( \frac{d \ln |\epsilon|}{d \ln \omega} + \frac{d \ln |\mu|}{d \ln \omega} \right) \\ &= 1 + \frac{1}{2} \cdot \left( \frac{\omega}{\epsilon} \cdot \frac{d \epsilon}{d \omega} + \frac{\omega}{\mu} \cdot \frac{d \mu}{d \omega} \right) = \frac{1}{2} \left( 1 + \frac{\omega}{\epsilon} \cdot \frac{d \epsilon}{d \omega} \right) + \frac{1}{2} \left( 1 + \frac{\omega}{\mu} \cdot \frac{d \mu}{d \omega} \right) \\ &= \frac{1}{2 \epsilon} \left( \epsilon + \omega \cdot \frac{d \epsilon}{d \omega} \right) + \frac{1}{2 \mu} \left( \mu + \omega \cdot \frac{d \mu}{d \omega} \right) \end{aligned} \quad (1.15)$$

From the equation in section 1.1.3.1, it can be obtained that

$$1 + \frac{\omega}{\varepsilon} \cdot \frac{d\varepsilon}{d\omega} > 0, \quad 1 + \frac{\omega}{\mu} \cdot \frac{d\mu}{d\omega} > 0 \text{ for } \varepsilon > 0, \mu > 0 \quad (1.16)$$

$$1 + \frac{\omega}{\varepsilon} \cdot \frac{d\varepsilon}{d\omega} < 0, \quad 1 + \frac{\omega}{\mu} \cdot \frac{d\mu}{d\omega} < 0 \text{ for } \varepsilon < 0, \mu < 0 \quad (1.17)$$

Finally, the relation between phase velocity ( $\vec{v}_p$ ) and group velocity ( $\vec{v}_g$ ) depend on the sign of

$1 + \frac{\omega}{|n|} \frac{d|n|}{d\omega}$  as follows [14].

$$1 + \frac{\omega}{|n|} \frac{d|n|}{d\omega} > 0, \quad n > 0 \quad (\varepsilon > 0, \mu > 0) \quad (1.18)$$

$$1 + \frac{\omega}{|n|} \frac{d|n|}{d\omega} < 0, \quad n < 0 \quad (\varepsilon < 0, \mu < 0) \quad (1.19)$$

Therefore, one can obtain  $\vec{v}_g = \frac{\vec{v}_p}{\alpha}$ , where  $\alpha$  has the same sign as  $n$ . It implies that  $\vec{v}_p$  and  $\vec{v}_g$  are parallel in the right-handed medium and are anti-parallel in the left-handed medium.

The energy velocity ( $\vec{v}_e$ ) is given by  $\vec{v}_e = \frac{\vec{S}}{\bar{\omega}}$ , where

$$\begin{aligned} \vec{S} &= \frac{1}{2} \text{Re}(\vec{E} \times \vec{H}^*) = \frac{|E_0|^2}{2\eta} \cdot \frac{n}{|n|} \hat{k} \\ \bar{\omega} &= \frac{1}{4} \left\{ \frac{d(\varepsilon\omega)}{d\omega} |E_0|^2 + \frac{d(\mu\omega)}{d\omega} |H_0|^2 \right\} = \frac{1}{4} |E_0|^2 \left\{ \frac{d(\varepsilon\omega)}{d\omega} + \frac{1}{\eta^2} \cdot \frac{d(\mu\omega)}{d\omega} \right\} \end{aligned}$$

Therefore,

$$\begin{aligned}
\vec{v}_e &= \frac{\vec{S}}{\omega} = \left( \frac{|E_0|^2}{2\eta} \cdot \frac{n}{|n|} \hat{k} \right) / \frac{1}{4} |E_0|^2 \left\{ \frac{d(\epsilon\omega)}{d\omega} + \frac{1}{\eta^2} \cdot \frac{d(\mu\omega)}{d\omega} \right\} \\
&= \frac{2n}{\eta|n|} \hat{k} \left[ \frac{d(\epsilon\omega)}{d\omega} + \frac{1}{\eta^2} \cdot \frac{d(\mu\omega)}{d\omega} \right]^{-1} = \frac{2n}{\eta|n|} \hat{k} \left[ \left( \epsilon + \omega \frac{d\epsilon}{d\omega} \right) + \frac{1}{\eta^2} \cdot \left( \mu + \omega \frac{d\mu}{d\omega} \right) \right]^{-1} \\
&= \frac{2n\hat{k}}{\eta|n|\epsilon} \left[ \left( 1 + \frac{\omega}{\epsilon} \frac{d\epsilon}{d\omega} \right) + \left( \frac{\omega}{\mu} + \omega \frac{d\mu}{d\omega} \right) \right]^{-1} \\
&= \frac{2n\hat{k}}{|n|\sqrt{\epsilon\mu}} \left[ \left( 1 + \frac{\omega}{\epsilon} \frac{d\epsilon}{d\omega} \right) + \left( \frac{\omega}{\mu} + \omega \frac{d\mu}{d\omega} \right) \right]^{-1} \\
&= \frac{2n\hat{k}}{|n|\frac{n}{c_0}} \cdot \frac{1}{\left( 1 + \frac{\omega}{\epsilon} \frac{d\epsilon}{d\omega} \right) + \left( \frac{\omega}{\mu} + \omega \frac{d\mu}{d\omega} \right)} = \frac{c_0\hat{k}}{|n|\left( 1 + \frac{\omega}{|n|} \frac{d|n|}{d\omega} \right)} \\
&= \frac{\vec{v}_p}{\left( 1 + \frac{\omega}{|n|} \frac{d|n|}{d\omega} \right)} = \frac{\vec{v}_p}{\alpha} \tag{1.20}
\end{aligned}$$

Comparing Eq. (1.14) to (1.20), one immediately sees that the energy velocity is the same as the group velocity. In a right-handed medium, where  $\alpha > 0$ ,  $\vec{v}_g$  and  $\vec{v}_e$  are in the same direction as  $\vec{v}_p$  while in a left-handed medium, where  $\alpha < 0$ ,  $\vec{v}_g$  and  $\vec{v}_e$  are in the opposite direction of  $\vec{v}_p$ .

## 1.2 Realization of NIMs

Although more than three decades ago, Veselago predicted many unusual properties of a hypothetical isotropic medium with simultaneously negative electrical permittivity ( $\epsilon$ ) and magnetic permeability ( $\mu$ ), they remained completely hypothetical until the experiment of D. R. Smith and co-workers [8,9] was realized with a combination of the pioneering works of J.

B. Pendry, who designed the split ring resonators (SRRs) for negative permeability [15] and an infinite metal wires array for negative permittivity [16], leading to a negative refractive index.

## 1.2.1 SRRs and Thin Metal wires

### 1.2.1.1 Thin Metal wires for Effective Negative Permittivity

Materials with negative permittivity are found routinely in nature. All naturally occurring metals have negative permittivity up to the plasma frequency ( $\omega_p$ ). The plasma frequencies are in the ultraviolet or visible range, and are many orders of magnitude higher than microwave frequencies. For the purpose of constructing metamaterials with metallic structures, it is desirable to scale the value of  $\varepsilon$  (that is, plasma frequency) to reasonable value (on the order of -1) to improve the impedance matching and transmission. In Ref [16], the authors theoretically demonstrated very low plasma frequency resulting from an array of thin metal wires. The configuration of an array of thin metal wires is illustrated in Fig. 1.4. The plasma frequency ( $\omega_p$ )

in the Drude model for dielectric function of a metal given by  $\varepsilon(\omega) = 1 - \frac{\omega_p^2}{\omega(\omega + i\omega_c)}$ , where  $\omega_c$

is the scattering frequency of bulk metal [17-19], can be written as

$$\omega_p = \sqrt{\frac{ne^2}{\varepsilon_0 m_{eff}}} \quad (1.21)$$

where  $n$  is the electron density and  $m_{eff}$  is the effective mass of electrons.



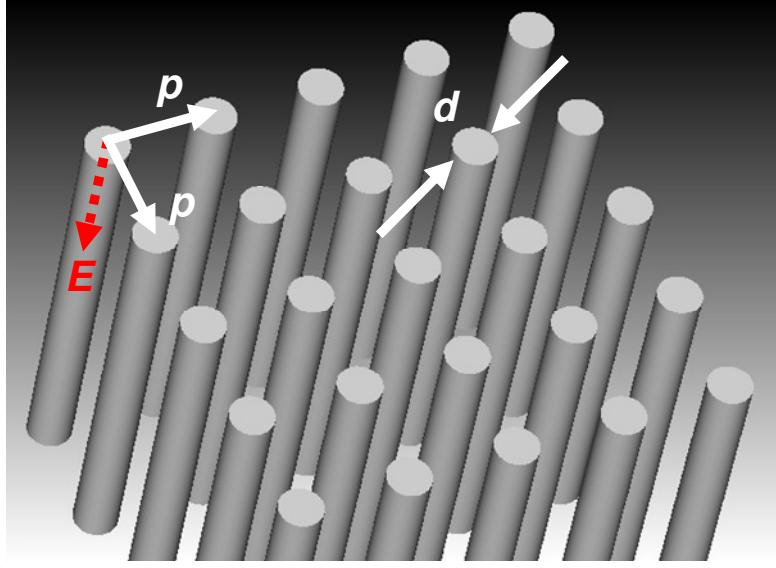


Fig. 1.4 Schematic view of an array of thin metal wires with geometrical parameters ( $p$ : pitch,  $d$ : diameter) and the direction of electric field ( $\vec{E}$ ) along with thin metal wires.

The reasons that an array of thin metal wires lowers the plasma frequency are due to the diluted effective electron density and effective mass. The effective electron density is obtained by the ratio of volume occupied by the metallic thin wire to the vacuum space and expressed as

$$n_{eff} = n \frac{\pi \left(\frac{d}{2}\right)^2}{p^2} \quad (1.22)$$

Furthermore, the effect of the self-inductance of the structure can be considered as a contribution to the effective mass of the electrons [16], which is given as

$$m_{eff} = \frac{\mu_0 (d/2)^2 e^2 n}{2} \cdot \ln\left(\frac{2p}{d}\right) \quad (1.23)$$

Therefore, if the effective electron density ( $n_{\text{eff}}$ ) decreases and the effective mass ( $m_{\text{eff}}$ ) increases, then the plasma frequency ( $\omega_p$ ) decreases. In other words, the plasma frequency ( $\omega_p$ ) of 2D array of metal thin wires can be written as

$$\omega_p = \sqrt{\frac{ne^2}{\epsilon_0 m_{\text{eff}}}} = \sqrt{\frac{e^2}{\epsilon_0} \left( \frac{n\pi \left(\frac{d}{2}\right)^2 / p^2}{\frac{\mu_0 (d/2)^2 e^2 n}{2} \cdot \ln\left(\frac{2p}{d}\right)} \right)} = \sqrt{\frac{2c_0^2 \pi}{p^2 \ln\left(\frac{2p}{d}\right)}} \quad (1.24)$$

It can be seen that the plasma frequency only depends on the geometrical parameters, pitch ( $p$ ) and the diameter of metal wire ( $d$ ).

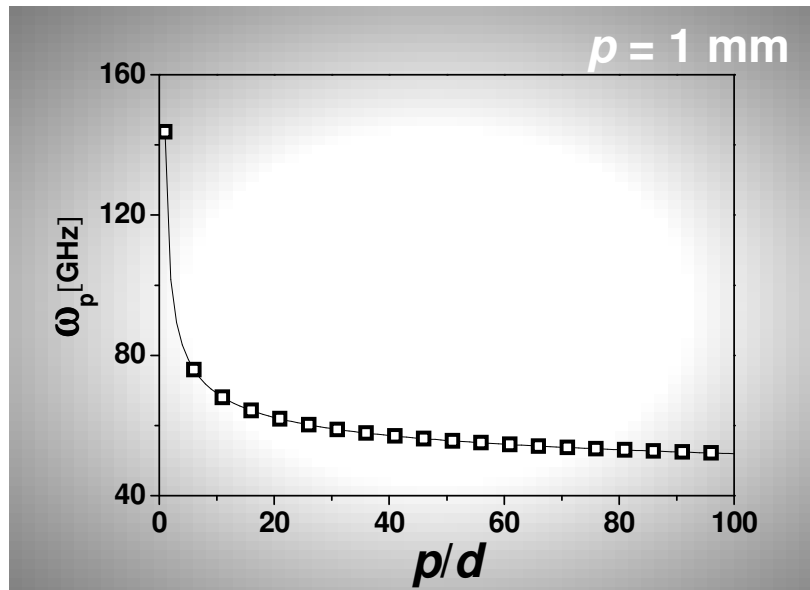


Fig. 1.5 The plasma frequency ( $\omega_p$ ) is the function of structural geometry,  $p/d$ , where  $p$  is the pitch (1 mm) and  $d$  is the diameter of metal wire.

### 1.2.1.2 SRRs for Effective Negative Permeability

As shown in Fig. 1.6, SRRs consist of two concentric metallic rings, each with a gap facing towards opposite directions, providing a narrow frequency band with negative permeability under certain polarizations of the incident electromagnetic wave [15]. This structure is equivalent to a *RLC* circuit. The inductance ( $L$ ) is due to the two loops, and the capacitance ( $C$ ) is generated between inner and outer metallic rings and the gap in between, and the resistance ( $R$ ) is a result of the Ohmic loss of the metal.

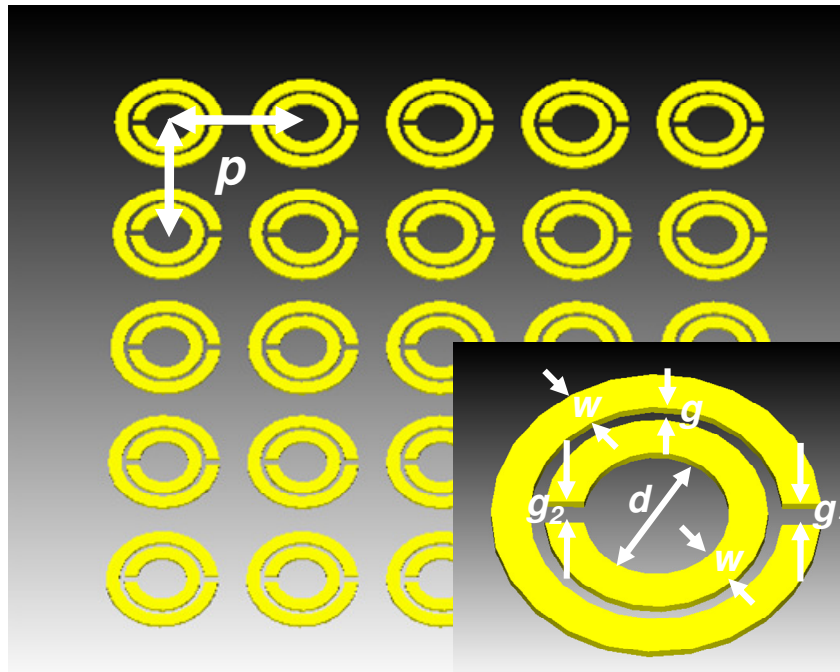


Fig. 1.6 Schematic view of an array of SRRs with pitch ( $p$ ). Inset shows the unit cell of the SRRs with geometric parameters: diameter ( $d$ ), gap between inner and outer rings ( $g$ ), ring width ( $w$ ) and the gaps in the inner and outer rings ( $g_1, g_2$ ).

Incident light is applied with magnetic field ( $\vec{H}$ ) perpendicular to the structure, the induced current is generated in the inner and outer metallic rings. In the vicinity of the resonant frequency ( $\omega_0$ ) given as  $\sim \sqrt{LC}$ , the magnetic response would be the strongest.

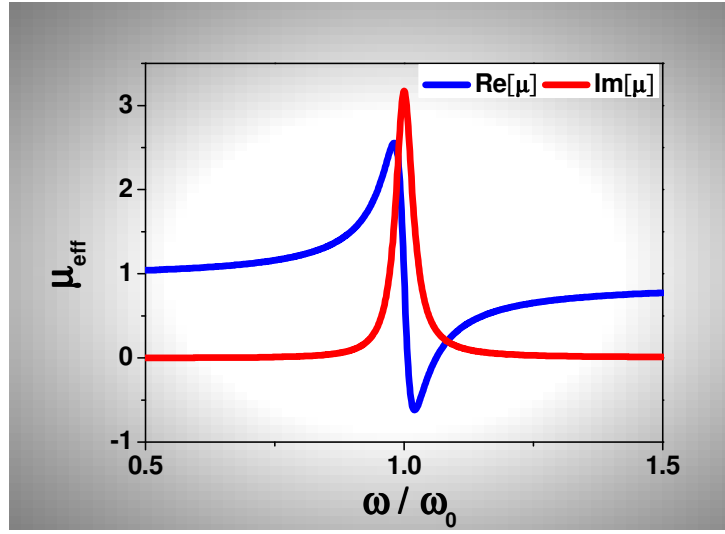


Fig. 1.7 Real (blue line) and imaginary (red line) parts of the effective permeability ( $\mu_{\text{eff}}$ ) are the function of the frequency ( $\omega/\omega_0$ ), where  $\omega_0$  is the resonant frequency.

The effective permeability ( $\mu_{\text{eff}}$ ) can be written as

$$\mu_{\text{eff}} = 1 - \frac{\pi \frac{(d/2)^2}{p^2}}{1 - \frac{3pc_0^2}{\pi\omega^2 \left(\frac{d}{2}\right)^2 \ln\left(\frac{2w}{g}\right)} + i \frac{2p\sigma}{\omega\mu_0 \left(\frac{d}{2}\right)}} = 1 - \frac{\pi \frac{d^2}{4p^2}}{1 - \frac{12pc_0^2}{\pi\omega^2 d^2 \ln\left(\frac{2w}{g}\right)} + i \frac{4p\sigma}{\omega\mu_0 d}} \quad (1.25)$$

$$\omega_0 = \frac{12pc_0^2}{\pi\omega^2 d^2 \ln\left(\frac{2w}{g}\right)}$$

where  $\omega_0$  is the resonant frequency and  $\mu_0$  is the permeability of free space [15]. The real part of effective permeability due to SRRs has negative value within a narrow frequency band above the resonant frequency ( $\omega_0$ ).

### 1.2.2 Single SRR (U-shaped SRR)

Figure 1.8 shows the analogy of a conventional  $LC$  circuit and a metallic single SRR (U-shaped SRR) on a dielectric surface [20].

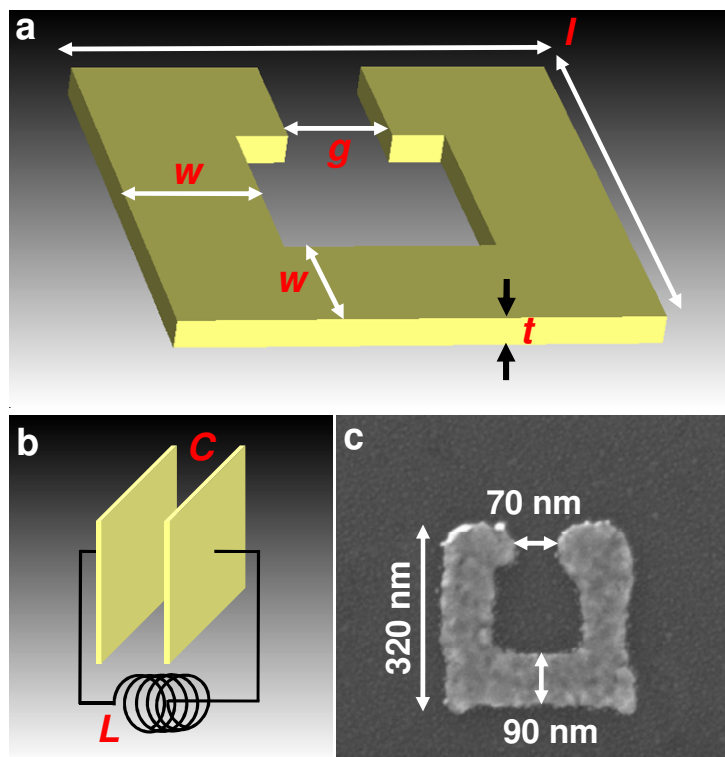


Fig. 1.8 (a) Schematic view of single SRR with geometrical parameters: gap ( $g$ ), length ( $l$ ), width ( $w$ ) and thickness ( $t$ ). (b) Illustration of the equivalent circuit consisting of an inductance ( $L$ ) and a capacitance ( $C$ ). (c) SEM image of fabricated single SRR [20].

The anticipated  $LC$  resonant frequency can be estimated by the following approach: the capacitance ( $C$ ) for a large capacitor with nearby plates can be described as  $C \propto$  plate area/distance and the inductance ( $L$ ) for a long coil with  $N$  windings for  $N = 1$  ( $L \propto$  coil area/length). Using the geometrical parameters as shown in Fig. 1.8 (b), width of metal ( $w$ ), gap of the capacitor ( $g$ ), thickness of metal ( $t$ ) and length of the coil ( $l$ ), the capacitance and the inductance can be found as

$$C = \epsilon_0 \epsilon_c \frac{wt}{g}, \quad L = \mu_0 \frac{l^2}{t} \quad (1.26)$$

where the effective permittivity ( $\epsilon_c$ ) of the material in between the plates [20-24]. This leads to the eigenfrequency ( $\omega_{LC}$ ) and to the  $LC$  resonant wavelength ( $\lambda_{LC}$ )

$$\begin{aligned} \omega_{LC} &= \frac{1}{\sqrt{LC}} = \frac{1}{\sqrt{\mu_0 \frac{l^2}{t} \epsilon_0 \epsilon_c \frac{wt}{g}}} = \frac{1}{\sqrt{\mu_0 \frac{l^2}{1} \epsilon_0 \epsilon_c \frac{w}{g}}} = \frac{c_0}{l \sqrt{\frac{w}{g} \epsilon_c}} \\ \lambda_{LC} &= \frac{2\pi c_0}{\omega_{LC}} = 2\pi l \sqrt{\frac{w}{g} \epsilon_c} \end{aligned} \quad (1.27)$$

From Eq. (1.27), the resonant wavelength ( $\lambda_{LC}$ ) is approximately  $10 \times l$  ( $\lambda_{LC} \approx 10 \times l$ ), using relevant parameters,  $\epsilon_c \geq 1$  and  $w \approx g$ . Figure 1.9 shows

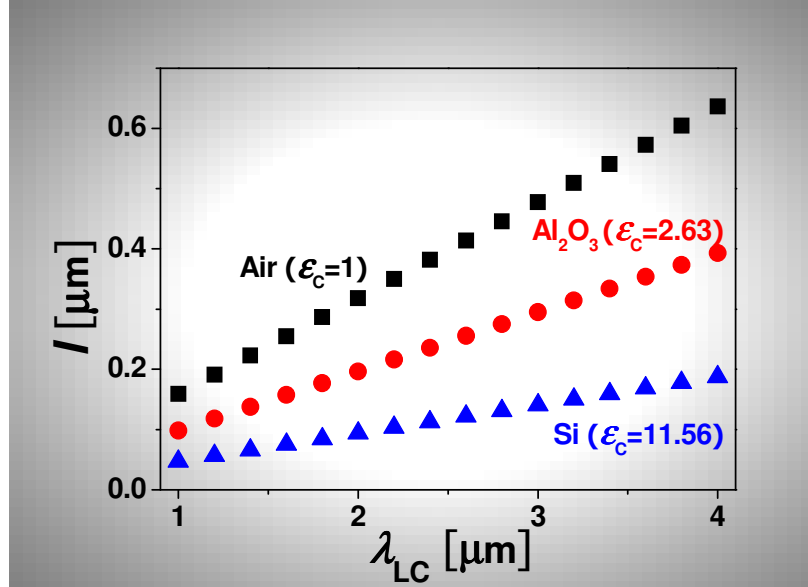


Fig. 1.9 The length of single SRR ( $l$ ) as shown in Fig. 1.8 is the function of the resonant wavelength ( $\lambda_{LC}$ ) with effective permittivity ( $\epsilon_c$ ) of three different materials (air, sapphire and silicon) in between the plates, and  $w \approx g$ .

### 1.2.3 Cut-wire pairs

The connection between single SRR (called U-shaped SRR) as shown in Fig. 1.8 and cut-wire pairs is illustrated in Fig. 1.10 (a)-(d) [25-29]. In the transition from Fig. 1.10 (a) to (b), the  $LC$  resonant frequency increases because it is proportional to the square root of distance ( $g$ ) between plates, resulting from Eq. (1.27). In next transition from Fig. 1.10 (b) to (c), the additional opening the bottom arm of the U-shaped SRR results in the increase of  $LC$  resonant frequency due to a second serial capacitance, further reducing the net capacitance in the  $LC$  circuit. A pair of cut wires is generated by further opening of the lower slit as shown in the transition from Fig. 1.10 (c) to (d). The Ohmic currents in the horizontal arms in single SRR

structure as shown in Fig. 1.8 and Fig. 1.10 (a) have been replaced by displacement currents in cut-wire pairs as shown in Fig. 1.10 (d), in addition that the resonant frequency is increased.

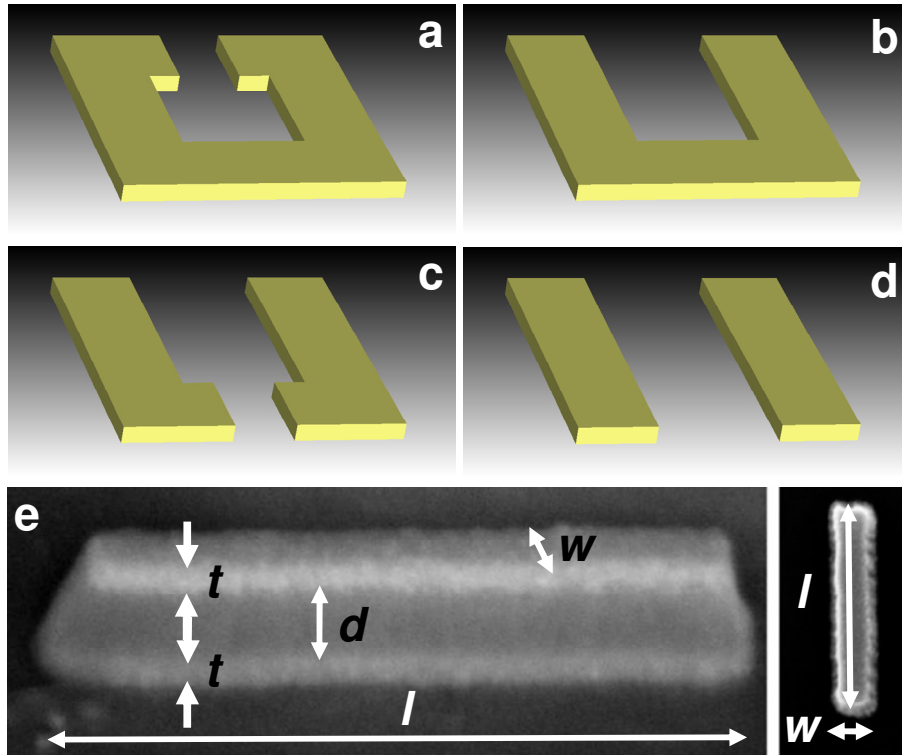


Fig. 1.10 Schematic view of transition from (a) single SRR (U-shaped SRR) to (d) cut-wire pairs. (e) Side/top view SEM image of cut-wire pairs [27].

### 1.2.4 Fishnet structure

Zhang *et al.* proposed [30] and experimentally demonstrated [31] a NIM structure composed of two parts at near infrared regime: an array of thin metal wires parallel to the direction of electric field as shown in Fig. 1.11 (a) leads to the negative electric permittivity ( $\epsilon$ ) below the effective plasma frequency of this diluted metal and the negative magnetic



permeability ( $\mu$ ) from a pair of finite-width metal stripes separated by a dielectric layer along the direction of the incident magnetic field as shown in Fig. 1.11 (b). The resulting structure is a 2-dimensional array of holes penetrating completely through a metal-dielectric-metal film stack as shown in Fig. 1.11 (c), (d) [32]. The fishnet structure as shown in Fig. 1.11 (c), (d) has been brought towards the visible regime [33].

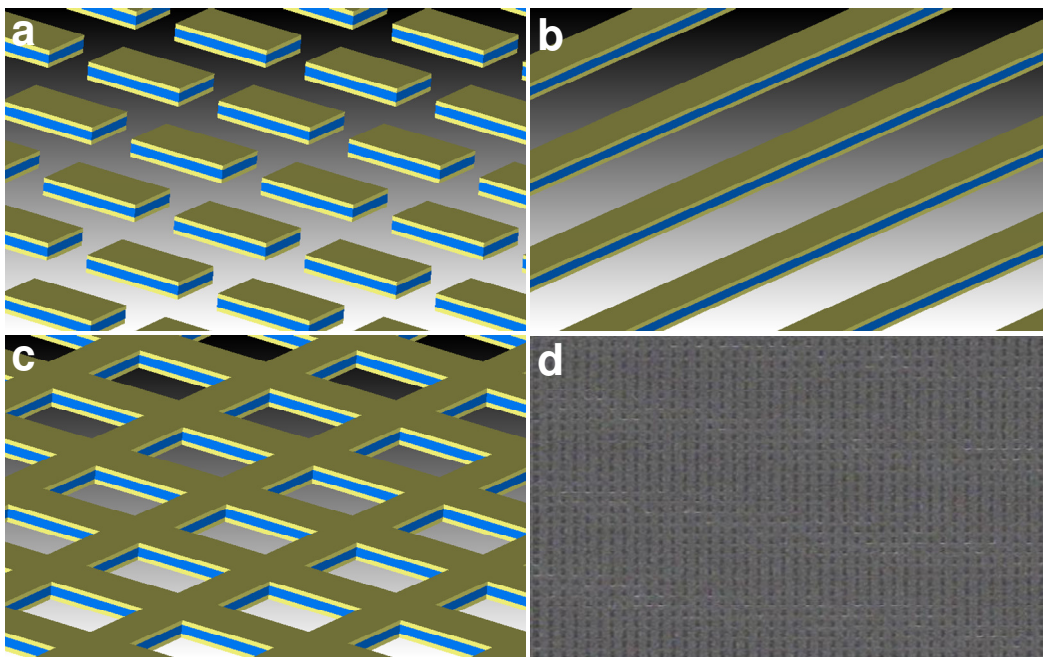


Fig. 1.11 Schematic view of (a) magnetic atoms with a negative permeability and (b) electric atoms with a negative permittivity. The combination of (a) and (b) leads to a negative refractive index ( $n' < 0$ ), which is called (c) a fishnet NIM. (d) Top view of SEM image of a fabricated fishnet NIM [32].

### **1.3 Outline of the Dissertation**

The object of this work is to explore the physical origin and applicability of the metamaterials or NIMs. The outline of this dissertation is as follows.

Chapter 1 is the introduction and outline.

Chapter 2 describes the detailed processing flows, for samples made on glass substrate with a single-step interferometric lithography patterning technique and self-aligned processing. With small modifications as noted, the processing can be used for making samples discussed for future work in Chapter 6.

Chapter 3 discusses the structural impact on the NIMs. NIMs at near infrared wavelengths are fabricated with circular, elliptical and rectangular holes penetrating through metal/dielectric/metal films. All three NIM structures exhibit similar figure of merit; however, the transmission is higher for the NIM with rectangular holes as a result of an improved impedance match with the substrate-superstrate (air-glass) combination.

Chapter 4 reports the bi-anisotropic effects due to sidewall-angle in NIMs. In general, the processing procedure to fabricate the fishnet structured NIMs is to define the hole-size using a polymeric material, usually by lithographically defining polymer posts, followed by deposition of the constitutive materials and dissolution of the polymer (liftoff processing). This processing (fabrication of posts: multi-layer deposition: liftoff) often gives rise to significant sidewall-angle

because materials accumulate on the tops of the posts that define the structure, each successive film deposition has a somewhat larger aperture on the bottom metamaterial film, giving rise to a nonzero sidewall-angle and to optical bianisotropy.

Chapter 5 demonstrates a nanometer-scale, sub-picosecond metamaterial device capable of over terabit/second all-optical communication in the near infrared spectrum. We achieve a 600 fs device response by utilizing a regime of sub-picosecond carrier dynamics in amorphous silicon and  $\sim 70\%$  modulation in a path length of only 124 nm by exploiting the strong nonlinearities in metamaterials. We identify a characteristic signature associated with the negative index resonance in the pump-probe signal of a fishnet structure. We achieve much higher switching ratios at the fundamental resonance ( $\sim 70\%$ ) relative to the secondary resonance ( $\sim 20\%$ ) corresponding to the stronger negative index at the fundamental resonance. This device opens the door to other compact, tunable, ultrafast photonic devices and applications.

Chapter 6 provides suggestions for future research topics extending this work.

## 1.4 References

1. V. M. Shalaev, "Optical negative-index metamaterials," *Nat. Photonics* **1**, 41–48 (2007).
2. C. M. Soukoulis, S. Linden, and M. Wegener, "Negative Refractive Index at Optical Wavelengths," *Science* **315**, 47-49 (2007).
3. V. G. Veselago, "The electrodynamics of substances with simultaneously negative values of  $\epsilon$  and  $\mu$ ," *Sov. Phys. USP.* **10**, 509 (1968).
4. D. R. Smith, J. B. Pendry, and M. C. K. Wiltshire, "Metamaterials and Negative Refractive Index," *Science* **305**, 788 (2004).
5. J. B. Pendry and D. R. Smith, "Reversing Light with Negative Refraction," *Phys. Today* **57**, 37-43 (2004).
6. C. M. Soukoulis, "Bending Back Light: The Science of Negative Index Materials," *Optics and Photonic News* June, 16-21 (2006).
7. C. M. Soukoulis, M. Kafesaki, and E. N. Economou, "Negative-Index Materials: New Frontiers in Optics," *Adv. Mater.* **18**, 1941 (2006).
8. D. R. Smith, W. J. Padilla, D. C. Vier, S. C. Nemat-Nasser, and S. Schultz, "Composite medium with simultaneously negative permeability and permittivity," *Phys. Rev. Lett.* **84**, 4184-4187 (2000).
9. R. A. Shelby, D. R. Smith, and S. Schultz, "Experimental verification of a negative index of refraction," *Science* **292**, 77-79 (2002).
10. K. Busch, G. von Freymann, S. Linden, S. F. Mingaleev, L. Theselashvili, and M. Wegener, "Periodic nanostructures for photonics," *Phys. Rep.* **444**, 101–202 (2007).
11. J. D. Jackson, *Classical Electrodynamics*. John Wiley, third ed., 1998.
12. L. D. Landau, E. M. Lifshitz, and L. P. Pitaevskii, *Electrodynamics of Continuous Media*. Linacre House, Jordan Hill, Oxford, UK: Butterworth Heinemann, 1984.
13. Lecture Notes from *Martin Wegener and Vladimir Shalaev*.
14. Dissertation of *Shuang Zhang and Jiangfeng Zhou*.
15. J. B. Pendry, A. Holden, D. Robbins, and W. Stewart, "Magnetism from conductors and enhanced nonlinear phenomena," *IEEE Trans. Microwave Theory Tech.* **47**, 2075 (1999).

16. J. B. Pendry, A. Holden, W. Stewart, and I. Youngs, "Extremely low frequency plasmons in metallic mesostructures," *Phy. Rev. Lett.* **76**, 4773 (1996).
17. M. A. Ordal, L. L. Long, R. J. Bell, S. E. Bell, R. R. Bell, R. W. Alexander, and C. A. Ward, "Optical properties of the metals Al, Co, Cu, Au, Fe, Pb, Ni, Pd, Pt, Ag, Ti and W in the infrared and far infrared," *Appl. Opt.* **22**, 1099 (1983).
18. P. B. Johnson and R. W. Christy, "Optical constants of the noble metals," *Phys. Rev. B* **6**, 4370–4379 (1972).
19. E. D. Palik, "Handbook of Optical Constants of Solids" (Academic Press, San Diego, 1998).
20. S. Linden, C. Enkrich, M. Wegener, J. Zhou, T. Koschny, and C. M. Soukoulis, "Magnetic Response of Metamaterials at 100 Terahertz," *Science* **306**, 1351 (2004).
21. M. Shamonin, E. Shamonina, V. Kalinin, and L. Solymar, "Properties of a metamaterial element: Analytical solutions and numerical simulations for a singly split double ring," *J. Appl. Phys.* **95**, 3778 (2004).
22. C. Enkrich, F. Pérez-Willard, D. Gerthsen, J. Zhou, C. M. Soukoulis, M. Wegener, and S. Linden, "Focused-Ion-Beam Nanofabrication of Near-Infrared Magnetic metamaterials," *Adv. Mater.* **17**, 2547 (2005).
23. C. Enkrich, M. Wegener, S. Linden, S. Burger, L. Zschiedrich, F. Schmidt, J. Zhou, T. Koschny, and C. M. Soukoulis, "Magnetic Metamaterials at Telecommunication and Visible Frequencies," *Phys. Rev. Lett.* **95**, 203901(2005).
24. M. W. Klein, C. Enkrich, M. Wegener, C. M. Soukoulis, and S. Linden, "Single-slit split-ring resonators at optical frequencies: limits of size scaling," *Opt. Lett.* **31**, 1259 (2006).
25. L. V. Panina, A. N. Grigorenko, and D. P. Makhnovskiy, "Optomagnetic composite medium with conducting nanoelements," *Phys. Rev. B* **66**, 155411 (2002).
26. V. A. Podolskiy, A. K. Sarychev, E. E. Narimanov, and V. M. Shalaev, "Resonant light interaction with plasmonic nanowire systems," *J. Opt. A: Pure Appl. Opt.* **7**, 32 (2005).
27. G. Dolling, C. Enkrich, M. Wegener, J. Zhou, C. M. Soukoulis, and S. Linden, "Cut-wire pairs and plate pairs as magnetic atoms for optical metamaterials," *Opt. Lett.* **30**, 3198 (2005).
28. A. N. Lagarkov and A. K. Sarychev, "Electromagnetic properties of composites containing elongated conducting inclusions," *Phys. Rev. B* **53**, 6318 (1996).
29. V. M. Shalaev, W. Cai, U. K. Chettiar, H. Yuan, A. K. Sarychev, V. P. Drachev, and A. V. Kildishev, "Negative index of refraction in optical metamaterials," *Opt. Lett.* **30**, 3356 (2005).

30. S. Zhang, W. Fan, K. J. Malloy, S. R. J. Brueck, N.-C. Panoiu, and R. M. Osgood, "Near-infrared double negative metamaterials," *Opt. Express* **13**, 4922-4930 (2005).
31. S. Zhang, W. Fan, N. C. Panoiu, K. J. Malloy, R. M. Osgood, and S. R. J. Brueck, "Experimental demonstration of near-infrared negative-index metamaterials," *Phys. Rev. Lett.* **95**, 137404 (2005).
32. Z. Ku and S. R. J. Brueck, "Comparison of negative refractive index materials with circular, elliptical and rectangular holes," *Opt. Express* **15**, 4515-4522 (2007).
33. G. Dolling, M. Wegener, C. M. Soukoulis, and S. Linden, "Negative-index metamaterial at 780 nm wavelength," *Opt. Lett.* **32**, 53 (2007).

## **Chapter 2 Fabrication**

### **2.1 Nanofabrication**

Nanophotonics including the negative-index metamaterials [1-6], metamaterials [7-9], surface plasmonic structures [10-15], two- and three-dimensional photonic crystals [16-20] and distributed feedback/distributed Bragg reflectors [21] is often required to be for large areas of periodic or quasi-periodic structures. Present nanofabrication of the periodic structures widely employs standard semiconductor techniques: conventional lithography (interferometric [22-25], electron-beam [26,27], focused-ion-beam [28,29], or nano-imprint [30,31]), electron-beam evaporation, etching, and liftoff processing.

#### **2.1.1 Interferometric Lithography**

Interferometric lithography (IL), a parallel process which can obtain uniform patterns over a large area, utilizes a small number (most often two) coherent laser beams incident from different directions on a photoresist (PR) film to produce an interference pattern whose intensity distribution is recorded in the photosensitive layer and is later transferred (developed) by thermal (e.g. a post-exposure bake) and chemical (e.g. developer solution) processes.

#### **2.1.2 IL Setup**

The basic setup of IL is as shown in Fig. 2.1. The coherent laser source is split into two parts. One is going to the sample directly and the other is reflected by the mirror to the sample.

The angle  $\theta$  is formed between the beam and surface normal to the sample. The resulting interference pattern has a period given by the formula,

$$\sin \theta = \frac{\lambda}{2nd} \quad (2.1)$$

where  $d$  is the pitch of grating,  $\lambda$  is the wavelength of the incident beam and  $n$  is the refractive index of the incident medium, usually  $n = n_{air} = 1$ . To produce 2D square array of pattern (posts or holes) in the PR, one IL exposure are carried out, rotating the sample by  $90^\circ$ , and performing a second exposure.

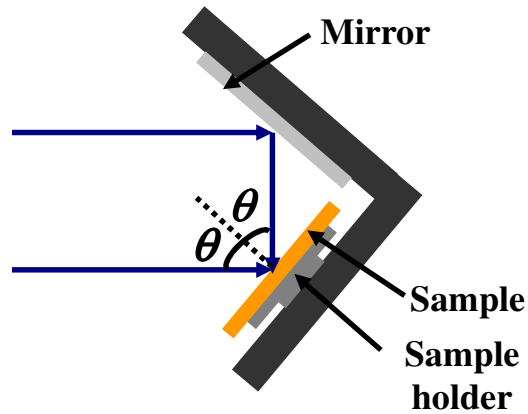


Fig. 2.1 Experimental arrangements of IL.

From Eq. (2.1), taking  $n = 1$  and a laser beam with a wavelength of 355 nm, the limiting period  $d_{min}$  of IL is  $\sim \lambda/2$  ( $\sim 178$  nm). Further reductions in scale are possible with immersion techniques. This allows an improvement in the optical resolution by use of a high-index liquid immersion medium between the exit face of prism and the PR surface. Deionized water with a refractive index of  $\sim 1.44$  is good immersion medium at 193 nm (ArF wavelength) [32-36].



### 2.1.3 PR patterning with IL

Simple two-beam interference produces an array of uniformly spaced parallel lines covering the exposure area, 1D grating. In order to understand the properties of positive/negative-tone PR through 1D grating, on the assumption that above a certain threshold  $D_{th}$  is removed and below  $D_{th}$  is retained on development for positive-tone PR (inverse for negative-tone PR), sinusoidal aerial image is formed in the positive-tone PR layer and square pattern is formed due to high nonlinearity of PR's response as shown in Fig. 2.2.

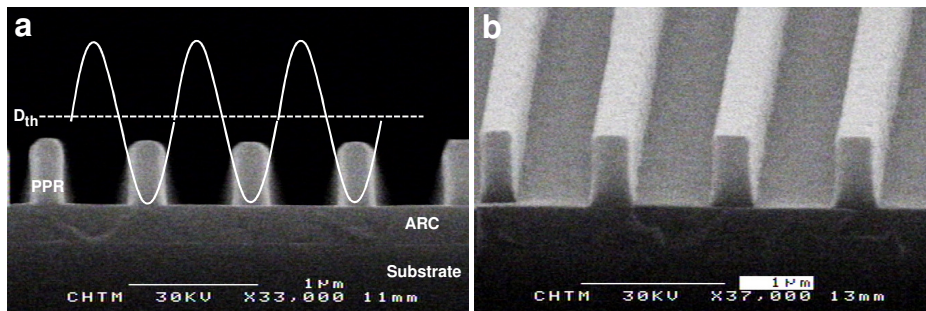


Fig. 2.2 (a) Side view scanning electron microscopy (SEM) image of 1D grating in positive-tone PR with formation of square pattern with sinusoidal aerial pattern. (b) Tilt view SEM image of (a).

For positive-tone PR, high (low) exposure doses results in a 2D array of posts (holes) because exposure changes the chemical structure of the positive-tone PR so that it becomes soluble in the developer solution to clear the exposed resist during developing. Contrary to the

positive-tone PR, exposed area remains in the developer solution for negative-tone PR, resulting in the reverse occurrence of holes and posts as shown in Fig. 2.3.

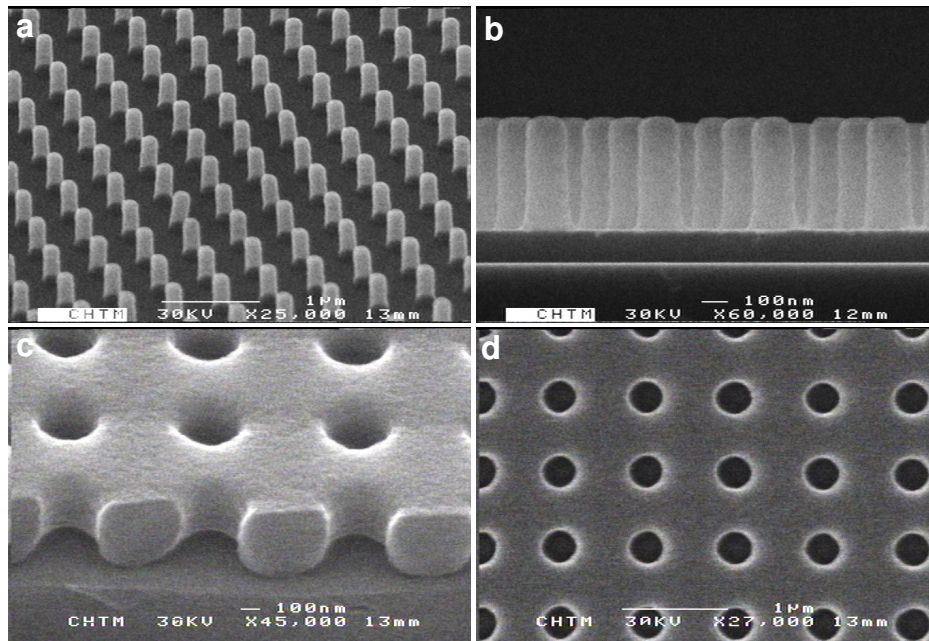


Fig. 2.3 SEM images of (a), (b) a periodic circular posts in positive-tone PR and (c), (d) a periodic circular holes in negative-tone PR.

## 2.2 Fabrication of a Single-functional layered Circular/Elliptical Negative-Index Metamaterial

The structure of a single-functional layered (a functional layer is defined as metal/dielectric/metal) circular/elliptical negative-index metamaterial (NIM) consists of a BK7 glass substrate with three layers, gold (Au); sapphire ( $\text{Al}_2\text{O}_3$ ); and gold (Au) perforated with a two-dimensional square array of circular/elliptical apertures through the entire structure.

Schematic view of processing steps to fabricate one-functional layered circular/elliptical NIM is as shown in Fig. 2.4.

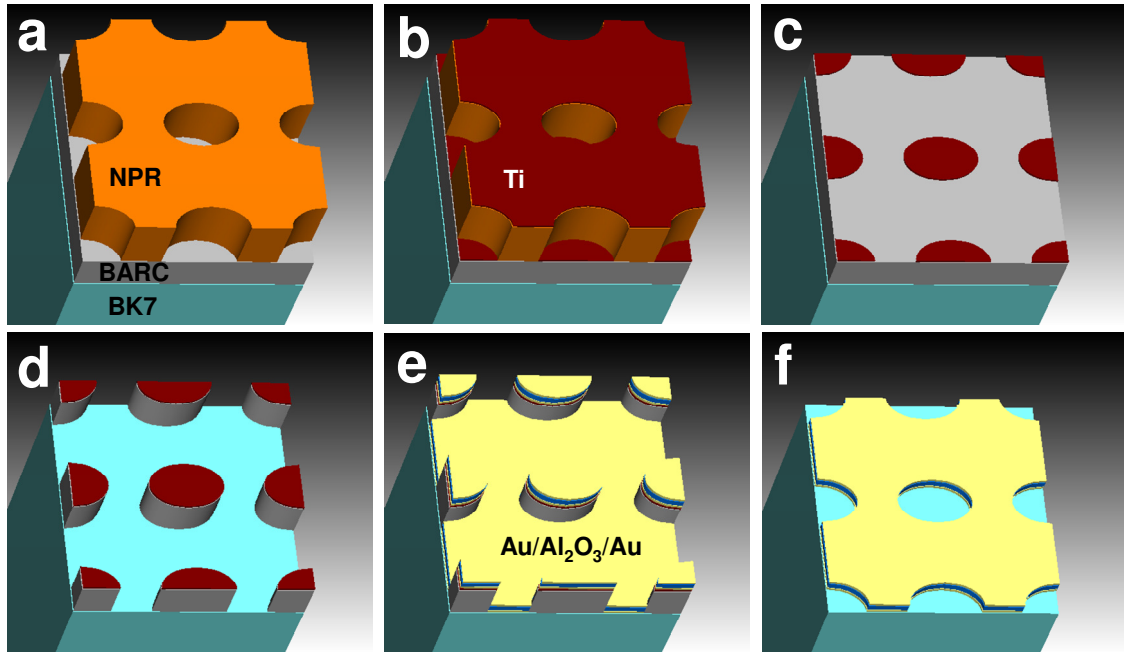


Fig. 2.4 Schematic view of processing flow. (a) Patterning of 2D hole array in PR layer by IL. (b) e-beam evaporation of Titanium (Ti) as the selective etching mask. (c) Liftoff processing. (d) Reactive Ion Etch (RIE) processing into a bottom anti-reflection coating layer (BARC). (e) e-beam evaporation of Au/Al<sub>2</sub>O<sub>3</sub>/Au. (f) Liftoff processing by O<sub>2</sub> plasma ash.

I. Clean substrate: BK7 glass substrate (2.5×2.5 cm<sup>2</sup>) is cleaned with piranha solution with a volume concentration ratio of (H<sub>2</sub>SO<sub>4</sub>:H<sub>2</sub>O<sub>2</sub> = 4:1) to remove any residual organic contamination for 10 min, deionized (DI) water rinse and N<sub>2</sub> blow dry, followed by dehydration on 150°C hotplate for 6 min.

II. Bottom anti-reflection coating (BARC): BARC (Brewer Science: XHRIC-16) for i-line lithography is spun onto the wafer at 4000 rpm for 30 s, the wafer is baked in an oven at 175°C for 3 min; this is repeated twice to make tall posts (thickness is about 320 nm).

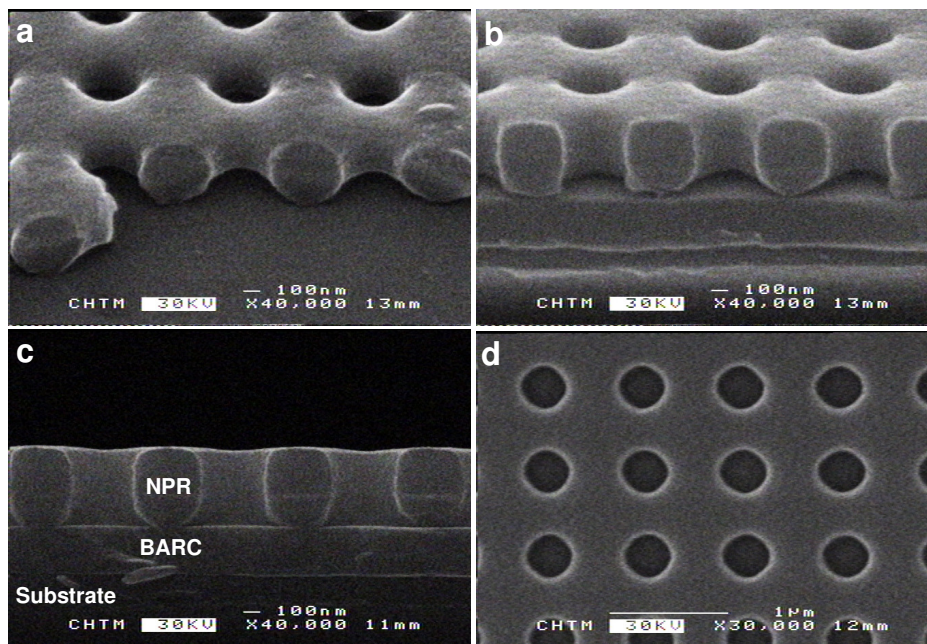


Fig. 2.5 SEM images of samples: (a), (b) Tilt view (c) Side view (d) Top view of a periodic circular hole PR pattern defined by IL.

III. Negative-tone PR (NPR): After the wafer is cooled down, NPR (Futurerex: NR7-500P) for i-line PR is spread on top BARC layers at 4000 rpm for 30 s and oven-baked at 95°C for 3 min (thickness is about 500 nm).

IV. IL: IL is carried out with two coherent beams of UV light (a 355-nm third harmonic YAG:Nd<sup>3+</sup> laser source) forming at an angle of ~12.46° (~823 nm pitch) and produces a periodic

circular/elliptical hole pattern in the NPR layer with two successive orthogonal one-dimensional exposures with power 50 mJ and same/different doses for symmetrical/asymmetrical aperture shape; 2 min post-bake at 110°C is used to drive off volatile compounds from the exposure; after the exposed and post-baked sample is cooled down, it is developed (Shipley, Inc.: MF-702) for 60 s and rinsed with deionized water as shown in Fig. 2.5 and Fig. 2.8 (a), (b).

V. Selective etching mask: After the PR pattern is defined, 25 nm thick Ti is deposited with an e-beam evaporator at a pressure of the order of  $10^{-7}$  Torr during deposition and  $\sim 0.05$  nm/s as a selective etching mask. Sample should be put at the center of the sample holder and the holder should be put in the center spot of the metal evaporator to minimize any shadow effect, which means one sample per run, followed by liftoff processing with acetone to remove the NPR layer. This results in an array of circular/elliptical Ti disks atop the BARC layer as shown in Fig. 2.8 (c), (d).



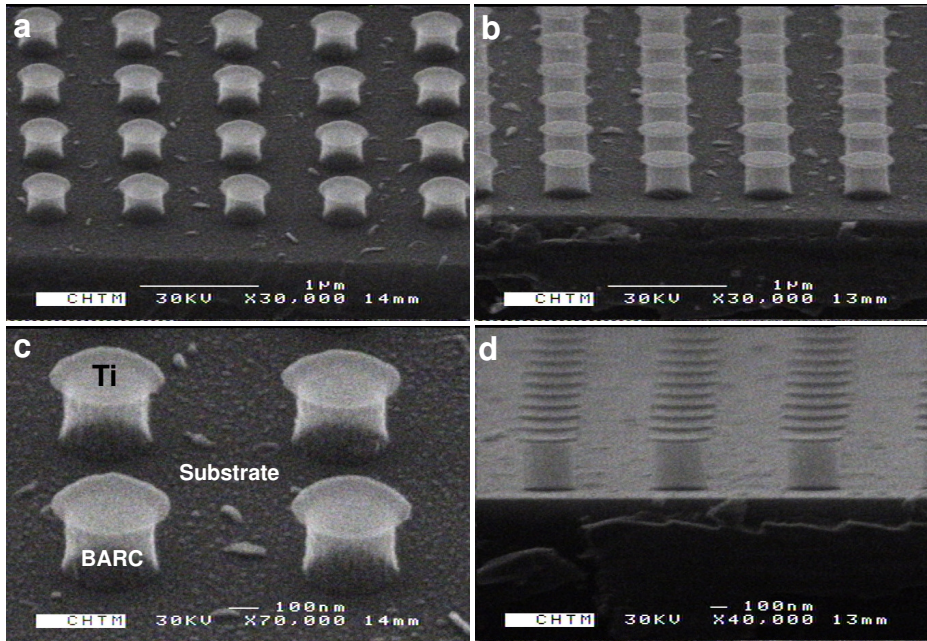


Fig. 2.6 SEM images of BARC posts etched by anisotropic O<sub>2</sub> plasma RIE using Ti as the selective etching mask.

VI. Etch processing: An anisotropic O<sub>2</sub> plasma-reactive ion etch is used to transfer the Ti pattern into the BARC layer with a small isotropic etching component to provide a slight undercut for the final lift-off step as shown in Fig. 2.6 and Fig. 2.9 (a)-(c).

VII. Au/Al<sub>2</sub>O<sub>3</sub>/Au: Au and Al<sub>2</sub>O<sub>3</sub> are deposited alternatively by e-beam evaporation with same condition (pressure, deposition rate and sample-position in e-beam evaporator) as V as shown in Fig. 2.7 (a)-(c).

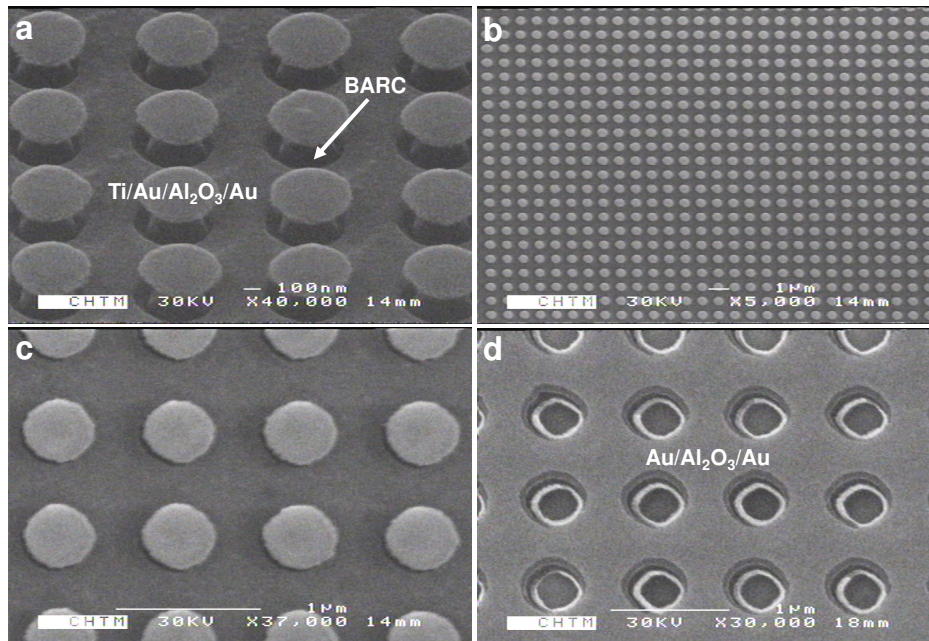


Fig. 2.7 SEM images: (a)-(c) Consecutive Au/Al<sub>2</sub>O<sub>3</sub>/Au deposited samples. (d) Completed Au-Al<sub>2</sub>O<sub>3</sub>-Au samples with circular holes.

VIII. Removal of BARC posts: Finally, a fully isotropic, high pressure O<sub>2</sub> plasma ash is used to remove the BARC posts. This leads to a two-dimensional square array of circular/elliptical holes through the multilayer structure (circular/elliptical NIM) as shown in Fig. 2.7 (d) and Fig. 2.9 (d).

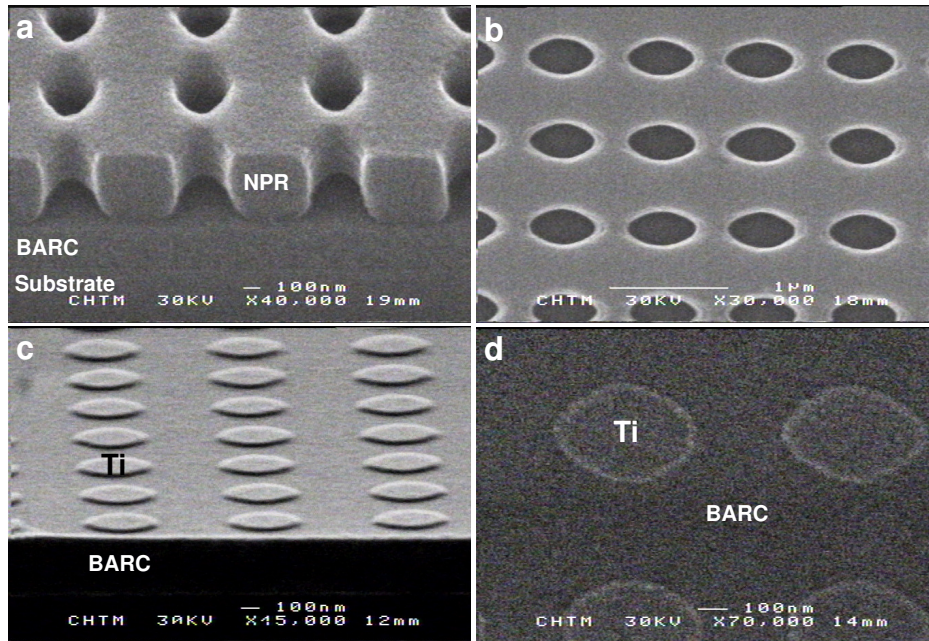


Fig. 2.8 SEM images of samples: (a) Tilt view (b) Top view of a periodic elliptical hole PR pattern defined by IL. (c) Tilt view (d) Top view of an array of circular/elliptical Ti disks atop the BARC layer.



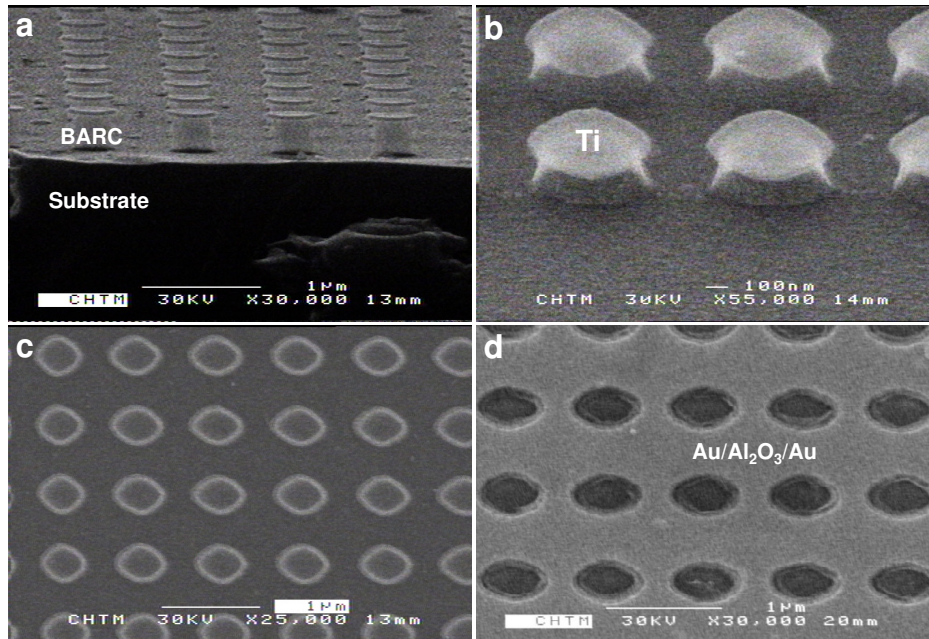


Fig. 2.9 SEM images: (a)-(c) BARC posts etched by anisotropic O<sub>2</sub> plasma RIE using Ti as the selective etching mask. (d) Completed Au-Al<sub>2</sub>O<sub>3</sub>-Au samples with elliptical holes.

### 2.3 Fabrication of a Single-functional layered Fishnet NIM

A single-functional layered rectangular NIMs, which is called fishnet structured NIM, consists of a BK7 glass substrate with Au/Al<sub>2</sub>O<sub>3</sub>/Au layers penetrated with a two-dimensional square array of rectangular apertures through multilayer. Schematic view of brief processing steps to fabricate one-functional layered fishnet structured NIM is as shown in Fig. 2.10. A somewhat different process is used to fabricate the rectangular apertures through the multilayer.

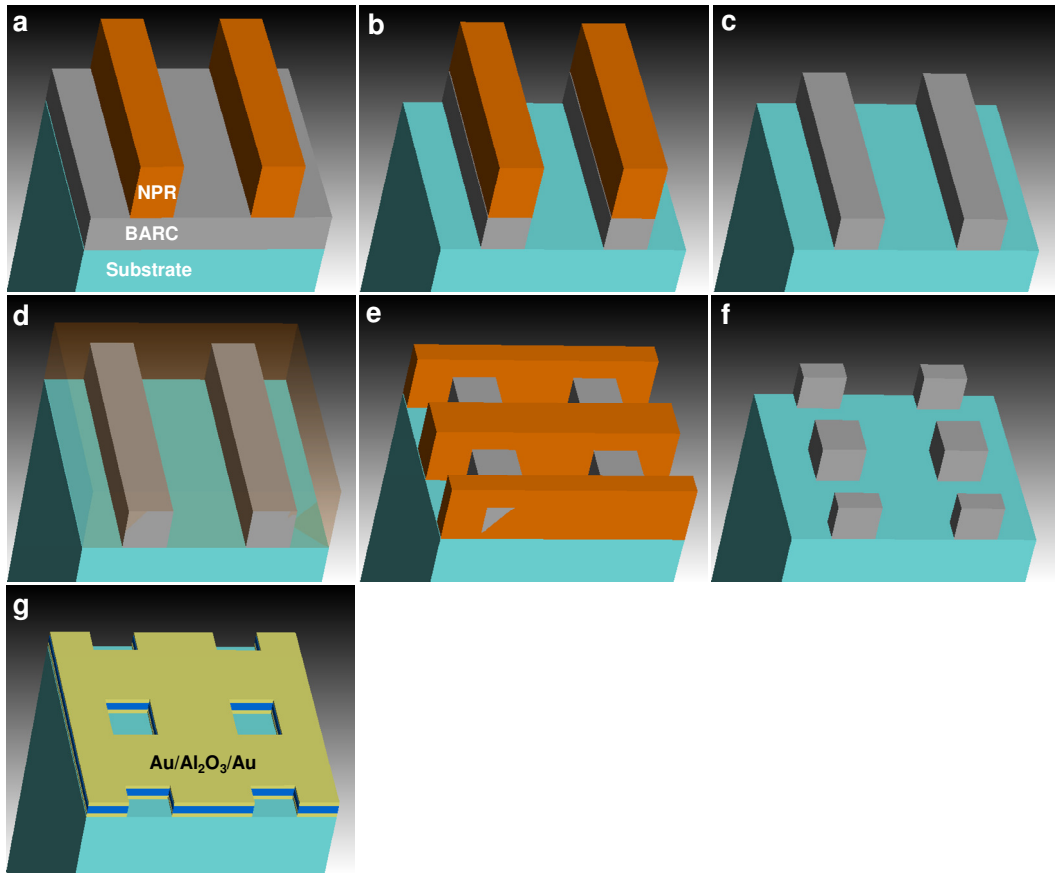


Fig. 2.10 Schematic view of fabrication procedure. (a) 1D Patterning in PR layer by IL. (b) RIE processing into BARC layer. (c) Removal of PR. (d) Recoating the PR. (e) 1D patterning perpendicular to 1D BARC pattern. (f) Removal of PR. (g) e-beam evaporation of Au/Al<sub>2</sub>O<sub>3</sub>/Au and liftoff processing to get rid of BARC rectangular posts.

I. Clean substrate: BK7 glass substrate (2.5×2.5 cm<sup>2</sup>) is cleaned with same recipe as part I in section 2.2 (Fabrication of one-functional layered circular/elliptical NIM).

II. BARC: BARC (XHRIC-16) for i-line lithography is spun onto the wafer with same recipe as part II in section 2.2.

III. NPR: After the wafer is cooled down, NPR (Futurerex: NR7-500P) for i-line PR is spread a top BARC layers at 4000 rpm for 30 s and hotplate-baked at 150°C for 60 s, resulting in vertical NPR sidewall (thickness is about 500 nm).

IV. IL: IL using a 355 nm third harmonic YAG:Nd<sup>3+</sup> laser source produces a single exposure to make 1D pattern in the NPR on BARC with power 50 mJ; 2 m post-bake at 110°C; after the exposed and post-baked sample is cooled down, it is developed (Shipley, Inc.: MF-702) for 13 s due to different baking condition for NPR in part III and rinsed with deionized water as shown in Fig. 2.11 (a).

V. Etch processing: After 1D PR pattern is defined, an anisotropic O<sub>2</sub> plasma-RIE is used to transfer 1D PR pattern into the BARC and 1D PR pattern is used as the selective etching mask, followed by selective removal of the PR layer with acetone, leading to 1D BARC pattern as shown in Fig. 2.11 (c).

VI. Recoat NPR: A second NPR layer is spun onto the 1D BARC pattern with 4000 rpm for 30 s and oven baked at 95°C for 3 min.

VII. IL: IL reproduces a 1D PR pattern at right angles to the original 1D pattern with power 50 mJ; 2 m post-bake at 110°C; after the exposed and post-baked sample is cooled down, it is developed (Shipley, Inc.: MF-702) for 30 s and rinsed with deionized water as shown in Fig. 2.11 (e).

VIII. Etching processing: An anisotropic O<sub>2</sub> plasma-RIE is used to transfer 1D PR pattern into the 1D BARC pattern and 1D PR pattern is used as the selective etching mask, followed by selective removal of the PR layer with acetone, leading to 2D rectangular BARC posts as shown in Fig. 2.11 (f).

IX. Au/Al<sub>2</sub>O<sub>3</sub>/Au: Three layers, Au/Al<sub>2</sub>O<sub>3</sub>/Au, are deposited by e-beam evaporation with same condition as part V in section 2.2.

X. Removal of BARC posts: As the final step of fabricating the fishnet structured NIM, a fully isotropic high pressure O<sub>2</sub> plasma ash is carried out to remove the BARC posts with same recipe as part VIII in section 2.2, leading to the final structure as shown in Fig. 2.11 (e), (f). Figure 2.11 (f) also shows the advantage of large area of patterning using IL techniques [37].

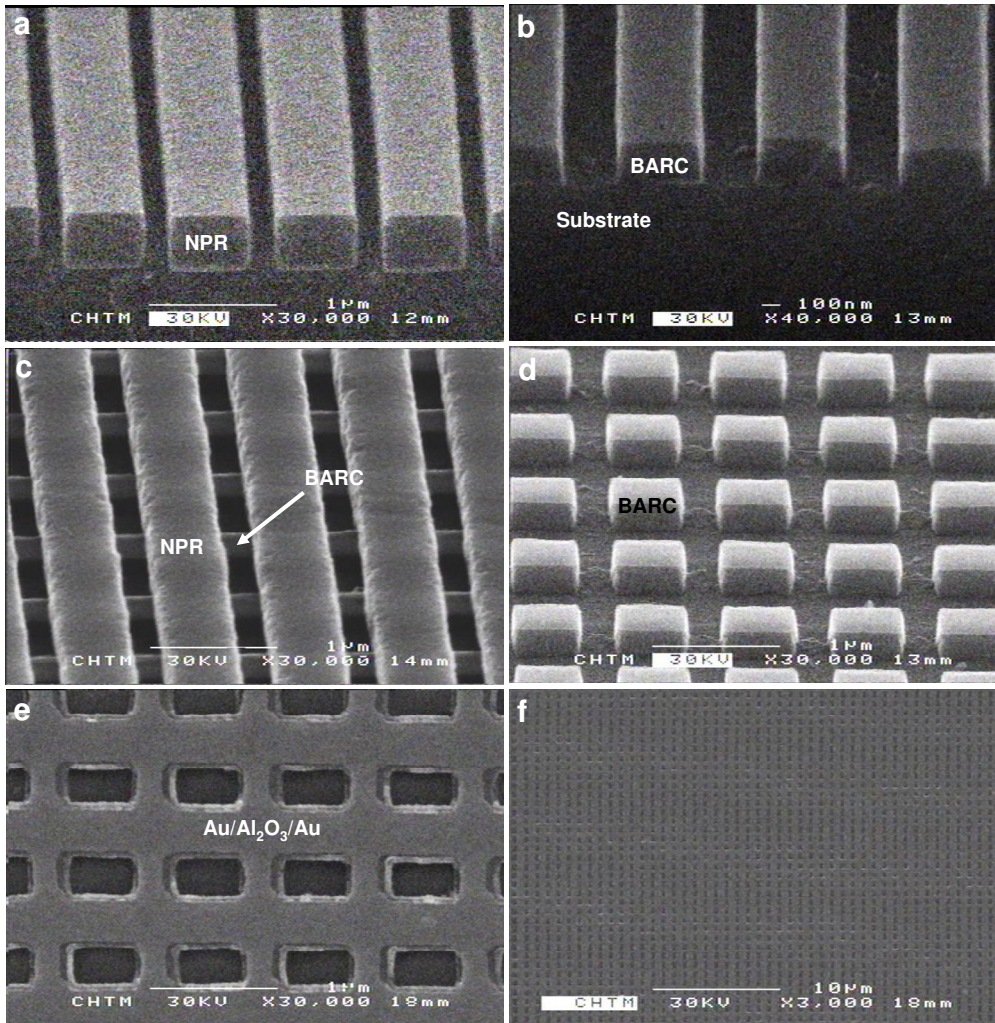


Fig. 2.11 SEM images of fabrication procedure. (a) First 1D PR Pattern on BARC layer by IL. (b) 1D BARC pattern after first anisotropic RIE etch. (c) Second 1D PR pattern perpendicular to (b). (d) Second anisotropic RIE etch, leading to 2D BARC rectangular post pattern. (e), (f) Completely fabricated samples: After e-beam evaporation of Au/Al<sub>2</sub>O<sub>3</sub>/Au, followed by fully isotropic O<sub>2</sub> plasma ash to remove the BARC posts.

## 2.4 Fabrication of Multi-functional layered NIMs

Multifunctional layered elliptical NIMs are composed of a BK7 glass substrate with either one (Au/Al<sub>2</sub>O<sub>3</sub>/Au), two (Au/Al<sub>2</sub>O<sub>3</sub>/Au/Al<sub>2</sub>O<sub>3</sub>/Au), or three (Au/Al<sub>2</sub>O<sub>3</sub>/Au/Al<sub>2</sub>O<sub>3</sub>/Au/Al<sub>2</sub>O<sub>3</sub>/Au) functional layers perforated with a two-dimensional square array of elliptical apertures through the entire structure. In brief, as different processes from section 2.2, thicker BARC layer is used to make tall posts, more anisotropic O<sub>2</sub> plasma RIE used to etch thicker BARC layer and metal/dielectric material deposited alternatively by e-beam evaporation for one to three functional layers.

I. Clean substrate: same recipe as part I in section 2.2.

II. BARC: BARC (XHRIC-16) is spun onto the wafer with similar recipe as part I in section 2.2 except that this is repeated three times with different baking time (2/2/3 min) at 175°C in oven, to make tall posts (thickness is about 480 nm).

III. NPR: NPR (NR7-500P) is spread a top thick BARC layers with same recipe as part III in section 2.3.

IV. IL: IL is performed to make the elliptical hole pattern in the NPR layer with same recipe as part IV in section 2.3 as shown in Fig. 2.12 (a).



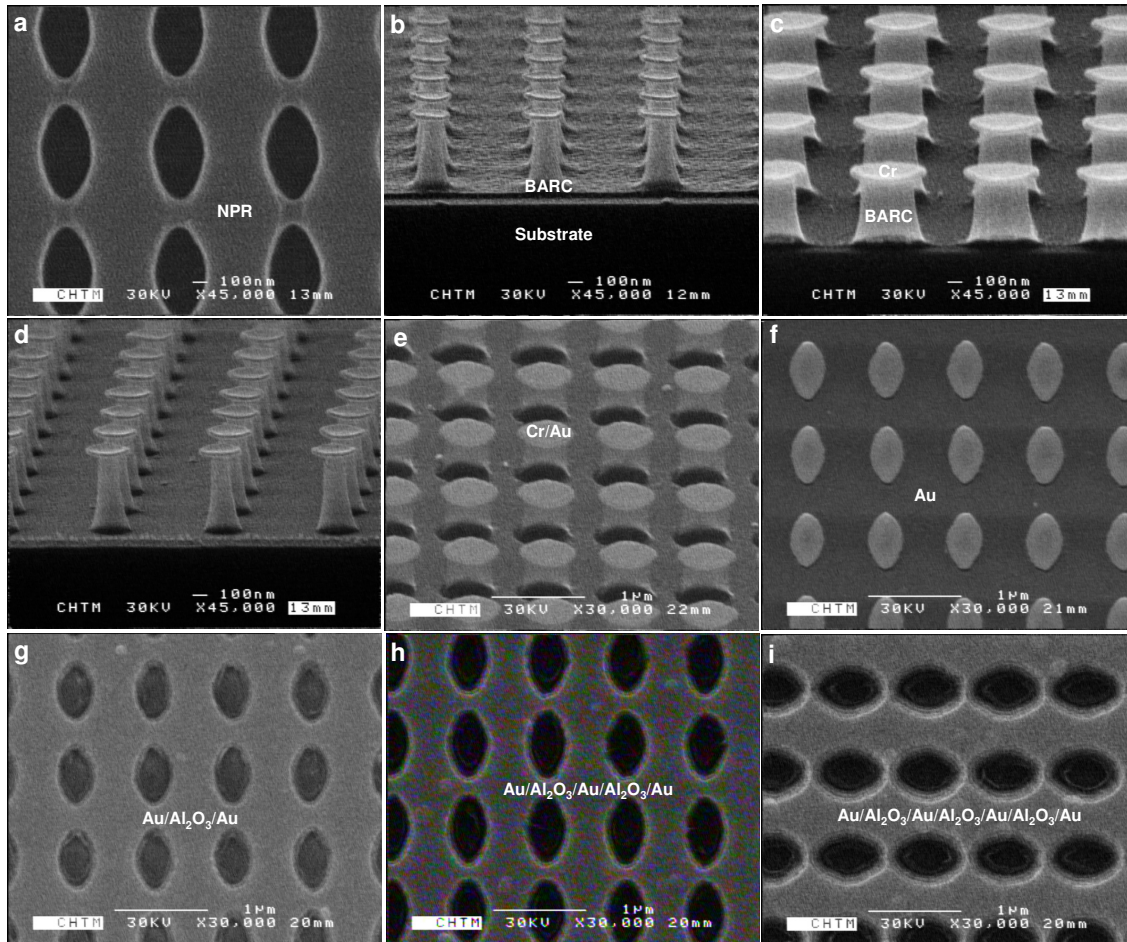


Fig. 2.12 SEM images of fabrication procedure for multifunctional layered elliptical NIMs. (a) IL-2D elliptical hole array in PR layer on thick BARC layer. (b)-(d) Anisotropic RIE etch, resulting in tall BARC posts. (e) Tilt view. (f) Top view of samples after first Au e-beam deposition. Top view of elliptical NIMs with (g) one, (h) two, and (i) three functional layers.

V. Selective etching mask: After the PR pattern is defined, a 25-nm thick layer of chromium (Cr) as a selective etch mask is deposited on the developed sample using e-beam evaporator with same recipe as part V of section 2.2, followed by a liftoff processing with acetone to remove the PR layer.

VI. Etching processing: More anisotropic  $O_2$  plasma-RIE is carried out to transfer the Cr pattern into thick BARC as shown in Fig. 2.12 (b)-(d). Figure 2.12 (b) shows that BARC layer remains between elliptical posts, resulting from not appropriate etching time.

VII. Consecutive e-beam evaporations of Au/ $Al_2O_3$ : As mentioned above, one to three functional layers are deposited with same condition as part V in section 2.2.

VIII. Removal of BARC posts: Same recipe as part VI in section 2.2, which leads to one to three functional layered elliptical NIMs structures as shown in Fig. 2.12 (g)-(i).

## **2.5 Fabrication of Ultrafast Optical Switching device with NIM**

The ultrafast optical switching device with one-functional layered elliptical NIM consists of a BK7 glass substrate with silver/amorphous silicon/silver (Ag/ $\alpha$ -Si/Ag) layers with a two-dimensional square periodic array of elliptical holes penetrating all three layers. A schematic view of brief processing steps to fabricate the ultrafast optical switching device with one-functional layered elliptical NIM is as shown in Fig. 2.13. As the main different process from section 2.2, polymethyl methacrylate layer is used as a sacrificial layer for liftoff processing in final, in addition to e-beam deposition of dielectric film used as a protection.



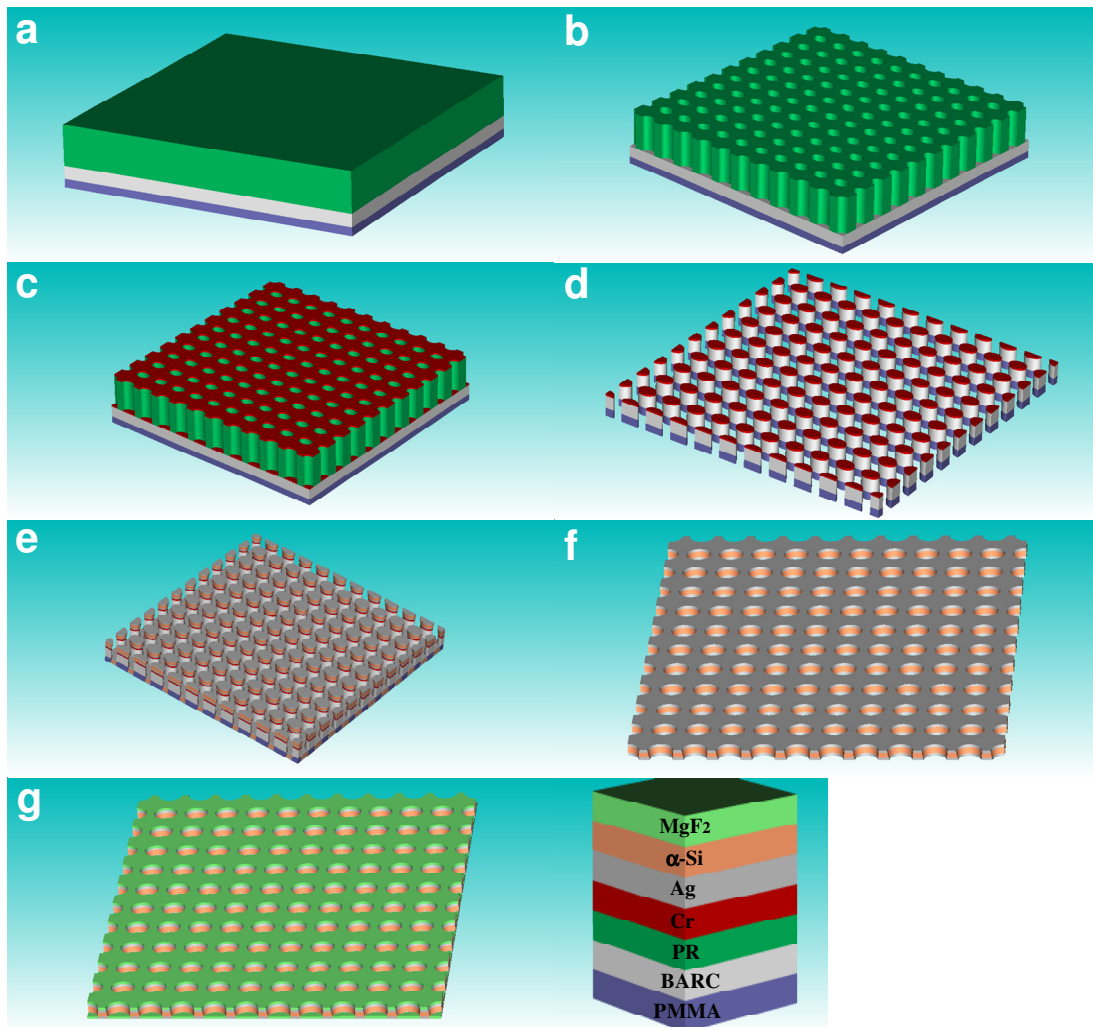


Fig. 2.13 Schematic view of fabrication procedure. (a) Coat the PMMA, ARC and NPR in sequence. (b) Patterning of 2D hole array in PR layer by IL. (c) e-beam evaporation of Cr as the selective etching mask. (d)  $O_2$  plasma RIE process into BARC and PMMA layer after liftoff process. (e) e-beam evaporation of  $Ag/\alpha$ -Si/ $Ag$ . (f) Liftoff process with acetone. (g) e-beam deposition of magnesium fluoride ( $MgF_2$ ).

I. Clean substrate: BK7 glass substrate ( $2.5 \times 2.5 \text{ cm}^2$ ) is cleaned with same recipe as part I in section 2.2.

II. Polymethyl methacrylate (PMMA): PMMA (MicroChem: 950 PMMA 2% in Anisole) is spun onto the wafer at 1500 rpm for 30 s, followed by hotplated-baked at  $180^\circ\text{C}$  for 60 s (thickness is about 100 nm). This PMMA sacrificial layer is used to remove the BARC/PMMA posts in the part IX.

III. BARC: BARC (XHRIC-16) is spun onto the wafer with same recipe as part II in section 2.2.

IV. NPR: NPR (NR7-500P) is spread a top thick BARC layers with same recipe as part III in section 2.3.

V. IL: IL is carried out to produce the elliptical hole pattern in the NPR layer with same recipe as part IV in section 2.3 as shown in Fig. 2.14 (a), (b).

VI. Selective etching mask: a 25-nm thick layer of Cr is deposited with same recipe as part V of section 2.2, followed by a liftoff with acetone to remove the PR layer. During this liftoff, the PMMA layer was protected by the layer of BARC, resulting in an array of elliptical Cr dots atop the BARC and PMMA layer.

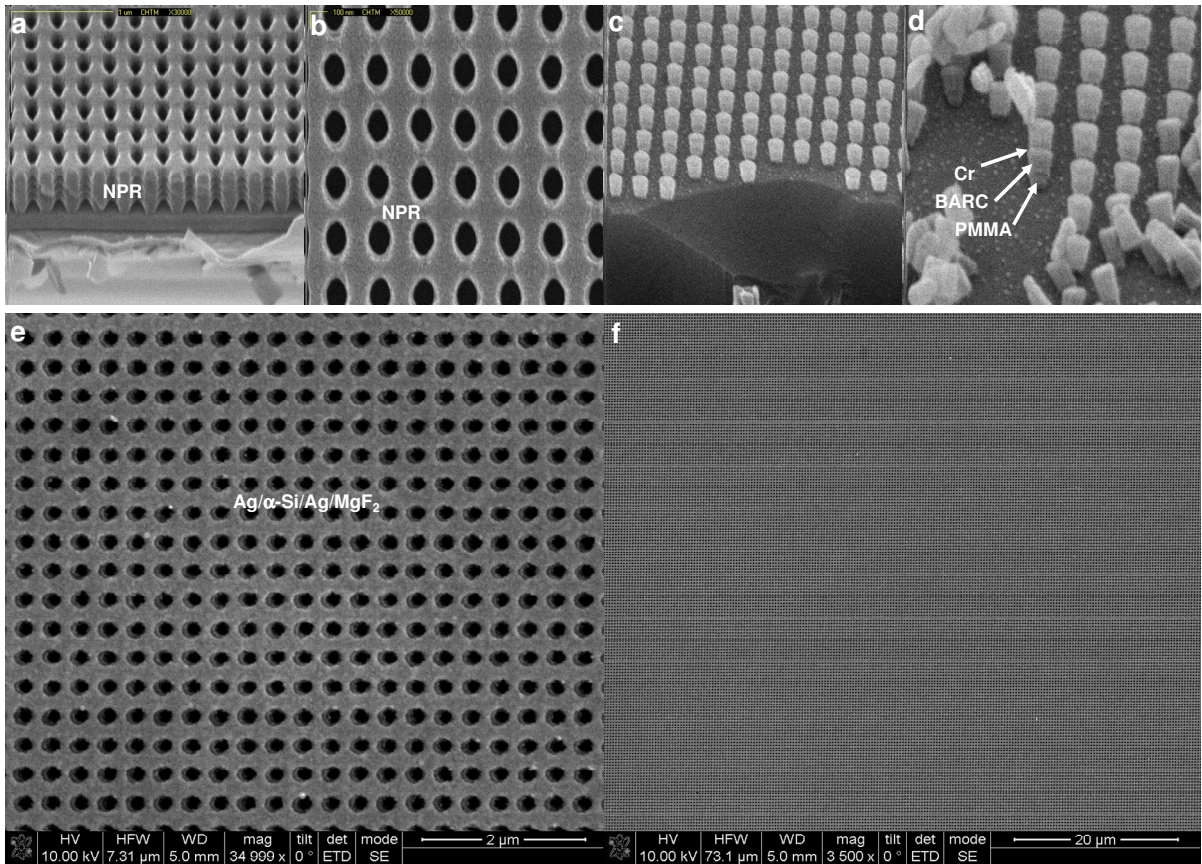


Fig. 2.14 SEM images of fabrication procedure for ultrafast optical switching device with elliptical NIM. (a) Tilt view. (b) Top view of 2D elliptical hole array in PR layer on the BARC/PMMA layer by IL. (c), (d) Anisotropic RIE etch, resulting in Cr/BARC/PMMA posts. (e), (f) Top view of completely fabricated device.

VII. Etch: Using Cr dots as a selective etching mask, a predominately anisotropic O<sub>2</sub> plasma-RIE with slight isotropic component is used to etch through the BARC and PMMA to the substrate while generating a small undercut for the subsequent liftoff process, which is need to be careful due to the interface between BARC and PMMA as shown in Fig. 2.14 (c), (d). This work was done at the Center for Integrated Nanotechnologies (CINT), so that different etching recipe from

previous fabrication was used at RF power (200W), O<sub>2</sub> gas (50 sccm) and O<sub>2</sub> pressure (200 mTorr).

VIII. e-beam evaporation of constituent materials: e-beam deposition of Ag is performed at the Center for High Technology Materials (CHTM) with same recipe as part V, section 2.2 and  $\alpha$ -Si is deposited at CINT with a pressure of the order of  $10^{-7}$  Torr, 0.05 nm/s and carefulness to reduce the shadow effect such as the sample-position at sample-holder and position of sample holder in e-beam evaporator chamber.

IX. Liftoff processing: Ag/a-Si/Ag on top of Cr/BARC/PMMA posts is removed by acetone using the PMMA sacrificial layer instead of a high pressure, isotropic O<sub>2</sub> plasma ash (in section 2.2, 2.3 and 2.4) due to potentially damage the Ag metal surface.

X. Dielectric film deposition: A final blanket, e-beam deposited magnesium fluoride (MgF<sub>2</sub>) layer served as a protection layer, isolating the Ag from oxidation during measurement (optical pump).

## 2.6 References

1. S. Zhang, W. Fan, N. C. Panoiu, K. J. Malloy, R. M. Osgood, and S. R. J. Brueck, "Experimental demonstration of near-infrared negative-index metamaterials," *Phys. Rev. Lett.* **95**, 137404 (2005).
2. V. M. Shalaev, W. Cai, U. K. Chettiar, H-K. Yuan, A. K. Sarychev, V. P. Drachev, and A. V. Kildishev, "Negative index of refraction in optical metamaterials," *Opt. Lett.* **30**, 3356-3358 (2005).
3. S. Zhang, W. Fan, K. J. Malloy, S. R. J. Brueck, N.-C. Panoiu, and R. M. Osgood, "Demonstration of metaldielectric negative-index metamaterials with improved performance at optical frequencies," *J. Opt. Soc. Am. B* **23**, 434-438 (2006).
4. G. Dolling, C. Enkrich, W. Wegener, C. M. Soukoulis, and S. Linden, "Low-loss negative-index metamaterial at telecommunication wavelengths," *Opt. Lett.* **31**, 1800-1802 (2006).
5. Z. Ku and S. R. J. Brueck, "Comparison of negative refractive index materials with circular, elliptical and rectangular holes," *Opt. Express* **15**, 4515-4522 (2007).
6. J. Valentine, S. Zhang, T. Zentgraf, E. Ulin-Avila, D. A. Genov, G. Bartal, and X. Zhang, "Three-dimensional optical metamaterial with a negative refractive index," *Nature* **455**, 376-379 (2008).
7. S. Linden, C. Enkrich, M. Wegener, J. Zhou, T. Koschny, and C. M. Soukoulis, "Magnetic response of metamaterials at 100 Terahertz," *Science* **306**, 1351-1353 (2004).
8. S. Zhang, W. Fan, A. Frauenglass, B. Minhas, K. J. Malloy, and S. R. J. Brueck, "Demonstration of Mid-Infrared Resonant Magnetic Nanostructures exhibiting a negative permeability," *Phys. Rev. Lett.* **94**, 037402 (2005).
9. N. Liu, L. Fu, S. Kaiser, H. Schweizer, and H. Giessen, "Plasmonic building blocks for magnetic molecules in threedimensional optical metamaterials," *Adv. Mater.* **20**, 3859-3865 (2008).
10. E. M. Rabinovich, J. T. Thompson, X. C. Long, S. R. J. Brueck, L. M. Tender, R. K. Jain, and G. P. Lopez, "Fibers with surface Plasmon waves and an internal grating for chemical and biological sensors," *Abstracts of Papers of the American Chemical Society* **213**, 55 (1997).
11. H. F. Ghaemi, Tineke Thio, D. E. Grupp, T. W. Ebbesen, and H. J. Lezec, "Surface plasmons enhance optical transmission through subwavelength holes," *Phys. Rev. B* **58**, 6779 (1998).

12. M. J. O'Brien, V. H. Perez-Luna, S. R. J. Brueck, and G. P. Lopez, "A surface Plasmon resonance array biosensor based on spectroscopic imaging," *Biosensors & Bioelectronics* **16**, 97 (2001).
13. H. J. Lezec, A. Degiron, E. Devaux, R. A. Linke, L. Martin-Moreno, F. J. Garcia-Vidal, and T. W. Ebbesen, "Beaming Light from a Subwavelength Aperture," *Science* **297**, 820-822 (2002).
14. W. J. Fan, S. Zhang, B. K. Minhas, K. J. Malloy, and S. R. J. Brueck, "Enhanced infrared transmission through subwavelength coaxial metallic arrays," *Phys. Rev. Lett.* **94**, 033902 (2005).
15. W. J. Fan, S. Zhang, K. J. Malloy, and S. R. J. Brueck, "Enhanced mid-infrared transmission through nanoscale metallic coaxial-aperture arrays," *Optics Express* **13**, 4406 (2005).
16. S. Y. Lin, J. G. Fleming, D. L. Hetherington, B. K. Smith, R. Biswas, K. M. Ho, M. M. Sigalas, W. Zubrzycki, S. R. Kurtz, and Jim Bur, "A three-dimensional photonic crystal operating at infrared wavelengths," *Nature* **394**, 251 (1998).
17. O. Painter, R. K. Lee, A. Scherer, A. Yariv, J. D. O'Brien, P. D. Dapkus, and I. Kim, "Two-dimensional photonic band-gap defect mode laser," *Science* **284**, 819 (1999).
18. J. G. Fleming, S. Y. Lin, I. El-Kady, R. Biswas, and K. M. Ho, "All-metallic three-dimensional photonic crystals with a large infrared bandgap," *Science* **417**, 52 (2002).
19. A. Yariv, Y. Xu, and S. Mookherjea, "Transverse Bragg resonance laser amplifier," *Opt. Lett.* **28**, 176-178 (2003).
20. J. J. Wierer, M. R. Krames, J. E. Epler, N. F. Gardner, J. R. Wendt, M. M. Sigalas, S. R. J. Brueck, D. Li, and M. Shagam, "III-Nitride LED's with photonic crystal structures," *Proc. SPIE* **5739**, 102-107 (2005).
21. J. L. Bradshaw, J. D. Bruno, J. T. Pham, D. E. Wortman, S. Zhang, and S. R. J. Brueck, "Single-longitudinal-mode emission from interband cascade DFB laser with a grating labricated by interferometric lithography," *Proc. Inst. Electr. Eng. - Optoelectron.* **150**, 288-292 (2003).
22. S. H. Zaidi and S. R. J. Brueck, "Multiple-exposure interferometric lithography," *J. Vac. Sci. Tech. B* **11**, 658 (1993).
23. X. L. Chen, S. H. Zaidi, S. R. J. Brueck, and D. J. Devine, "Interferometric lithography of sub-micrometer sparse hole arrays for field-emission display applications," *J. Vac. Sci. Tech. B* **14**, 3339 (1996).
24. S. R. J. Brueck, S. H. Zaidi, X. Chen, and Z. Zhang, "Interferometric lithography-from periodic arrays to arbitrary patterns" *Microelectronic Engineering* **42**, 145 (1998).

25. M. J. O'Brien, P. Bisong, L. K. Ista, E. M. Rabinovich, A. L. Garcia, S. S. Sibbett, G. P. Lopez, and S. R. J. Brueck, "Fabrication of an integrated nanofluidic chip using interferometric lithography," *J. Vac. Sci. Tech. B* **21**, 2941 (2003).
26. F. J. Hohn, A. D. Wilson, and P. Coane, "Advanced electron-beam lithography for 0.5- $\mu\text{m}$  to 0.25- $\mu\text{m}$  device fabrication," *IBM Journal of Research and Development* **32**, 514 (1988).
27. M. Okano, H. Kikuta, Y. Hirai, K. Yamamoto, and T. Yotsuya, "Optimization of diffraction gratings profiles in fabrication by electron-beam lithography," *Applied Optics* **43**, 5137 (2004).
28. A. Datta, Y. R. Wu, and Y. L. Wang, "Gas-assisted focused-ion-beam lithography of a diamond (100) surface," *App. Phys. Lett.* **75**, 2677 (1999).
29. L. Bach, W. Kaiser, J. P. Reithmaier, A. Forchel, M. Gioannini, V. Feies, and I. Montrosset, "22-GHz modulation bandwidth of long cavity DBR laser by using a weakly laterally coupled grating fabricated by focused ion beam lithography," *IEEE Photonics Technology Letters* **16**, 18 (2004).
30. S. Y. Chou, R. P. Krauss, and P. J. Renstrom, "Imprint lithography with 25-nanometer resolution," *Science* **272**, 85 (1996).
31. S. Y. Chou, C. Keimel, and J. Gu, "Ultrafast and direct imprint of nanostructures in silicon," *Nature*, **417**, 835 (2002).
32. C. V. Shank and R. V. Schmidt, "Optical technique for producing 0.1- $\mu\text{m}$  periodic surface structures," *Appl. Phys. Lett.* **23**, 154 (1973).
33. W. T. Tsang and S. Wang, "Simultaneous exposure and development technique for making gratings in positive photoresist," *Appl. Phys. Lett.* **23**, 196 (1974).
34. J. A. Hoffnagle, W. D. Hinsberg, M. Sanchez, and F. A. Houle, "Liquid immersion deep ultraviolet interferometric lithography," *J. Vac. Sci. Tech. B* **17**, 3306-3309 (1999).
35. M. Switkes and M. Rothschild, "Immersion lithography at 157 nm," *J. Vac. Sci. Tech. B* **19**, 2353-2356 (2001).
36. J. H. Burnett and S. G. Kaplan, "Measurement of the refractive index and thermo-optic coefficient of water near 193 nm," *J. Microlith. Microfab. Microsys.* **3**, 68-72 (2004).
37. S. R. J. Brueck, "Optical and interferometric lithography-nanotechnology enablers," *Proc. IEEE* **93**, 1704-1721(2005).

# Chapter 3 Comparison of Structural Impact on the Negative-Index Metamaterials

## 3.1 Introduction

The initial demonstrations of negative-index metamaterials (NIMs) [1,2] along with theoretical predictions of potential applications such as imaging beyond the diffraction limit [3,4] have led to intense interest in extending these results to shorter near-infrared and visible wavelengths. Over the past few years, there have been theoretical efforts towards the realization of short wavelength magnetic metamaterials [5] and NIMs [6,7], and experimental demonstration of magnetic metamaterials at far-, mid-, near-infrared and visible wavelengths [8-12] and near-infrared NIMs [13,14].

Recently, Zhang *et al.* proposed [13] and demonstrated [15] a NIM structure composed of two parts: the negative electric permittivity ( $\epsilon$ ) results from an array of thin metal wires parallel to the direction of electric field and the negative magnetic permeability ( $\mu$ ) from a pair of finite-width metal stripes separated by a dielectric layer along the direction of the incident magnetic field. The resulting structure is a 2D array of holes penetrating completely through a metal-dielectric-metal film stack. In the initial experiments, circular holes were used, which led to relatively wide metal stripes contributing to the permittivity, to a large negative  $\epsilon$ , and a significant impedance mismatch between the metamaterial and the incident and transmitted media. The structure was metal-like and most of the incident energy was reflected, with only about 5% transmission in the negative refractive index spectral region. The experimental figure of merit [ $\text{FOM} \equiv -\text{Re}(n) / \text{Im}(n)$ ] was only about 0.5 for this structure. This result was improved



using elliptical apertures with narrower metal stripes parallel to the electric field, with about 20% transmission and a FOM of about 0.9 [16]. Dolling *et al.* [17] introduced a variant with rectangular apertures (called the fishnet structure) and achieved both a higher transmission (~65%) and an improved FOM (~3) and argued that the improvement was due to the improved material properties (silver versus gold) and to the square structure which provided a constant width across the aperture in contrast to the varying chord of the elliptical structure. However, their experiment used a different material system (silver- magnesium fluoride-silver in place of gold-sapphire-gold) and was resonant at a different wavelength (1.5  $\mu\text{m}$  instead of 2  $\mu\text{m}$ ) making a detailed understanding of the structural impact on the metamaterial properties difficult. In this chapter we fabricate, in the gold (Au) – sapphire ( $\text{Al}_2\text{O}_3$ ) – gold (Au) material system, a series of three structures with 2D array of circular, elliptical and rectangular apertures resonant at similar wavelengths to allow a direct comparison of the metamaterial properties. We find that the impact of the geometry of the individual apertures is most dramatic on the impedance and that there is only a weak dependence of the FOM on the aperture geometry.

## **3.2 Design of Circular, Elliptical and Rectangular NIMs**

The sample structure consists of a BK7 glass substrate with a pair of metallic films (30-nm thick layers of Au) separated by a dielectric film (60-nm thick layer of  $\text{Al}_2\text{O}_3$ ), with a 2-dimensional (2D) square periodic array of circular, elliptical and rectangular holes penetrating through the multilayer structure. Schematic representations of these structures are shown in Fig. 3.1.

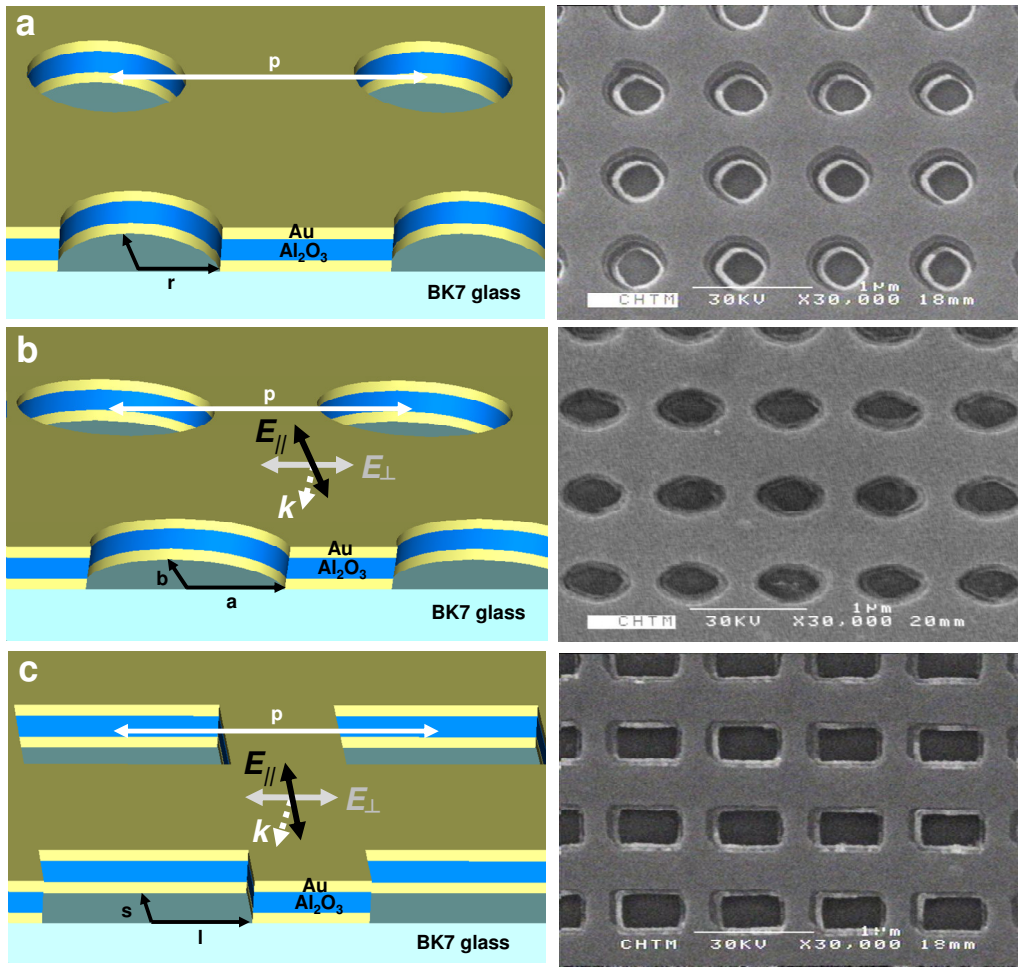


Fig. 3.1 Tilted schematic and top view of SEM images of NIM structures with (a) circular (b) elliptical (c) rectangular holes. In (b) and (c), the polarization can be directed along either the major (long) or the minor (short) axis, which are denoted  $E_{\parallel}$  (electric field parallel to the minor/short axis) and  $E_{\perp}$  (electric field perpendicular to the minor/short axis) polarization, respectively.

The detailed fabrication procedures for the circular/elliptical/rectangular holes through the multilayer are described in section 2 and section 3 of Chapter 2, in addition that IL has been used to fabricate these structures, resulting in very good uniformity across a large area [18].

The geometrical parameters and measured dimensions are indicated in tilted view in Fig. 3.1 and listed in Table 3.1. The orthogonal pitches of the 2D gratings are both 823 nm. The thicknesses of Au/Al<sub>2</sub>O<sub>3</sub>/Au are 30/60/30 nm, respectively. The circular hole size is formed with a diameter ( $2r$ ) of 400 nm; elliptical hole size is formed with 534 nm, 340 nm in major ( $2a$ ) and minor ( $2b$ ) axis, respectively; rectangular hole size is formed with 528 nm, 339 nm in long ( $2l$ ) and short ( $2s$ ) axis, respectively.

	Circular NIM	Elliptical NIM	Rectangular NIM
Pitch ( $p$ )	823	823	823
Hole size	400 ( $2r$ )	534 ( $2a$ ) / 340 ( $2b$ )	528 ( $2l$ ) / 339 ( $2s$ )
Thickness (Au/Al <sub>2</sub> O <sub>3</sub> /Au)	30/60/30	30/60/30	30/60/30

Table 3.1 The geometrical parameters of circular, elliptical and rectangular NIMs (all dimensions in nm)

### 3.3 Measurement and Simulation

The transmission of these samples across the near-infrared wavelength region ( $\sim 2 \mu\text{m}$ ) was measured at normal incidence using Fourier-transform infrared spectroscopy (FTIR). The measured transmission spectra were normalized to the spectrum of a bare BK7 glass standard. In the case of the symmetric NIM with circular holes, an unpolarized FTIR beam was used to

measure the transmission. For the asymmetric structures (elliptical/rectangular NIMs), the incident electric field was either parallel to the narrower stripe width between apertures ( $E_{\parallel}$ ), or parallel to the wider width between apertures and perpendicular to the narrow direction ( $E_{\perp}$ ). The transmission spectra of samples with circular, elliptical and rectangular holes for both  $E_{\parallel}$  and  $E_{\perp}$  are shown in Fig. 3.2.

A rigorous coupled wave analysis (RCWA) simulation, a commonly used algorithm to compute the spectra of transmission and reflectance of periodic structures [19,20], was used to calculate the transmission spectra to understand properties of these different structures such as effective refractive index, the FOM, impedance, effective permittivity (permeability) and so on. The present version of the simulation software is restricted to rectangular holes. Therefore, for the circular case, the aperture was modeled as a square with the same open area as the circle. For the elliptical case, a rectangular geometry was calculated with open area and the ratio of side length the same as the area and the major/minor axis ratio of the ellipse. Metal/dielectric/metal thicknesses of 30/60/30 nm were used in the simulation. This code was used to analyze the initial circular aperture NIM and a detailed comparison of experiment and simulation for amplitude and phase of transmission and reflection was presented [13]. Zhang and Dolling have both measured the amplitude and phase of reflection and transmission and demonstrated that this modeling procedure gives a good fit to the experimentally measured index and impedance (or permittivity and permeability); those measurements are not repeated here [13,17].

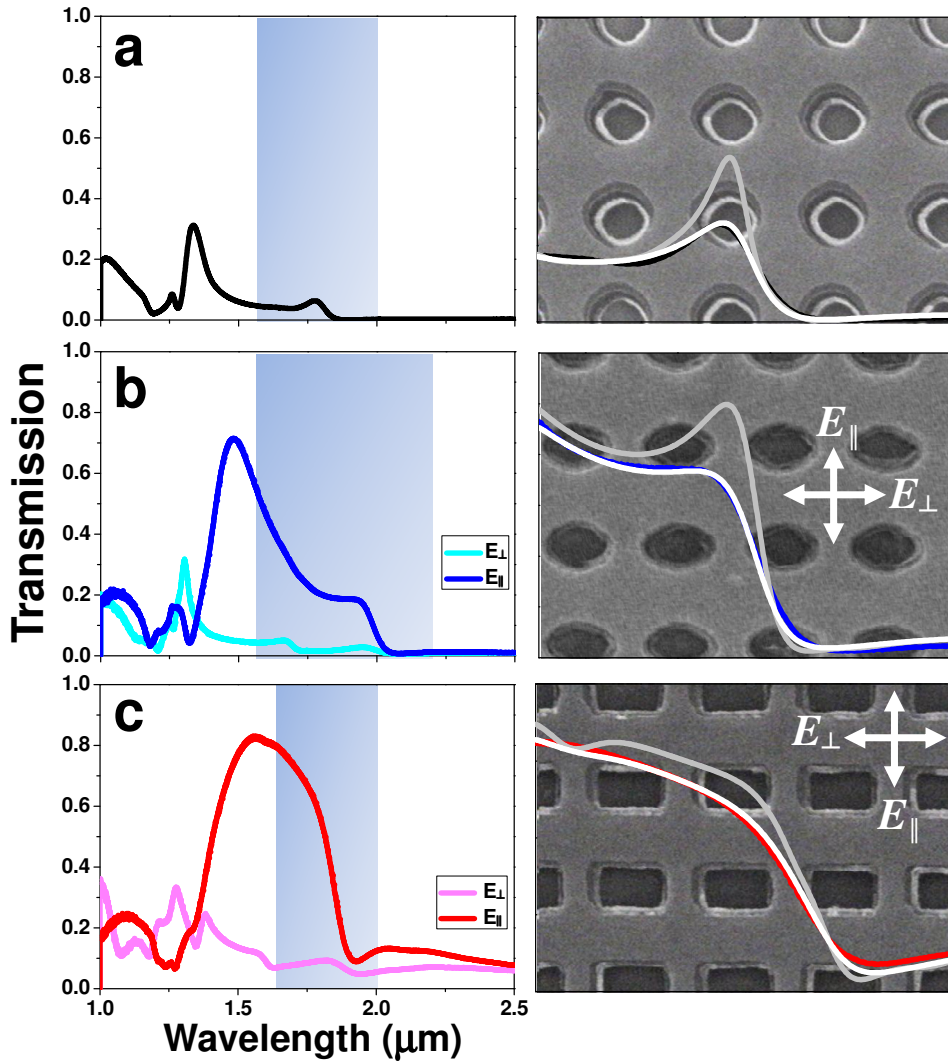


Fig. 3.2 First column shows the measured normal incident transmission spectra for  $E_{\parallel}$  and  $E_{\perp}$  polarization using FTIR. NIMs with (a) circular (b) elliptical (c) rectangular holes. Shaded areas represent wavelength regions of negative refractive index. Second column shows a comparison of  $E_{\parallel}$  transmission spectra calculated by RCWA model and measurement across the negative refractive index region with one ( $1 \times \omega_c$ ) and two times ( $2 \times \omega_c$ ) the bulk scattering frequency in a Drude model for Au permittivity.

A simple Drude model for the Au permittivity was used, which is a good approximation to experiment values in the near-IR. The permittivity is given as

$$\epsilon_{Au} = 1 - \frac{\omega_p^2}{\omega(\omega + i\gamma \cdot \omega_c)} \quad (3.1)$$

where  $\omega_p$  (plasma frequency) =  $1.37 \times 10^{16}$  Hz and  $\omega_c$  (bulk scattering frequency) =  $4.1 \times 10^{13}$  Hz [21].  $\gamma$  is a fitting parameter to account for additional scattering in the thin, multi-domain films as well as for any sample inhomogeneity across the  $\sim 1 \text{ cm}^2$  measurement area [13]. [Spectra measured on small areas across the sample show very good uniformity with only small variations in spectra, much less than the observed structural variations]. Figure 3.2 shows that the structure (dips and peaks) in the region of negative refractive index becomes less distinct as  $\gamma$  is increased. Two times the scattering frequency ( $\gamma=2$ ) of bulk Au was found to give the best fit between experiment and simulation over the range of wavelengths of interest for all three structures as shown in Fig. 3.2. This allows us to extract the effective refractive index ( $n_{\text{eff}}$ ), impedance ( $\xi_{\text{eff}}$ ), permittivity ( $\epsilon_{\text{eff}}$ ) and permeability ( $\mu_{\text{eff}}$ ) over the range of negative refraction from simulation. The effective refractive index and impedance were extracted from the complex coefficients of transmission and reflection obtained by a RCWA simulation as shown in Fig. 3.3 (a), (b) and Fig. 3.4 (a), (b) [5,22]. The effective refractive indices ( $n_{\text{eff}}$ ) of circular, elliptical and rectangular NIMs are shown in Fig. 3.3 (a), (b). For the three different NIM structures, a negative refractive index is obtained over a range of wavelengths (1.56  $\mu\text{m}$  to 2  $\mu\text{m}$ , 1.64  $\mu\text{m}$  to 2.2  $\mu\text{m}$  and 1.64  $\mu\text{m}$  to 1.98  $\mu\text{m}$  for circular, elliptical and rectangular NIMs, respectively).

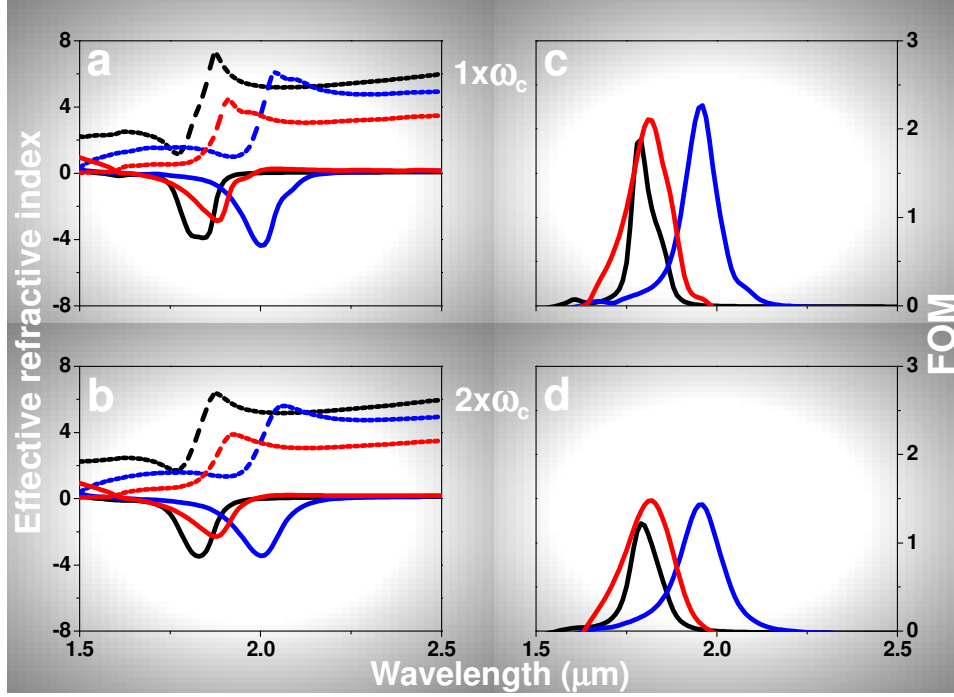


Fig. 3.3 (a), (b) Real (solid lines) and imaginary (dashed lines) parts of the effective refractive index using the scattering frequencies one ( $1 \times \omega_c$ ) and two times ( $2 \times \omega_c$ ) that of bulk Au, respectively. (c), (d) FOMs using  $1 \times \omega_c$  and  $2 \times \omega_c$ . The same color conventions as Fig. 3.2 is followed (black: circular NIM, blue: elliptical NIM and red: rectangular NIM).

For a smaller scattering frequency ( $\gamma = 1$ ), larger real parts and smaller imaginary parts of effective refractive index are obtained as shown in Fig. 3.3 (a). For simulation with  $\gamma = 2$ , the minimum real parts of effective index  $[-\text{Re}(n_{\text{eff}})]$  are larger than the imaginary parts of the index  $[\text{Im}(n_{\text{eff}})]$  as shown in Fig. 3.3 (b), e.g.  $\text{FOM} > 1$  which is improved compared with previous reports [13,16]. The FOMs are plotted in Fig. 3.3 (c), (d). For thin metal lines along the electric field,  $E_{\parallel}$  polarization, electric field along the narrow stripes, the FOMs using  $\gamma = 2$  are 1.22, 1.43 and 1.48 for circular, elliptical and rectangular NIMs, respectively. In Fig. 3.3 (d), the circular

structure has a somewhat smaller FOM, however the results for the elliptical and fishnet structures (rectangular structure) are quite similar. These FOMs for circular and elliptical structures are higher than the results in Refs [13,16], suggesting that the present samples have an improved homogeneity. For reference, peaks of FOMs using  $\gamma = 1$  are approximately 1.88, 2.26 and 2.11 in Fig. 3.3 (c). As a result of uncertainty in the modeling (particularly the use of a rectangular structure to model all three experimental samples), these results should be interpreted only qualitatively to suggest that there is not a strong structural dependence of the FOM.

Over the wavelength range of negative refraction, the effective impedance ( $\xi_{\text{eff}}$ ) for each structure is shown in Fig. 3.4, the real part of the impedance for the fishnet structure is closer to  $\sqrt{\xi_{\text{air}} \xi_{\text{glass}}} \sim 1.2$  required to antireflection coating the glass-air interface, which indicates that rectangular NIM > elliptical NIM > circular NIM is the order of both higher transmission and better impedance matching between the NIMs and the superstrate ( $\xi_{\text{air}} = 1$ ), substrate ( $\xi_{\text{substrate}} = 1.5$ ) combination. In Fig. 3.2 (c), the transmission in the region of negative index is as high as ~80% with rectangular holes, which is improved in comparison with the low transmission obtained in NIM with circles and ellipses due to better impedance matching as shown in Fig. 3.4 (a), (b). The calculated effective permittivity ( $\epsilon_{\text{eff}}$ ) and permeability ( $\mu_{\text{eff}}$ ), shown in Fig. 3.4 (c), (d) and Fig. 3.5, can be extracted from the effective refractive index ( $n_{\text{eff}}$ ) and impedance ( $\xi_{\text{eff}}$ ) by simple calculation ( $\mu_{\text{eff}} = n_{\text{eff}} \times \xi_{\text{eff}}$  and  $\epsilon_{\text{eff}} = n_{\text{eff}} / \xi_{\text{eff}}$ ).



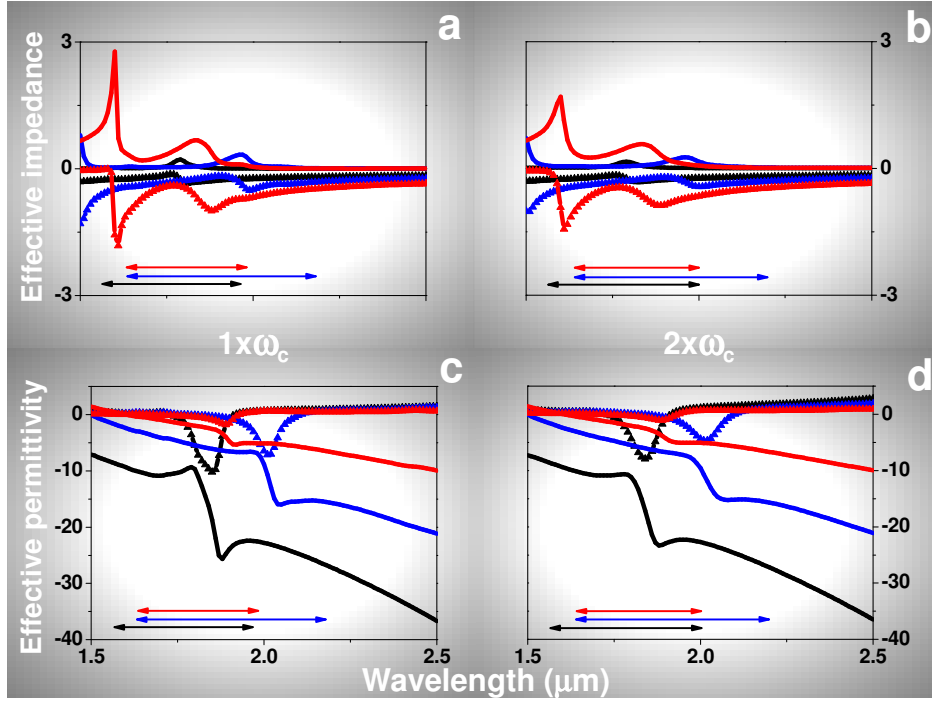


Fig. 3.4 (a), (b) The calculated effective impedance ( $\xi_{\text{eff}}$ ). (c), (d) Calculated effective permittivity ( $\epsilon_{\text{eff}}$ ). Real parts of  $\xi_{\text{eff}}$  and  $\epsilon_{\text{eff}}$  are indicated by solid lines and imaginary parts are plotted with symbols. The same color convention as Fig. 3.2 is followed. Arrows represent the negative refractive index region of circular, elliptical and rectangular NIMs, respectively.

The effective permittivity, Fig. 3.4 (c), (d) resembles the permittivity of a dilute Drude metal, in addition that the real parts of the effective permeability show a resonant modulation around 1.8  $\mu\text{m}$  (for circular and rectangular holes) and 2  $\mu\text{m}$  (for elliptical holes), and the imaginary parts show peaks, reflecting the magnetic resonance behavior.  $\text{Re}(\mu_{\text{eff}})$  has negative values for all three structures for  $\gamma = 1$  whereas for  $\gamma = 2$  the minimum value of  $\text{Re}(\mu_{\text{eff}})$  of circular NIM is not negative; it is negative for the elliptical and rectangular structures. (In Ref. [13], only results for  $\gamma = 3$  were presented and a negative  $\text{Re}(\mu_{\text{eff}})$  was not achieved). Figure 3.4 (c), (d) and Fig. 3.5

indicate that the influence of the scattering frequency ( $\gamma$ ) is predominantly on the effective permeability ( $\mu_{\text{eff}}$ ) as expected.

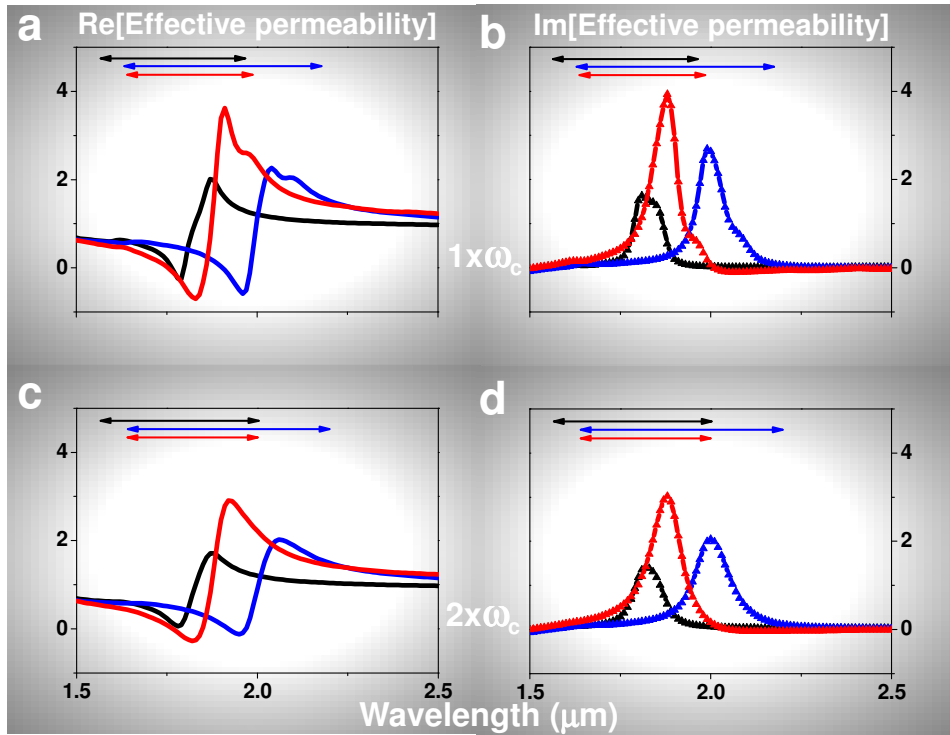


Fig. 3.5 (a)-(d) The effective permeability ( $\mu_{\text{eff}}$ ). The color convention is the same as in Fig. 3.2.

### 3.4 Summary

In summary, the impact of the geometry (circular, elliptical and rectangular apertures) and of metal electron scattering rates on the optical properties of NIMs has been examined. The experimental results are in good agreement with a RCWA simulation and with the progression of improved impedance matching in moving from circular to elliptical to rectangular apertures. A transmission of over 80% was achieved in the negative index region for the rectangular aperture

geometry. The FOMs are very similar for all three geometries with NIMs with ellipses and rectangular structures being about 20% higher than for circular structures. The simulations were restricted to rectangular structures, and while excellent agreement was achieved with measured transmission spectra, additional simulations that fully take into account the impacts of the actual non-rectangular aperture geometries are need to confirm the effects of structure on the FOM.

### 3.5 References

1. D. R. Smith, W. J. Padilla, D. C. Vier, S. C. Nemat-Nasser, and S. Schultz, "Composite medium with simultaneously negative permeability and permittivity," *Phys. Rev. Lett.* **84**, 4184-4187 (2000).
2. R. A. Shelby, D. R. Smith, and S. Schultz, "Experimental verification of a negative index of refraction," *Science* **292**, 77-79 (2002).
3. V. G. Veselago, "The electrodynamics of substances with simultaneously negative values of  $\epsilon$  and  $\mu$ ," *Sov. Phys. USP.* **10**, 509 (1968).
4. J. B. Pendry, "Negative refraction makes a perfect lens," *Phys. Rev. Lett.* **85**, 3966-3969 (2000).
5. S. O'Brien and J. B. Pendry, "Magnetic activity at infrared frequencies in structured metallic photonic crystals," *J. Phys. Condens. Matter* **14**, 6383-6394 (2002).
6. N.-C. Panoiu and R. M. Osgood, "Influence of the dispersive properties of metals on the transmission characteristics of left-handed materials," *Phys. Rev. E* **68**, 016611(2003).
7. N.-C. Panoiu and R. M. Osgood, "Numerical investigation of negative refractive index metamaterials at infrared and optical frequencies," *Opt. Commun.* **233**, 331-337 (2003).
8. S. Zhang, W. Fan, A. Frauenglass, B. Minhas, K. J. Malloy, and S. R. J. Brueck, "Demonstration of Mid-Infrared Resonant Magnetic Nanostructures exhibiting a negative permeability," *Phys. Rev. Lett.* **94**, 037402 (2005).
9. T. J. Yen, W. J. Padilla, N. Fang, D. C. Vier, D. R. Smith, J. B. Pendry, D. N. Basov, and X. Zhang, "Terahertz magnetic response from artificial materials," *Science* **303**, 1494-1496 (2004).
10. N. Katsarakis, G. Konstantinidis, A. Kostopoulos, R. S. Penciu, T. F. Gundogdu, Th. Koschny, M. Kafesaki, E. N. Economou, and C. M. Soukoulis "Magnetic response of split-ring resonators in the far infrared frequency regime," *Opt. Lett.* **30**, 1348-1350 (2005).
11. S. Linden, C. Enkrich, M. Wegener, J. Zhou, T. Koschny, and C. M. Soukoulis, "Magnetic response of metamaterials at 100 Terahertz," *Science* **306**, 1351-1353 (2004).
12. C. Enkrich, F. Pérez-Willard, D. Gerthsen, J. F. Zhou, T. Koschny, C. M. Soukoulis, M. Wegener, and S. Linden "Focused-ion-beam nanofabrication of near-infrared magnetic metamaterials," *Adv. Mat.* **17**, 2547-2549 (2005).

13. S. Zhang, W. Fan, N. C. Panoiu, K. J. Malloy, R. M. Osgood, and S. R. J. Brueck, "Experimental demonstration of near-infrared negative-index metamaterials," *Phys. Rev. Lett.* **95**, 137404 (2005).
14. V. M. Shalaev, W. Cai, U. K. Chettiar, H-K. Yuan, A. K. Sarychev, V. P. Drachev, and A. V. Kildishev, "Negative index of refraction in optical metamaterials," *Opt. Lett.* **30**, 3356-3358 (2005).
15. S. Zhang, W. Fan, K. J. Malloy, S. R. J. Brueck, N.-C. Panoiu, and R. M. Osgood, "Near-infrared double negative metamaterials," *Opt. Express* **13**, 4922-4930 (2005).
16. S. Zhang, W. Fan, K. J. Malloy, S. R. J. Brueck, N.-C. Panoiu, and R. M. Osgood, "Demonstration of metaldielectric negative-index metamaterials with improved performance at optical frequencies," *J. Opt. Soc. Am. B* **23**, 434-438 (2006).
17. G. Dolling, C. Enkrich, W. Wegener, C. M. Soukoulis, and S. Linden, "Low-loss negative index metamaterial at telecommunication wavelengths," *Opt. Lett.* **31**, 1800-1802 (2006).
18. S. R. J. Brueck, "Optical and Interferometric Lithography-Nanotechnology Enablers," *Proc. IEEE* **93**, 1704-1721 (2005).
19. M. G. Moharam and T. K. Gaylord, "Rigorous coupled-wave analysis of planar-grating diffraction," *J. Opt. Soc. Am.* **71**, 811-818 (1981).
20. B. K. Minhas, W. Fan, K. Agi, S. R. J. Brueck, and K. J. Malloy, "Metallic inductive and capacitive grids: theory and experiment," *J. Opt. Soc. Am. A* **19**, 1352-1359 (2002).
21. M. A. Ordal, L. L. Long, R. J. Bell, S. E. Bell, R. R. Bell, R. W. Alexander, and C. A. Ward, "Optical properties of the metals Al, Co, Cu, Au, Fe, Pb, Ni, Pd, Pt, Ag, Ti and W in the infrared and far infrared," *Appl. Opt.* **22**, 1099 (1983).
22. D. R. Smith and S. Schultz, "Determination of effective permittivity and permeability of metamaterials from reflection and transmission coefficients," *Phys. Rev. B* **65**, 195104. (2002).

# Chapter 4 Bi-Anisotropic Effects due to Non-Zero Sidewall-Angle in Negative-Index Metamaterials

## 4.1 Introduction

Artificially structured composite metamaterials consist of sub-wavelength sized structures that exhibit unusual electromagnetic properties, not found in nature. Research on metamaterials that display the properties of negative refraction, artificial magnetism and negative permeability (permittivity) has seen impressive growth since the first experimental verification [1,2] along with theoretical predictions of potential applications [3,4]. One of the most attractive features of metamaterials is to obtain negative refraction, termed left-handed materials (LHMs) or negative-index metamaterials (NIMs), over a specific frequency band. In artificially fabricated materials with permittivity ( $\epsilon = \epsilon' + i\epsilon''$ ) and permeability ( $\mu = \mu' + i\mu''$ ), the necessary condition for achieving a negative index is  $\epsilon' \cdot \mu'' + \mu' \cdot \epsilon'' < 0$  and lower losses are achieved if both the real parts are less than zero  $\epsilon' < 0, \mu' < 0$  [5]. For useful application, interest has been focused on reduction of loss in NIMs. A first candidate to reduce the loss is to design new structured NIMs (optimize the structure) to have negative real parts of  $\epsilon$  and  $\mu$  simultaneously so that losses become small. Another is to approach three dimensional (bulk) rather than planar structures in NIMs to improve the figure of merit [ $FOM \equiv -\text{Re}(n) / \text{Im}(n)$ ], that is, to lower  $\text{Im}(n)$ , by stacking multiple functional layers [6].

The fishnet structured NIM is composed of a 2-dimensional square periodic array of rectangular holes penetrating through a metal-dielectric-metal film stack. The dimension of NIMs with  $N$  functional layers based on the fishnet structure [7] for the optical frequency regime

should be at least below  $\sim 1 \mu\text{m}$  (pitch) and on the order of  $100 \times N \text{ nm}$  (thickness of NIM). In other words, to achieve optical-frequency NIMs, the aspect ratio (height/width) needs to be large. In previous reports the NIMs based on the fishnet structure with negative refractive index at near-infrared and visible frequency were fabricated with aspect ratios of  $\sim 0.4$  and  $\sim 1.4$ , respectively [8,9]. Present fabrication of one- to multiple-functional layered fishnet NIMs largely employs standard semiconductor techniques: conventional lithography (interferometric, e-beam, focused-ion-beam, or nano-imprint), electron beam evaporation, etching, and liftoff processing [8-14]. With the exception of the focused-ion-beam (FIB) processing [12], all reported fishnet NIMs have been fabricated with a sequential deposition of metal and dielectric films followed by a lift-off process. Although FIB is an alternate approach to fabricating NIMs, it also results in a nonzero sidewall angle as discussed in Ref [12]. Several reports have shown that a nonnegligible sidewall angle results from this process sequence [15-17]. This sidewall angle (SWA) results in a bianisotropic optical response, e.g. NIMs with SWAs are not symmetric structures, but rather are bi-anisotropic, exhibiting different reflectivities at normal incidence from the two sides of the film stack. In general, the processing procedure to fabricate the fishnet NIMs is to define the hole-size using a polymeric material, usually by lithographically defining polymer posts, followed by deposition of the constitutive materials and dissolution of the polymer (liftoff processing). This processing (fabrication of posts: multi-layer deposition: liftoff) often gives rise to significant SWAs because as materials accumulate on the tops of the posts that define the structure, each successive film deposition results in a somewhat larger aperture on the bottom metamaterial film, giving rise to a nonzero SWA and to optical bianisotropy as shown in Fig. 4.1 (a), (b). This sidewall angle will vary depending on the height of the sacrificial posts and on the deposition geometry (distance from the source and collimation). Etching approaches to forming

the metamaterial are also subject to top-to-bottom variations of the film stack geometry. This fabrication induced SWA effect requires a modified method to retrieve the effective parameters [18,19] in place of the conventional approach that is appropriate only to symmetric, vertical sidewall structures [20].

The negative permeability of fishnet structures is ascribed to the magnetic response from a cut-wire portion of the structure and the negative permittivity to the electric response in the thin-metal wire portion of the fishnet NIM, which together lead to a negative refractive index [7,11]. However, in a structure with a non-negligible SWA, the cut-wire structure magnetic response induced by  $\vec{H}$  is coupled with an electric response, and, similarly, in thin metal wires the electric response induced by  $\vec{E}$  is coupled with a magnetic response, which gives rise to bianisotropy and to differences in the reflectivity measured from the substrate and superstrate sides of the metamaterial [8,18-19,21-24].

In section 4.2, gold – silicon dioxide – gold (Au – SiO<sub>2</sub> – Au) sandwich fishnet structure with 1- to 5-functional layers (FLs) is modeled with a three dimensional finite integration technique (FIT) approach [25], in addition to modifications to the standard parameter retrieval algorithm. No substrate (multi-functional layered NIMs in symmetric case of an air) is present in the simulation to allow clearer demonstration of the effects of the bi-anisotropy. In section 4.3, the effect of a nonzero SWA on the performance of multiple layer fishnet-structure (one to three FLs) NIMs for an asymmetric case of a glass substrate and an air superstrate [15] is evaluated experimentally. Finally, in section 4.4, we extend these measurements and simulations to the symmetric case of a glass substrate, an index-matching fluid (refractive index-matching liquids, Cargille Lab, Inc.) in the metamaterial spaces, and a glass superstrate as shown in Fig. 4.14. This



symmetric cladding approach provides a clearer observation of the bianisotropic characteristics resulting from the nonzero SWA.

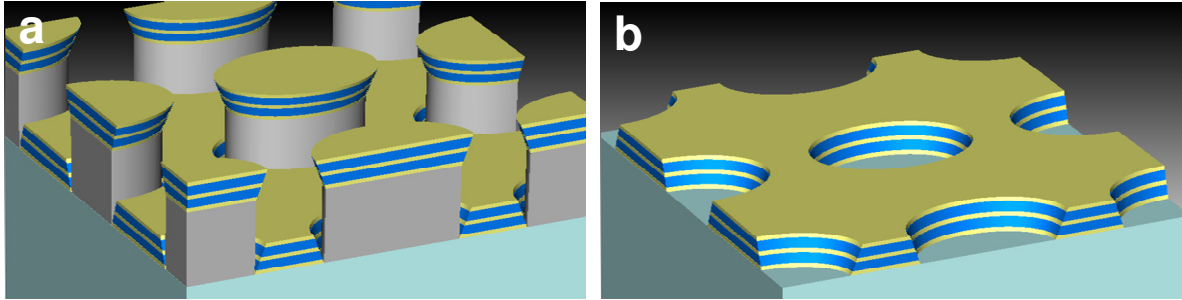


Fig. 4.1 Schematic view of SWA formation mechanism. (a) Illustration of tendency for tops of polymer posts to be larger in e-beam evaporation of constituent materials. (b) Final structure with SWA by liftoff processing.

## 4.2 Numerical Demonstration

### 4.2.1 Design and Dimensions

The geometrical parameters of the multi-functional layered fishnet NIMs are indicated in tilted view in Fig. 4.2 (a) and listed in Table 4.1. The orthogonal pitches of the 2D gratings  $p_x$  (pitch along  $\hat{x}$ -axis) and  $p_y$  (pitch along  $\hat{y}$ -axis) are both fixed at 800 nm. The thicknesses of Au/SiO<sub>2</sub>/Au are fixed at 20/20/20 nm, respectively. The rectangular hole size ( $2a$ ,  $2b$ ) is fixed at 65% (520 nm)/40% (320 nm) of the pitch for long/short sides, that is, the linewidths of the gratings along the  $\hat{x}$ ,  $\hat{y}$  axes are 280/480 nm, respectively. As discussed above, a free floating sample with no substrate is evaluated.

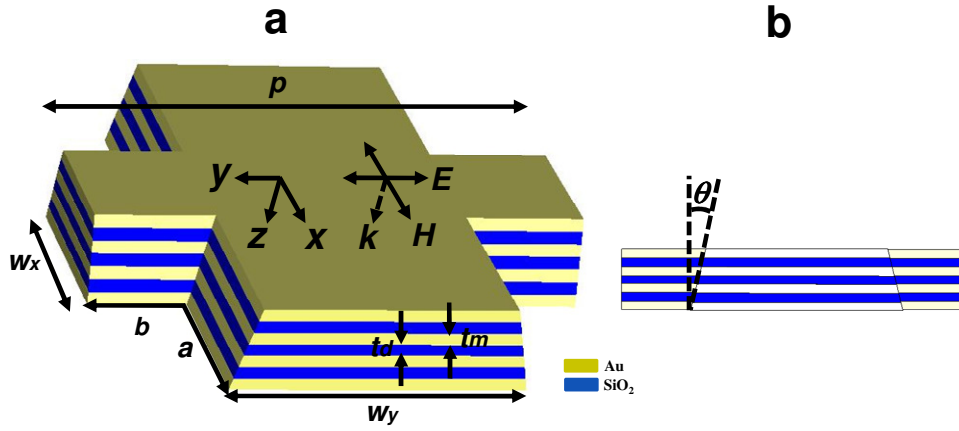


Fig. 4.2 (a) Schematic tilted view of the unit cell for 3 functional layered fishnet NIM with SWA with geometrical parameters, the direction of polarization and propagation. Side view is shown in (b) with SWA.

Pitch ( $p$ )	Rectangular hole size		Length		Thickness ( $t$ )		Constitutive materials	Sidewall-angle ( $\theta$ )
800	Long Side ( $2a$ )	520 ( $0.65 \cdot p$ )	$w_x$	280	Au ( $t_m$ )	20	Au Drude model	$0^\circ - 20^\circ$
	Short Side ( $2b$ )	320 ( $0.4 \cdot p$ )	$w_y$	480	SiO <sub>2</sub> ( $t_d$ )	20	SiO <sub>2</sub> : $n = 1.5$	

Table 4.1 NIM geometrical parameters (all dimensions in nm)

#### 4.2.2 Simulation

We performed simulations of an ideal multi-functional layered fishnet NIM with SWAs using both the commercial 3D FIT solver (CST Microwave Studio, Computer Simulation technology GmbH, Darmstadt, Germany) [25] and a rigorous coupled wave analysis (RCWA) [26,27]. Comparable results were obtained for both techniques; the results shown in this chapter

were obtained by CST. In the CST simulator, a single unit cell was simulated as shown in Fig. 4.2 (a), with appropriate boundary conditions including both the transverse magnetic field ( $H_t$ ) equal to zero (perfect magnetic conductor: PMC) in the  $\hat{y}, \hat{z}$  plane and transverse electric field ( $E_t$ ) equal to zero (perfect electric conductor: PEC) in the  $\hat{x}, \hat{z}$  plane, stimulating a TEM plane wave propagating in the  $\hat{z}$  direction. We find the complex frequency dependent  $S$  parameters  $S_{11}$ ,  $S_{12}$ ,  $S_{21}$  and  $S_{22}$ , where the subscript 1(2) represents the waveguide port at larger (smaller) aperture. The simulated transmission ( $|S_{21}|^2 = |S_{12}|^2$ ), reflectances ( $|S_{11}|^2$ ,  $|S_{22}|^2$ ) and reflection anisotropy ( $|S_{22}|^2 - |S_{11}|^2$ ) are plotted in Fig. 4.3. The direction of polarized incoming light (incident electric field) is parallel to the narrower stripe width ( $w_x$ ) between apertures ( $\hat{y}$  axis) as shown in Fig. 4.2 (a).

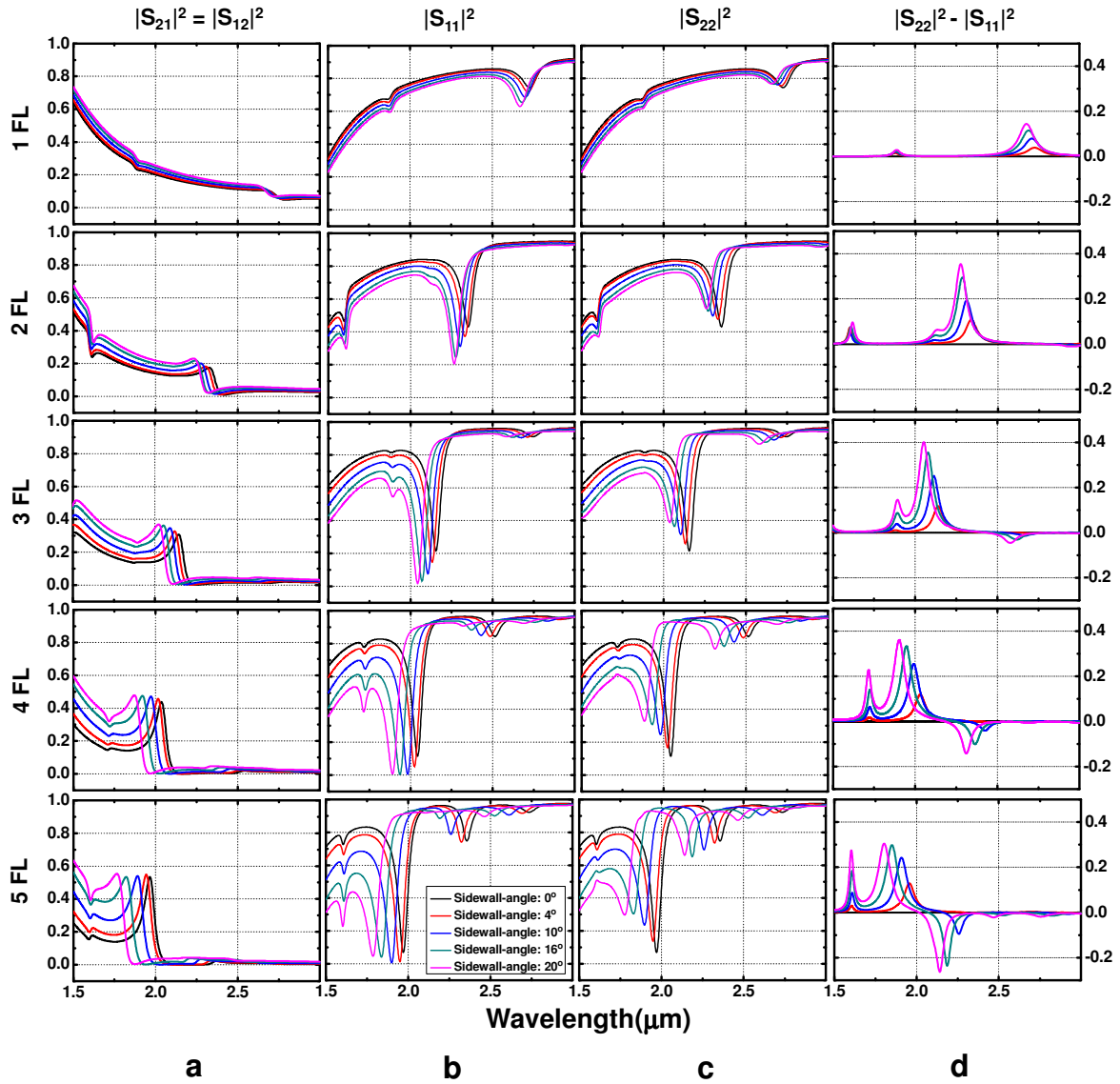


Fig. 4.3  $|S_{ij}|^2$ , where  $i, j = 1, 2$  (i.e. port 1, port 2) for one to up to five functional layered fishnet NIMs with SWAs ( $0^\circ, 4^\circ, 10^\circ, 16^\circ, 20^\circ$ ) as a parameter using the CST simulator. (a) The transmission is independent of propagation direction ( $|S_{21}|^2 = |S_{12}|^2$ ). (b), (c) The reflectances ( $|S_{11}|^2, |S_{22}|^2$ ) depend on the direction of incident wave as a result of the SWA. (d) Reflectivity difference,  $|S_{22}|^2 - |S_{11}|^2$ .

The refractive index of the dielectric material ( $\text{SiO}_2$ ) used as a spacer between Au layers in NIMs taken as  $n_{\text{SiO}_2} = 1.5$  along with a simple Drude model for the Au dielectric function given by Eq. (3.1) in Chapter 3, with  $\omega_p$  (plasma frequency) = 9.02 eV and  $\omega_c$  (collision frequency) = 0.0269 eV [28].

A common method to retrieve the effective constitutive parameters is based on the complex transmission and reflection coefficients ( $S$ -parameters). The standard retrieval method assumes isotropic constitutive parameters ( $\epsilon$ ,  $\mu$ ) for a symmetric structure [20]. However, this fails if the unit cell of the NIM is not symmetric in the propagation direction as a result of the SWAs induced during fabrication. In case of a NIM with SWAs, the  $S$ -parameters, especially  $S_{11}$  and  $S_{22}$  are different depending on the propagation direction of incident light with respect to the unit cell ( $S_{11} \neq S_{22}$ ,  $S_{21} = S_{12}$ ), e.g. the structure exhibits inhomogeneous asymmetry or bianisotropy [21].

The fishnet structured NIMs with SWA as shown in Fig. 4.2 (a) will respond with a bianisotropic property when a TEM plane wave is incident in the  $z$  direction with an electrical field in  $y$  direction and a magnetic field in the  $x$  direction. This is because the electrical field in the  $y$  direction can induce a magnetic dipole in the  $x$  direction due to the structural asymmetry, (i.e. SWA), while the magnetic field in the  $x$  direction can also induce an electrical dipole in the  $y$  direction (for details, see section 4.2.3) . By assuming that the medium is reciprocal [29] and that the harmonic time dependence is  $e^{-i\omega t}$ , we can write the constitutive relationships as

$$\begin{aligned}\bar{D} &= \bar{\epsilon} \cdot \bar{E} + \bar{\xi} \cdot \bar{H} \\ \bar{B} &= \bar{\mu} \cdot \bar{H} + \bar{\zeta} \cdot \bar{E}\end{aligned}\tag{4.1}$$

$$\text{where } \overline{\overline{\epsilon}} = \epsilon_0 \begin{pmatrix} \epsilon_x & 0 & 0 \\ 0 & \epsilon_y & 0 \\ 0 & 0 & \epsilon_z \end{pmatrix}, \overline{\overline{\mu}} = \mu_0 \begin{pmatrix} \mu_x & 0 & 0 \\ 0 & \mu_y & 0 \\ 0 & 0 & \mu_z \end{pmatrix}, \overline{\overline{\xi}} = \frac{1}{c} \begin{pmatrix} 0 & 0 & 0 \\ -i\xi & 0 & 0 \\ 0 & 0 & 0 \end{pmatrix}, \overline{\overline{\zeta}} = \frac{1}{c} \begin{pmatrix} 0 & i\xi & 0 \\ 0 & 0 & 0 \\ 0 & 0 & 0 \end{pmatrix}.$$

Here,  $c$ ,  $\epsilon_0$ ,  $\mu_0$  and  $\xi$  are the speed of light, permittivity and permeability of free space and the material bi-anisotropic parameter. The seven unknowns,  $\epsilon_x$ ,  $\epsilon_y$ ,  $\epsilon_z$ ,  $\mu_x$ ,  $\mu_y$ ,  $\mu_z$ , and  $\xi$  are quantities without dimensions. For the restricted polarization relevant to the experiment measurements as shown in Fig. 4.2 (a), three parameters ( $\epsilon_y$ ,  $\mu_x$ , and  $\xi$ ) will be active, while the other four parameters ( $\epsilon_x$ ,  $\epsilon_z$ ,  $\mu_y$ ,  $\mu_z$ ) will not be involved in the constitutive relations as

$$\begin{pmatrix} D_x \\ D_y \\ D_z \end{pmatrix} = \epsilon_0 \begin{pmatrix} \epsilon_x & 0 & 0 \\ 0 & \epsilon_y & 0 \\ 0 & 0 & \epsilon_z \end{pmatrix} \cdot \begin{pmatrix} 0 \\ E_y \\ 0 \end{pmatrix} + \frac{1}{c} \begin{pmatrix} 0 & 0 & 0 \\ -i\xi & 0 & 0 \\ 0 & 0 & 0 \end{pmatrix} \cdot \begin{pmatrix} H_x \\ 0 \\ 0 \end{pmatrix} \quad (4.2)$$

$$\begin{pmatrix} B_x \\ B_y \\ B_z \end{pmatrix} = \mu_0 \begin{pmatrix} \mu_x & 0 & 0 \\ 0 & \mu_y & 0 \\ 0 & 0 & \mu_z \end{pmatrix} \cdot \begin{pmatrix} H_x \\ 0 \\ 0 \end{pmatrix} + \frac{1}{c} \begin{pmatrix} 0 & i\xi & 0 \\ 0 & 0 & 0 \\ 0 & 0 & 0 \end{pmatrix} \cdot \begin{pmatrix} 0 \\ E_y \\ 0 \end{pmatrix}$$

After matrix multiplication, it can be simplified to a 1D case as

$$\begin{pmatrix} D_y \\ B_x \end{pmatrix} = \begin{pmatrix} \epsilon_0 \epsilon_y & -\frac{i\xi}{c} \\ \frac{i\xi}{c} & \mu_0 \mu_x \end{pmatrix} \cdot \begin{pmatrix} E_y \\ H_x \end{pmatrix} \quad (4.3)$$

In Eq. (4.3), the material bi-anisotropic parameter  $\xi$  (off-diagonal terms in the matrix) describes the excitation of magnetic dipoles by the electric component of the field and vice versa. Moreover, for an electromagnetic wave traveling in the  $z$  direction as shown in Fig. 4.2 (a), the impedances ( $z$ ) will be

$$z^{(2,1)} = \frac{\mu_x}{n + i\xi}, \quad z^{(1,2)} = \frac{\mu_x}{n - i\xi} \quad (4.4)$$

Here,  $z^{(i,j)}$  is the impedance for propagation direction from port  $j$  to port  $i$  and  $n$  is the effective refractive index, which related by  $n^2 = \varepsilon_y \mu_x - \xi^2$ . This result was used previously to interpret experiments on deliberately anisotropic metamaterial structures [19].

### 4.2.3 Analysis

Structures with different SWAs were modeled to investigate the effect of the SWA on the strength and position of the effective parameters – effective refractive index and permeability. From 1- to 5-FLs, the wavelength at the minimum value of  $\text{Re}(\mu_{\text{eff}})$  decreases as the SWA increases as shown in Fig. 4.4 (b) and (d). This tendency can be qualitatively interpreted by the magnetic resonance of an equivalent  $LC$  circuit: a larger SWA corresponds to smaller capacitance and inductance [30], which in turn leads to a shorter resonance wavelength. As shown in Fig. 4.4 (d), the wavelength of the minimum value of  $\text{Re}(\mu_{\text{eff}})$  is linearly dependent on the SWA.

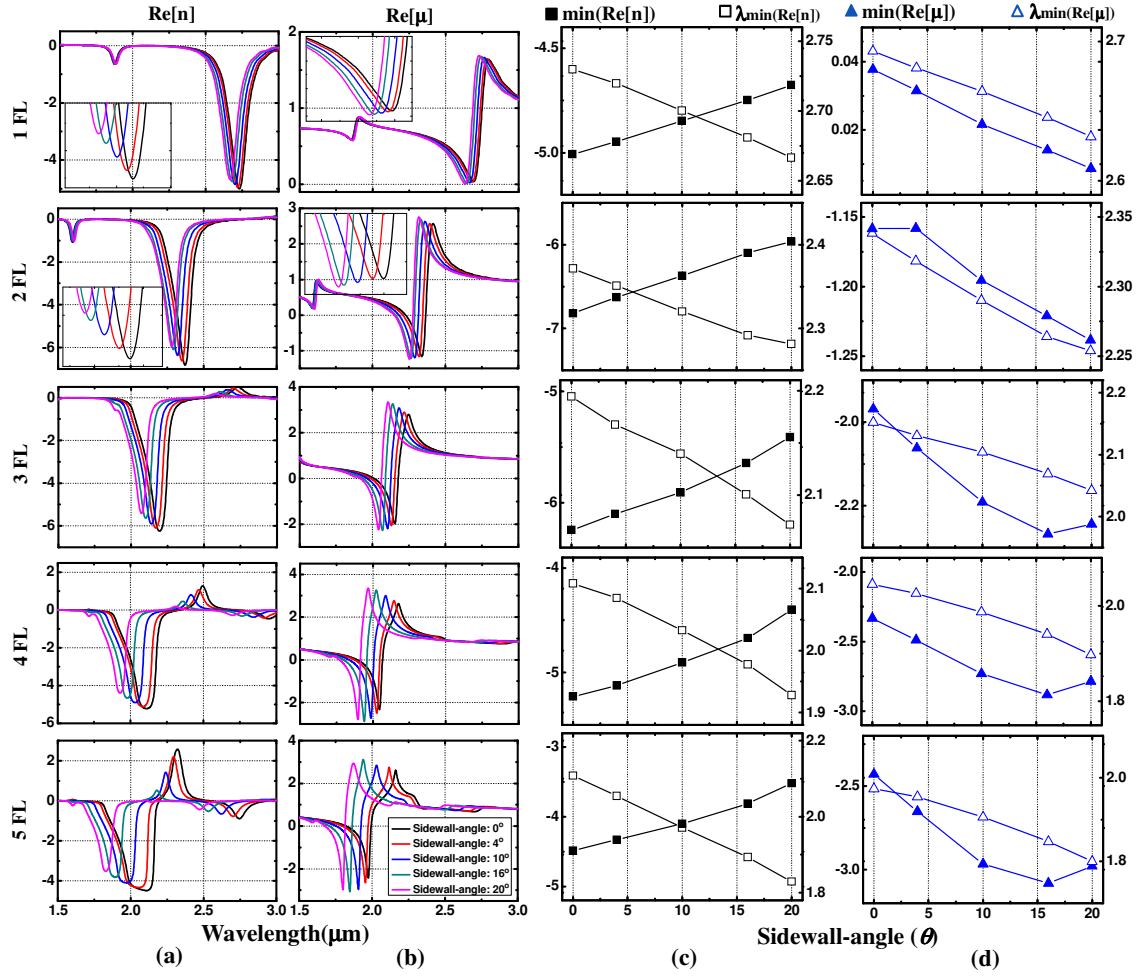


Fig. 4.4 Real parts of the effective parameters ( $n$ ,  $\mu$ ) for one- to five-functional layered fishnet NIMs with SWAs ( $0^\circ$ ,  $4^\circ$ ,  $10^\circ$ ,  $16^\circ$ ,  $20^\circ$ ) using the modified retrieval equation. (a), (b)  $\text{Re}(n_{\text{eff}})$  and  $\text{Re}(\mu_{\text{eff}})$ . (c), (d) Minimum values and the wavelength at minimum values of real parts of  $\text{Re}(n_{\text{eff}})$  and  $\text{Re}(\mu_{\text{eff}})$ . The five rows represent 1 FL up to 5 FLs, respectively.

The trend of a decreasing minimum value of  $\text{Re}(\mu_{\text{eff}})$  can be explained as a more complicated coupling between magnetic and electric dipoles. In an ideal fishnet structured NIM with vertical sidewalls, the bi-anisotropic parameter  $\xi$  for fishnet NIMs with zero SWA is identically zero,



independent of number of FLs. The structure is composed of independent electric atoms and magnetic atoms: the electric response results from the array of thin metal wires parallel to the electric field direction and the magnetic response from pairs of metal stripes separated by a dielectric spacer along the direction of magnetic field that support an anti-symmetric current as shown in Fig. 4.5 (a).

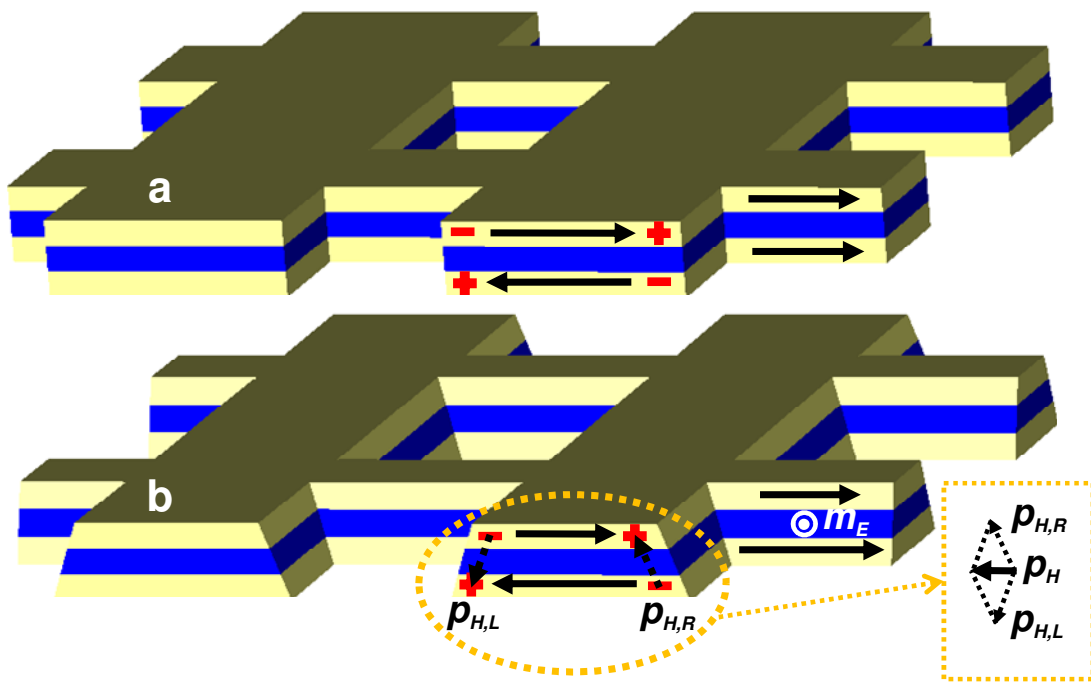


Fig. 4.5 Schematic depicting the electric and magnetic dipoles in an ideal fishnet structure (SWA = 0°) and a realistic fishnet structure with a fabrication-induced SWA (SWA ≠ 0°). (a) Electric/magnetic dipole induced by electric/magnetic field, respectively. (b) Electric dipole response, indicated by the two rightmost arrows, also induces a magnetic dipole ( $m_E$ ) due to the unbalanced current distribution in the two plates. The magnetic dipole response, asymmetric current loop, also induces an electric dipole ( $P_H$ ) in the metamaterial plane given by the vector sum of the two induced polarizations. The same coordinate system as Fig. 4.2 is followed.

However, in realistic fishnet structured NIMs with a fabrication-induced SWA, the NIMs are bi-anisotropic. In the thin metal wires (electric response), a magnetic dipole in the  $\hat{x}$ -direction is induced by an electric field  $\vec{E}$  in the  $\hat{y}$ -direction, resulting from the disparity of the current distribution in the two metal films, so the magnetic and electric dipoles induced by  $\vec{E}$  are coupled to each other. Figure 4.6 shows that the bi-anisotropic parameter  $\xi$  for multiple functional layered fishnet NIMs as a functional of the SWA. Figure 4.7 shows the current density as a specific frequency [at the minimum value of  $\text{Re}(\mu_{\text{eff}})$ ].

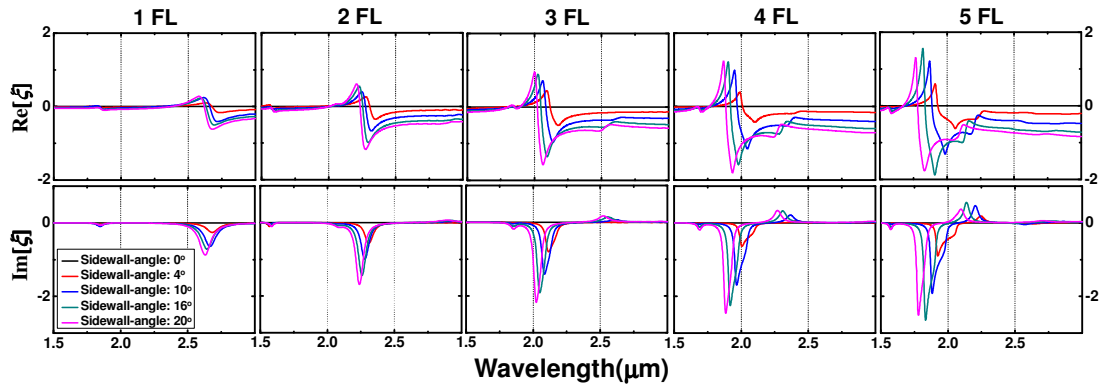


Fig. 4.6 Real and imaginary parts of the bi-anisotropic parameter ( $\xi$ ) for one- up to five-functional layered fishnet NIMs with SWAs ( $0^\circ$ ,  $4^\circ$ ,  $10^\circ$ ,  $16^\circ$ ,  $20^\circ$ ).

From Fig. 4.7 (a) and (c), two and three fishnet structured NIMs with vertical sidewalls have a symmetric current distribution in the upper and lower Au plates, but NIM with SWA ( $20^\circ$ ) show an unbalanced current distribution as shown in Fig. 4.7 (b) and (d). Similarly, the electric dipoles ( $P_H$ ) induced by  $\vec{H}$  (magnetic loop response) now include a net  $\hat{y}$ -component, so the electric and

magnetic dipoles induced by  $\vec{H}$  are also mutually coupled as shown in Fig. 4.5 (b). An equal current distribution is still obtained in ideal NIMs (vertical sidewalls) with 2, 3 FLs as shown in Fig. 4.7 (a) and (c). For this case there are no electric dipole induced by  $\vec{H}$  in the  $\hat{y}$ -direction. However, the SWA effect shown in Fig. 4.7 (b) and (d) results in the asymmetric current distribution resulting from unequal Au plate size. It also induces coupling between electric and magnetic dipoles as shown in Fig. 4.5 (b).

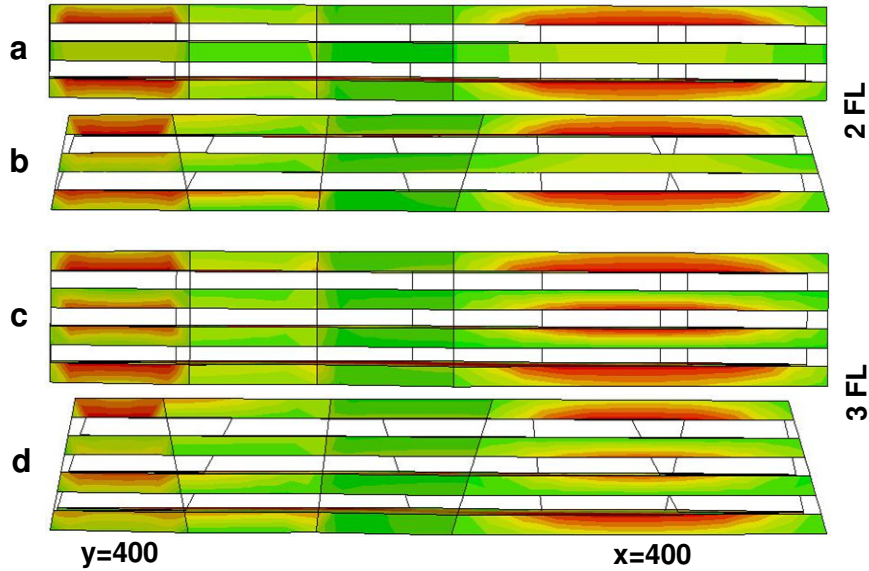


Fig. 4.7  $y$ -component of current density at specific frequency [minimum value of  $\text{Re}(\mu_{\text{eff}})$ ] for 2, 3 FLs with SWA  $0^\circ$ ,  $20^\circ$ . (a), (b) 2 FLs with SWA  $0^\circ$ ,  $20^\circ$ . (c), (d) 3FLs with SWA  $0^\circ$ ,  $20^\circ$ .

Next, it is of interest to study the extracted real part of the effective refractive index depending on the SWA and number of FLs. In Fig. 4.4 (a) and (b), the  $\text{Re}(\mu_{\text{eff}})$  of a single functional layered NIM is positive, but  $\text{Re}(n_{\text{eff}})$  is negative because the real part of the effective permittivity has a large negative value and overall the structure satisfies the necessary condition for negative

refraction ( $\epsilon' \cdot \mu'' + \mu' \cdot \epsilon'' < 0$ ). The magnitude of negative refractive index in NIMs with 1 FL depends on the sidewall-angle, that is, the minimum value of  $\text{Re}(n_{\text{eff}})$  increases as the SWA increases as shown in Fig. 4.4 (a). The reason for the increase is clear: as the SWA increases, the absolute values of  $\text{Re}(\epsilon_{\text{eff}})$  decrease (not shown) due to the decrease of the Au linewidth along the direction of electric field. The wavelength at the minimum of  $\text{Re}(n_{\text{eff}})$  decreases with increase of SWA, which is a result of the blue-shifted resonance peaks of both  $\text{Re}(\mu_{\text{eff}})$  and  $\text{Re}(\epsilon_{\text{eff}})$ . Two- to five-FL fishnet structured NIMs with SWA exhibit negative  $\text{Re}(\mu_{\text{eff}})$  and  $\text{Re}(\epsilon_{\text{eff}})$ , i.e. are double negative materials. Also, the blue-shifted resonance frequency of effective permittivity and permeability as mentioned above accounts for decrease of the wavelength at minimum effective refractive index in multi-functional layered NIMs with the increase of the SWA.

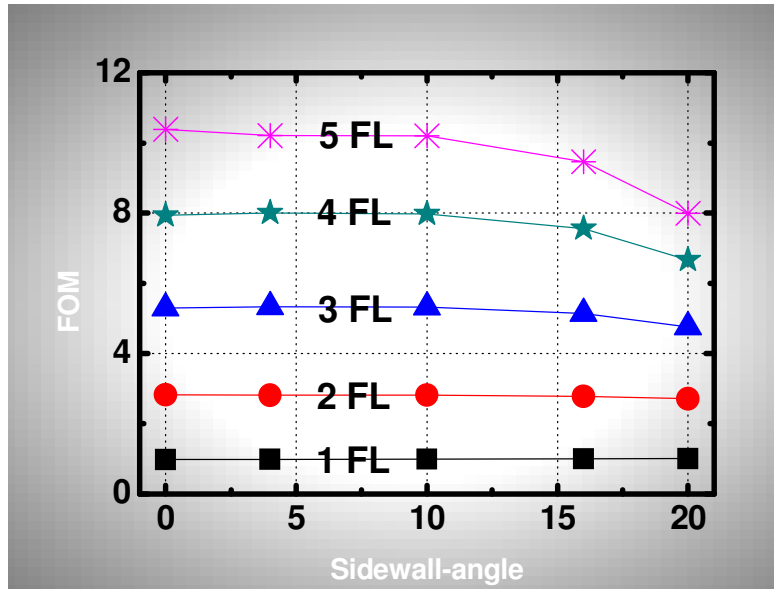


Fig. 4.8 The figure of merit [ $\text{FOM} \equiv -\text{Re}(n)/\text{Im}(n)$ ] of 1- to 5-functional layered NIMs as a function of the SWA.

## 4.3 Experimental Demonstration in Asymmetric medium

### 4.3.1 Design and Dimensions

In first experimental demonstration, we use gold-based NIMs with elliptical holes, similar to those reported previously in a comparison of unit cell geometry (circle, ellipse, and rectangle) [8]. As a result of the SWA, the NIM structure has a vertical ( $z$ -or propagation direction) biasymmetry. The transmission through the structure is identical from either side by reciprocity but the reflectivities are different depending on the incident illumination direction relative to the structural asymmetry. The inhomogeneous asymmetric structure has different  $S_{11}$  [reflectivity from port 1 (top, air)] and  $S_{22}$  [reflectivity from port 2 (bottom, substrate)] in contrast to the symmetric structure for which  $|S_{11}|^2 = |S_{22}|^2$  as described in section 4.2.2.

The structure of all samples discussed in this section consists of a BK7 glass ( $2.5 \times 2.5 \text{ cm}^2$ ) substrate with either one (Au/Al<sub>2</sub>O<sub>3</sub>/Au), two (Au/Al<sub>2</sub>O<sub>3</sub>/Au/Al<sub>2</sub>O<sub>3</sub>/Au), or three (Au/Al<sub>2</sub>O<sub>3</sub>/Au/Al<sub>2</sub>O<sub>3</sub>/Au/Al<sub>2</sub>O<sub>3</sub>/Au) FLs performed with a two-dimensional square array of elliptical holes through the entire structure. Each layer of Au (Al<sub>2</sub>O<sub>3</sub>) is 25 (58) nm thick, respectively. The total thickness of NIMs with one to three FLs was 108, 191, and 274 nm, respectively. Detailed processing steps to fabricate multifunctional layered NIMs with Au/Al<sub>2</sub>O<sub>3</sub> are described in section 4 of Chapter 2.

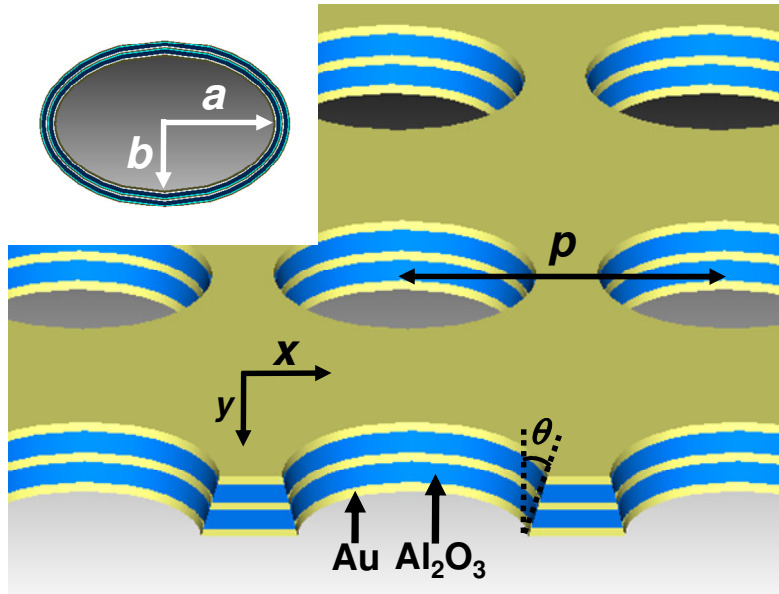


Fig. 4.9 Schematic view of structure and dimensions for two FLs elliptical NIM:  $p = 830$  nm,  $2a = 584$  nm,  $2b = 361$  nm, and  $\theta$  (SWA) =  $13^\circ$ . Inset shows magnified elliptical hole with dimension ( $a$ ,  $b$ ) in major/minor axis.

### 4.3.2 Measurement, Simulation and Analysis

The transmission and reflectance spectra were recorded with a Nicolet FTIR spectrometer with a quartz beam splitter and a DTGS-KBr detector. The transmission measurement was carried out at normal incidence to the samples and was normalized to the transmission through a bare BK7 glass substrate. For reflectance, the input beam is incident on the samples at  $11^\circ$  from the surface normal and normalization is with respect to the reflectivity from an Au mirror. The FTIR beam was polarized along the minor axis of the ellipses as shown in Fig. 4.10.

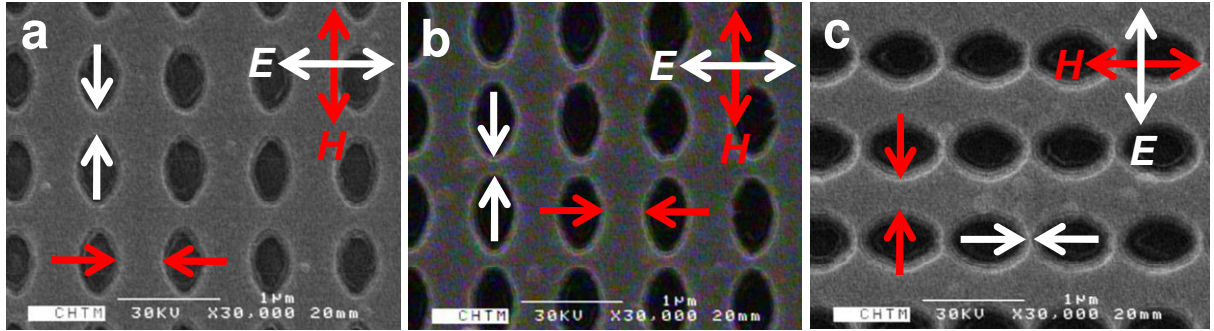


Fig. 4.10 SEM images (top view) of elliptical NIMs with (a) one, (b) two, (c) three FLs. The orientation of polarization is displayed ( $E$  and  $H$  denote electric and magnetic field, respectively). The increase in the ellipse dimensions with additional layers is clear.

Measured transmission and reflectance spectra of elliptical NIMs (eNIMs) with one to three FLs are shown in first column of Fig. 4.11. To simulate the properties of bianisotropy resulting from the fabrication-induced SWA, we used CST Microwave Studio [25] based on a FIT (for details, see section 4.2.2). The optical parameters for constitutive materials were taken as  $n_{\text{substrate}} = 1.5$ ,  $n_{\text{Al}_2\text{O}_3} = 1.62$  and a simple Drude model was used for Au permittivity, with plasma frequency  $\omega_p = 9.02$  eV, scattering frequency  $\omega_c = 0.081$  eV, which is three times larger [28] than that reported for bulk Au to give the best fit between experiment and simulation as shown in Fig. 4.11. In eNIMs with a nonzero SWA, the reflectances depending on the propagation direction of incident beam,  $|S_{11}|^2$  (from air) and  $|S_{22}|^2$  (from substrate), are different in both experiment and simulation as shown in Fig. 4.11.

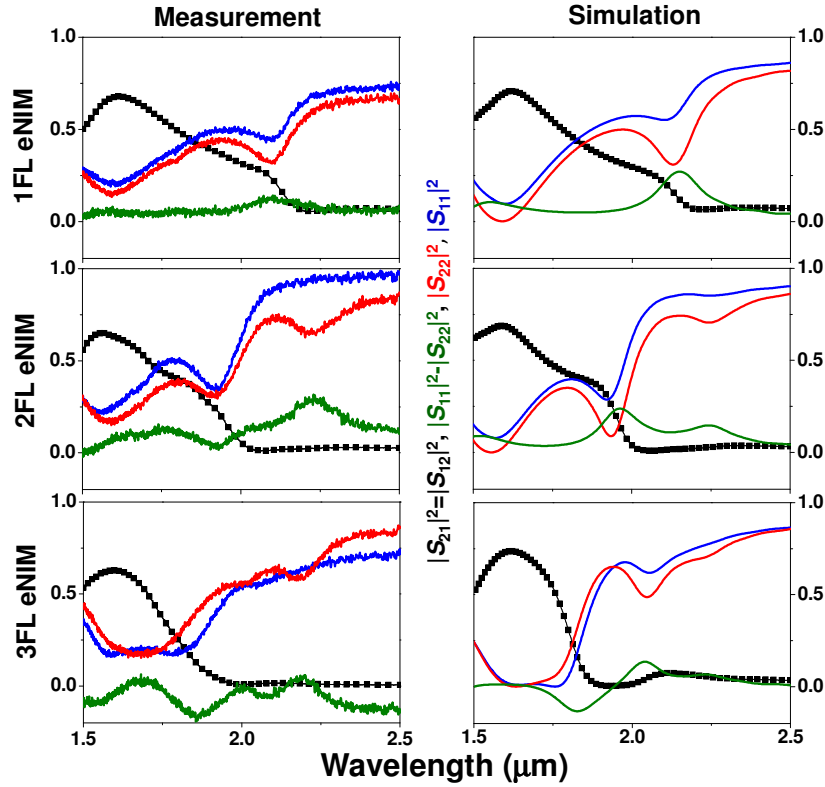


Fig. 4.11 Measured (left) and simulated (right) spectra with the specific polarization direction as shown in Fig. 4.10. The slight blue-shift of the experiment reflectivity resonance is due to the off-normal ( $11^\circ$ ) measurement angle.

Figure 4.12 shows the effective refractive index, permeability and FOM for one to three FLs eNIMs using this modified retrieval equation as explained in section 4.2.2. The eNIM with one FL has a negative  $\text{Re}(n_{\text{eff}})$ , negative  $\text{Re}(\epsilon_{\text{eff}})$  (not shown), positive  $\text{Re}(\mu_{\text{eff}})$ , and a comparatively large  $\text{Im}(\mu_{\text{eff}})$ , which leads to a material with a large loss but nonetheless satisfying the necessary condition for a negative index. The eNIMs with two and three FLs have both  $\text{Re}(\epsilon_{\text{eff}})$  and  $\text{Re}(\mu_{\text{eff}})$  negative, e.g. are double negative materials, and have improved FOMs. eNIMs with vertical sidewalls were modeled for direct comparison of effective parameters (same



as angles used in Fig. 4.11 and Fig. 4.12) [22]. In addition, the trend of  $\text{Re}(n_{\text{eff}})$  and  $\text{Re}(\mu_{\text{eff}})$  in Fig. 4.13 agrees with simulation results shown in Fig. 4.3.

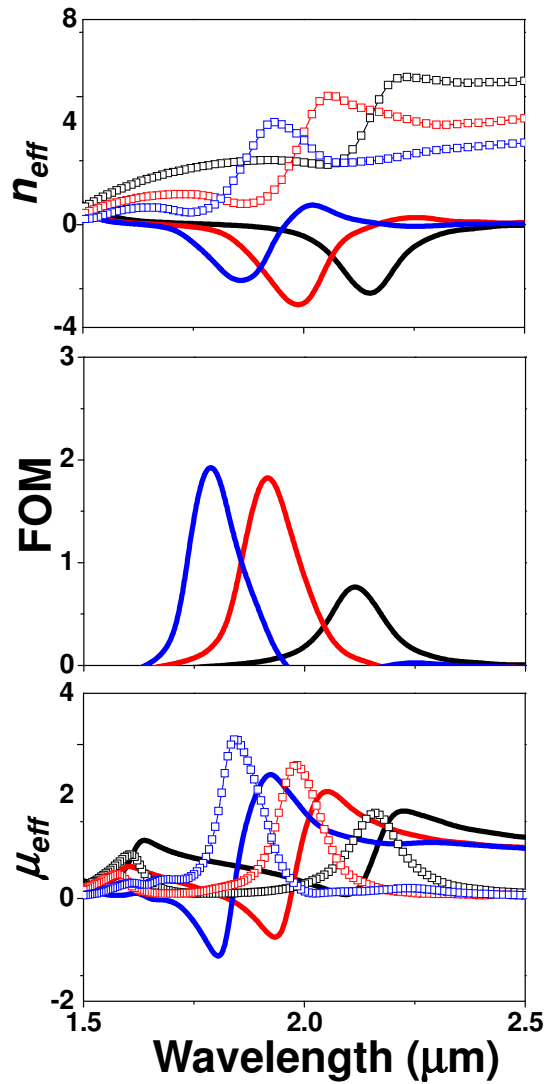


Fig. 4.12 Effective parameters (refractive index, FOM, and permeability) for one to three FLs eNIMs. The color convention is that one FL, two FLs, and three FLs eNIMs are black, red, and blue, respectively. Real (imaginary) part of effective parameters in first and third row is displayed with solid lines (line with unfilled square).

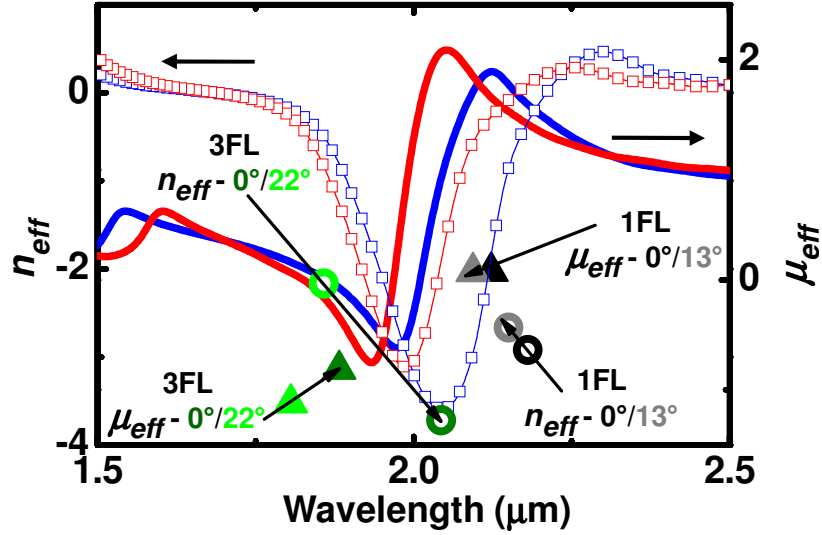


Fig. 4.13  $\text{Re}(n_{\text{eff}})$  (line with unfilled squares) and  $\text{Re}(\mu_{\text{eff}})$  (solid lines) in two FLs eNIMs with SWA  $0^\circ$  (blue) and  $13^\circ$  (red). Solid (open) symbols represent  $\min[\text{Re}(\mu_{\text{eff}})]$  ( $\min[\text{Re}(n_{\text{eff}})]$ ) of one and three FLs eNIMs with/without SWA. Color convention: gray (black): one FL eNIM with (without) SWA and three FL eNIMs light (dark) green: with (without) SWA.

It is worth pointing out that this understanding of nonzero SWA effects requires correction of our previous report [8]. As a result of SWA, a  $\sim 11\%$  improved FOM is retrieved for the NIMs with rectangular apertures.

Because reflectances depending on propagation direction (as shown in first column of Fig. 4.11) were measured in asymmetric medium (air/glass used as superstrate/substrate), additional experiments that fully take into account the bi-anisotropy effect due to fabrication imperfection are needed to confirm these SWA effects with free standing NIMs, i.e. without substrate effect.

## 4.4 Experimental Demonstration in Symmetric medium

### 4.4.1 Design and Dimensions

The structure of all samples investigated here are similar to one as described in section 4.3, except geometrical parameters shown in Fig. 4.14. Detailed fabrication steps for one- to three-functional layered eNIMs are explained in section 4 of Chapter 2.

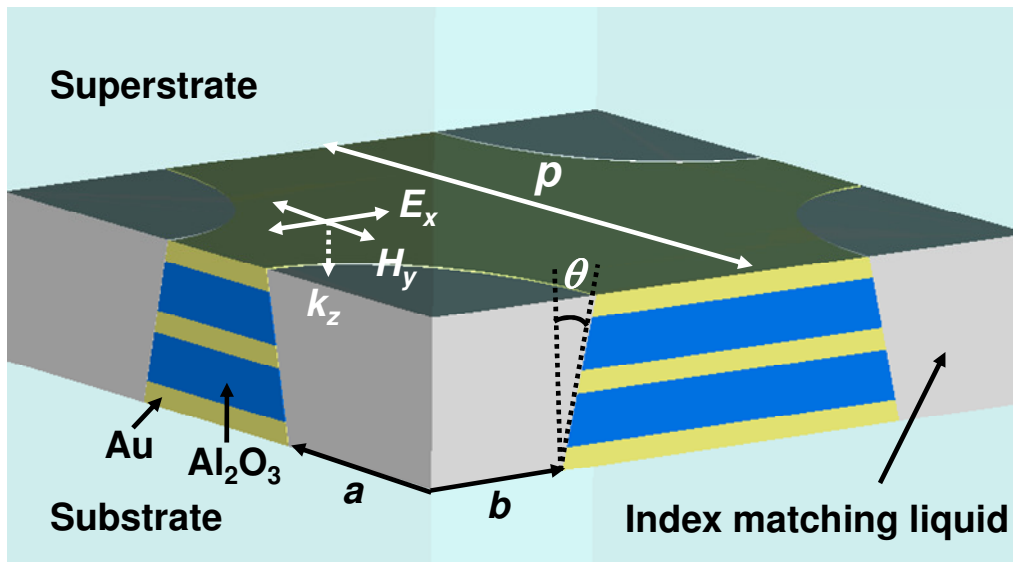


Fig. 4.14 Dimensions of two-functional-layered superstrate-eNIM:  $p = 810$  nm,  $2a = 536$  nm,  $2b = 352$  nm, and  $\theta$  (SWA) =  $13^\circ$ . The polarization direction is described ( $E$ ,  $H$ ,  $k$  denote electric, magnetic field, and propagation direction, respectively).

### 4.4.2 Measurement, Simulation and Analysis

The transmission and reflectance from the superstrate and substrate sides were measured using FTIR as explained in section 4.3.2 with the specific polarization shown in Fig. 4.14. The second and fourth rows of Fig. 4.15 show measured transmission, reflectance and, absorption (1–

T–R) depending on the propagation direction (superstrate to substrate and vice versa) of superstrate-eNIM (s-eNIM) with one to three FLs.

CST Microwave studio was used to obtain the electromagnetic response of one- to three-functional-layered s-eNIMs depending on the propagation direction [25]. The optical parameters for constitutive materials are indicated in section 4.3.2 except  $n_{\text{superstrate}} = n_{\text{index-match liquid}} = 1.5$ . The good agreement between experiment and simulation as shown in Fig. 4.15 gives confidence to investigating the bi-anisotropy effects through effective parameters. Modified retrieval methods [15,18-19,21-24] were used to extract the effective parameters as a result of the broken structural symmetry associated with the nonzero SWA ( $R_{\text{superstrate}} \neq R_{\text{substrate}}$ ).

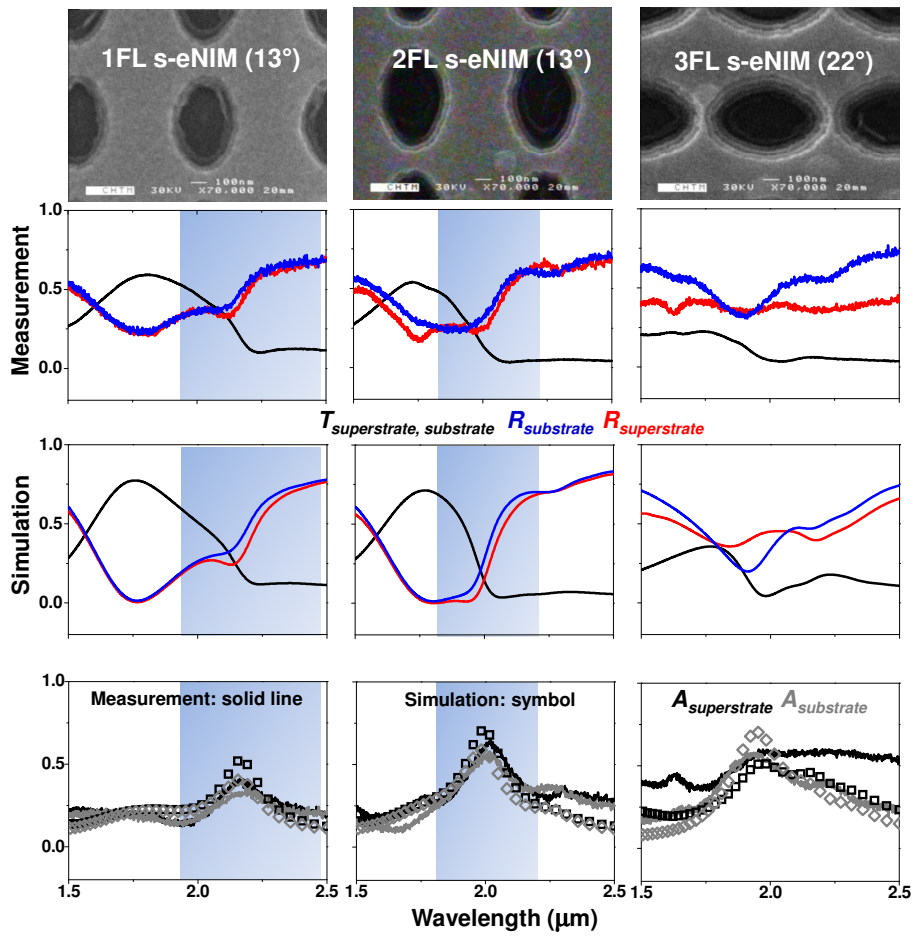


Fig. 4.15 Measured/simulated transmission, reflectance (from superstrate and substrate), and absorption ( $1-T-R$ ) for s-eNIMs, depending on the propagation direction, with the polarization shown in Fig. 4.14. Shaded areas represent wavelength regions of negative refractive index from simulation (see below). First row displays SEM image with one- to three-functional-layered eNIMs (without glass-superstrate and an index-matching fluid).

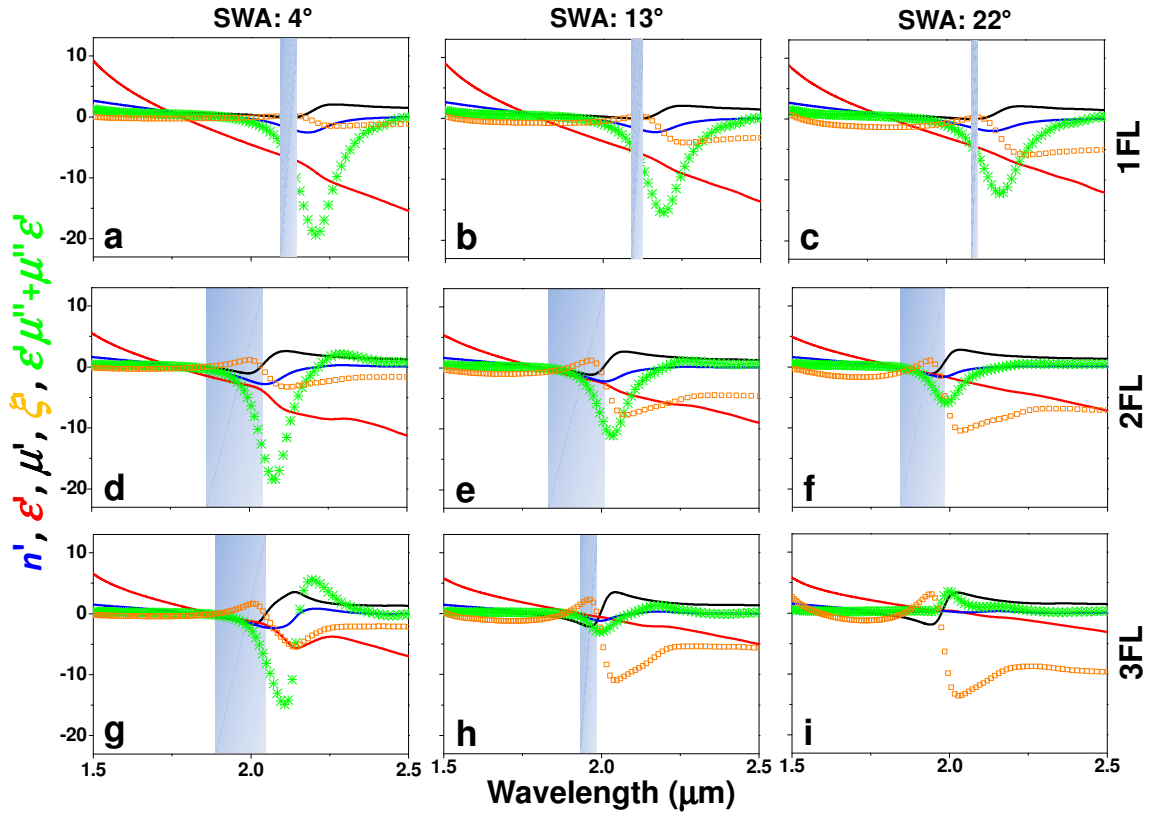


Fig. 4.16  $n', \epsilon', \mu', \xi'$ , necessary condition, and sufficient condition for negative refractive index for one- to three-functional-layered s-eNIMs with SWAs ( $4^\circ, 13^\circ, 22^\circ$ ) are plotted.  $\xi'$  has been multiplied by 10 for clarity.

In Fig. 4.16, we present the real parts of the effective parameters ( $n', \epsilon', \mu'$ ), the real part of the material bianisotropy parameter ( $\xi'$ ), the necessary and sufficient conditions for a negative refractive index for one- to three-functional-layered s-eNIMs with SWAs of  $4^\circ$ ;  $13^\circ$ ; and  $22^\circ$ . By causality ( $n'' > 0$ ), the negative refractive index region ( $n' < 0$ ) is equivalent to the region of  $\epsilon' \cdot \mu'' + \mu' \cdot \epsilon'' < 0$  (for details, see Chapter 1). The bandwidth of the sufficient condition (shaded region) associated with a double-negative material or a negative index with lower loss

becomes narrower as the SWA increases. Specifically, the region of the sufficient condition is limited by the bandwidth of the negative permeability ( $\mu' < 0$ ) in the case of a sidewall-angled one-functional-layered s-eNIM and a two-functional-layered s-eNIM with SWAs ( $4^\circ$  and  $13^\circ$ ), as shown in Fig. 4.16 (a)-(e) and it is influenced by the region of negative permittivity ( $\epsilon' < 0$ ) in the case of a two-functional-layered s-eNIM with SWA ( $22^\circ$ ) and all sidewall-angled three-functional-layered s-eNIMs as shown in Fig. 4.16 (f)-(i).

In general, the double-negative bandwidth depends primarily on the bandwidth of the resonant negative permeability; however, s-eNIMs with both two and three FLs and larger SWAs as shown in Fig. 4.16 (f)-(h) are impacted by the vertical shift of the negative effective permittivity due to a shifted effective plasma frequency ( $\omega_p$ ). In Fig. 4.16 (i), a  $22^\circ$  sidewall-angled three-functional-layered s-eNIM has no region of double negative material because the regions of negative permeability and permittivity no longer overlap. The necessary condition is also not satisfied, so the region of negative index is completely eliminated by the effects of the SWA. In Fig. 4.16, it is obvious that effective plasma frequency ( $\omega_p$ ) tends to decrease as the sidewall angle increases because it is related to the fraction of space occupied by the metal plates [31]. Also, the antiresonant peak of the effective permittivity becomes weaker as the SWA increases because the electric response becomes weaker, which is a consequence of the unequal size of the metal plates.

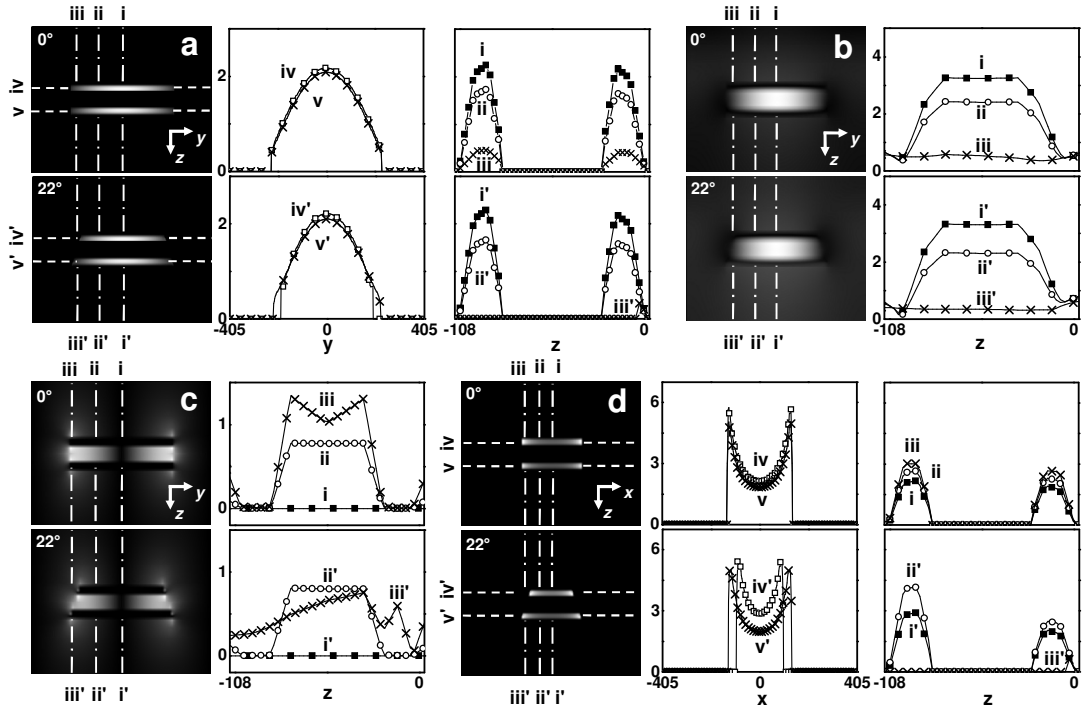


Fig. 4.17 (a) Magnitude of  $y$  component of current density ( $|J_y|$ ); (b)  $x$  component of magnetic field ( $|H_x|$ ); and (c)  $z$  component of electric field ( $|E_z|$ ) at a frequency of  $\min[\text{Re}(\mu_{\text{eff}})]$  for one-functional-layered s-eNIM with SWAs ( $0^\circ$ ,  $22^\circ$ ) are plotted along lines at the edge of cut-wire structure ( $x = 405$  nm). (d)  $|J_y|$  along the lines in edge of thin-metal wire structure ( $y = 405$  nm). The values of  $|J_y|$ ,  $|H_x|$  and  $|E_z|$  have been divided by  $10^{12}$  [A/m<sup>2</sup>],  $10^5$  [A/m], and  $10^8$  [V/m], respectively.



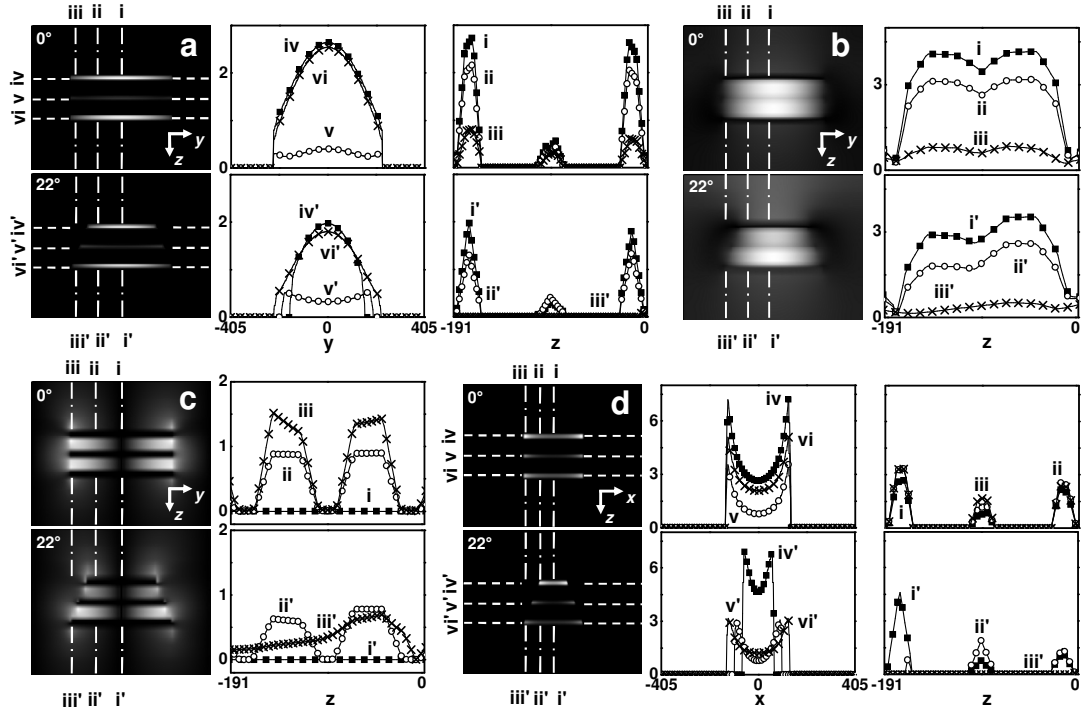


Fig. 4.18 (a) Magnitude of  $y$  component of current density ( $|J_y|$ ); (b)  $x$  component of magnetic field ( $|H_x|$ ); and (c)  $z$  component of electric field ( $|E_x|$ ) at a frequency of  $\min[\text{Re}(\mu_{\text{eff}})]$  for two-functional-layered s-eNIM with SWAs ( $0^\circ$ ,  $22^\circ$ ) are plotted along lines at the edge of cut-wire structure ( $x = 405$  nm). (d)  $|J_y|$  along the lines in edge of thin-metal wire structure ( $y = 405$  nm). The values of  $|J_y|$ ,  $|H_x|$  and  $|E_x|$  have been divided by  $10^{12}$  [A/m<sup>2</sup>],  $10^5$  [A/m], and  $10^8$  [V/m], respectively.

The antiresonant behavior of the real part of  $\xi$  becomes stronger with an increase of the SWA. At the magnetic resonance for a zero sidewall-angled (ideal) cut-wire structure, the magnetic field induces an antisymmetric current loop as shown in Fig. 4.17 (a) and Fig. 4.18 (a), producing a  $\vec{B}$  field confined mainly between the metal plates as shown in Fig. 4.17 (b) and Fig. 4.18 (b). Figure 4.17 (c) and Fig. 4.18 (c) show that the electric field, resulting from accumulated charges

at the edges of each metal plate induced by the antisymmetric currents, is expected to be antisymmetric with respect to the  $y = 0$  plane, to be symmetric with respect to the  $xy$ -plane through middle of the structure, and to be confined between and near the ends of the metal plates. In a zero SWA thin-metal wire structures at electric resonance, the induced currents in the upper and lower metal plates generated by  $\vec{E}$  are parallel, so the oppositely directed induced magnetic field lines go around the metal plates and cancel within the space between the metal plates, as shown in Fig. 4.17 (d) and Fig. 4.18 (d). On the other hand, for nonzero SWA, cut-wire, and thin-metal wire structures, the larger the size disparity (increase of SWA), the stronger the net electric dipole response in the cut-wire structure and the magnetic dipole response induced by asymmetric currents in the thin-metal wires. The reason is that for the nonzero sidewall-angled cut-wire part, the magnitude of the vector summation of electric dipoles tends to be larger as the fabrication-induced SWA increases, resulting from unbalanced current density distribution induced by  $\vec{H}$ . In other words, there is no longer an antisymmetric current density with respect to the  $xy$  plane through the middle of the structure, as shown in Fig. 4.17 (a) and Fig. 4.18 (a). This also results in an asymmetric electric field with respect to the  $xy$  plane through the middle of the structure because of the accumulated charge distribution at each metal plate, as shown in Fig. 4.17 (c) and Fig. 4.18 (c). For the nonzero sidewall-angled thin-metal wires part, the magnitude of the induced magnetic dipole moment between the metal plates tends to be stronger owing to a larger differential strength of induced currents by  $\vec{E}$  in the upper and lower metal plates, as shown in Fig. 4.17 (d) and Fig. 4.18 (d). Notice that in addition to the dependence on the SWA, the antiresonant behavior of  $\text{Re}(\xi)$  with the same sidewall angle as shown in Fig. 4.16 also becomes stronger as the number of FLs increases [22].

## **4.5 Summary**

In summary, we have numerically and experimentally demonstrated the influence of a fabrication-induced SWA in multifunctional layered NIMs based on a fishnet structure. For application, NIMs should be improved through minimization of the structural asymmetry to achieve the double-negative material or multifunctional layered structures, especially at optical frequencies due to the high aspect ratios (height/width) required (the proposed fabrication procedure was reported in [32]).

## 4.5 References

1. D. R. Smith, W. J. Padilla, D. C. Vier, S. C. Nemat-Nasser, and S. Schultz, "Composite medium with simultaneously negative permeability and permittivity," *Phys. Rev. Lett.* **84**, 4184-4187 (2000).
2. R. A. Shelby, D. R. Smith, and S. Schultz, "Experimental verification of a negative index of refraction," *Science* **292**, 77-79 (2002).
3. V. G. Veselago, "The electrodynamics of substances with simultaneously negative values of  $\epsilon$  and  $\mu$ ," *Sov. Phys. Usp.* **10**, 509-514 (1968).
4. J. B. Pendry, "Negative refraction makes a perfect lens," *Phys. Rev. Lett.* **85**, 3966-3969 (2000).
5. S. Zhang, W. Fan, N. C. Panoiu, K. J. Malloy, R. M. Osgood, and S. R. J. Brueck, "Experimental demonstration of near-infrared negative-index metamaterials," *Phys. Rev. Lett.* **95**, 137404 (2005).
6. S. Zhang, W. Fan, N. C. Panoiu, K. J. Malloy, R. M. Osgood, and S. R. J. Brueck, "Optical negative-index bulk metamaterials consisting of 2D perforated metal-dielectric stacks," *Opt. Express* **14**, 6778-6787 (2006).
7. S. Zhang, W. Fan, K. J. Malloy, S. R. J. Brueck, N.-C. Panoiu, and R. M. Osgood, "Near-infrared double negative metamaterials," *Opt. Express* **13**, 4922-4930 (2005).
8. Z. Ku and S. R. J. Brueck, "Comparison of negative refractive index materials with circular, elliptical and rectangular holes," *Opt. Express* **15**, 4515-4522 (2007).
9. G. Dolling, M. Wegener, and S. Linden, "Negative-index metamaterial at 780 nm wavelength," *Opt. Lett.* **32**, 53-55 (2007).
10. S. R. J. Brueck, "Optical and Interferometric Lithography – Nanotechnology Enablers," *Proc. IEEE* **93**, 1704- 1721 (2005).
11. V. M. Shalaev, W. Cai, U. K. Chettiar, H.-K. Yuan, A. K. Sarychev, V. P. Drachev, and A. V. Kildishev, "Negative index of refraction in optical metamaterials," *Opt. Lett.* **30**, 3356-3358 (2005),
12. J. Valentine, S. Zhang, T. Zentgraf, E. Ulin-Avila, D. A. Genov, G. Bartal, and X. Zhang, "Three-Dimensional Optical Metamaterial with a Negative Refractive Index," *Nature* **455**, 376-379 (2008).

13. W. Wu, E. Kim, E. Ponizovskaya, Y. Liu, Z. Yu, N. Fang, Y. R. Shen, A. M. Bratkovsky, W. Tong, C. Sun, X. Zhang, S. Y. Wang, and R. S. Williams, "Optical metamaterials at near and mid-IR range fabricated by nanoimprint lithography", *Appl. Phys. A*, **87**, 143-150 (2007).
14. N. Liu, L. Fu, S. Kaiser, H. Schweizer, and H. Giessen, "Plasmonic building blocks for magnetic molecules in threedimensional optical metamaterials," *Adv. Mater.* **20**, 3859–3865 (2008).
15. Z. Ku and S. R. J. Brueck, "Experimental demonstration of sidewall-angle-induced bianisotropy in multiple-layer negative-index metamaterials," *Appl. Phys. Lett.* **94**, 153107 (2009).
16. G. Doling, M. Wegener, and S. Linden, "Realization of three-functional-layer negative-index photonic metamaterial," *Opt. Lett.* **32**, 551-553 (2007).
17. E. Kim, Y. R. Shen, W. Wu, E. Ponizovskaya, Z. Yu, A. M. Bratkovsky, S. Y. Wang, and R. S. Williams, "Modulation of negative index metamaterials in the near-IR range," *Appl. Phys. Lett.* **91**, 173105 (2007).
18. X. Chen, B-I. Wu, J. A. Kong, and T. M. Grzegorzcyk, "Retrieval of the effective constitutive parameters of bianisotropic metamaterials," *Phys. Rev. E* **71**, 046610 (2005).
19. M. S. Rill, C. Plet, M. Thiel, I. Staude, G. von Freymann, S. Linden, and M. Wegener, "Photonic metamaterials by direct laser writing and silver chemical vapour deposition," *Nat. Mater.* **7**, 543-546 (2008).
20. D. R. Smith, S. Schultz, P. Marko's, and C. M. Soukoulis, "Determination of effective permittivity and permeability of metamaterials from reflection and transmission coefficients," *Phys. Rev. B* **65**, 195104 (2002).
21. D. R. Smith, D. C. Vier, Th. Koschny, and C. M. Soukoulis, "Electromagnetic parameter retrieval from inhomogeneous metamaterials," *Phys. Rev. E* **71**, 036617 (2005).
22. Z. Ku, J. Zhang, and S. R. J. Brueck, "Bi-anisotropy of multiple-layer fishnet negative-index metamaterials due to angled sidewalls," *Opt. Express* **17**, 6782–6789 (2009).
23. M. S. Rill, C. E. Kriegler, M. Thiel, G. von Freymann, S. Linden, and M. Wegener, "Negative-index bianisotropic photonic metamaterial fabricated by direct laser writing and silver shadow evaporation," *Opt. Lett.* **34**, 19–21 (2009).
24. Z. Li, K. Aydin, and E. Ozbay, "Determination of the effective constitutive parameters of bianisotropic metamaterials from reflection and transmission coefficients," *Phys. Rev. E* **79**, 26610 (2009).
25. CST Studio Suite 2006B, <[www.cst.com](http://www.cst.com)>.

26. M. G. Moharam and T. K. Gaylord, "Rigorous coupled-wave analysis of planar-grating diffraction," *J. Opt. Soc. Am.* **71**, 811-818 (1981).
27. B. K. Minhas, W. Fan, K. Agi, S. R. J. Brueck, and K. J. Malloy, "Metallic inductive and capacitive grids: theory and experiment," *J. Opt. Soc. Am. A* **19**, 1352-1359 (2002).
28. M. A. Ordal, L. L. Long, R. J. Bell, S. E. Bell, R. R. Bell, R. W. Alexander, and C. A. Ward, "Optical properties of the metals Al, Co, Cu, Au, Fe, Pb, Ni, Pd, Pt, Ag, Ti and W in the infrared and far infrared," *Appl. Opt.* **22**, 1099-1120 (1983).
29. J. A. Kong, *Electromagnetic Wave Theory*. EMW, Cambridge, MA, 2008.
30. J. Zhou, T. Koschny, and C. M. Soukoulis, "An efficient way to reduce losses of left-handed metamaterials," *Opt. Express* **16**, 11147-11152 (2008).
31. J. B. Pendry, A. J. Holden, W. J. Stewart, and I. Youngs, "Extremely low-frequency plasmons in metallic mesostructures," *Phys. Rev. Lett.* **76**, 4773-4776 (1996).
32. A. Boltasseva and V. M. Shalaev, "Fabrication of optical negative-index metamaterials: recent advances and outlook," *Metamaterials* **2**, 1-17 (2008).

# Chapter 5 All-Optical Switching device using a Negative- Index Metamaterial

## 5.1 Introduction

Development of all-optical signal processing, eliminating the performance and cost penalties of optical-electrical-optical conversion, is important for continuing advances in terabits/second (Tb/s) communications [1]. Because of generally weak ( $[\chi^{(2)}]^2$  or  $\chi^{(3)}$ ) optical nonlinearities, all-optical Kerr-effect and three/four-wave mixing modulators require macroscopic propagation lengths, from centimeters in the case of periodically poled LiNbO<sub>3</sub> (PPLN) [2] to kilometers for fiber-based approaches [1]. Semiconductor optical amplifiers (SOA) offer larger nonlinearities, but these active devices add optical noise and require significant additional area for carrier injection and heat dissipation [1]. High-Q crystalline semiconductor structures, modulated by optical carrier injection, are inherently slow as a result of long carrier lifetimes, although progress is being made in sweeping carriers out of the active region [3-5]. Recently, all-optical modulators using nanoplasmonic waveguides have been proposed, where strong optical field enhancements due to confinement result in smaller devices and larger modulation depths [6]. On the other hand, devices utilizing surface plasmon polaritons have demonstrated sub-picosecond (ps) modulation time-scales but with low modulation depths ( $\Delta T/T \sim 10\%$ ) in micrometer-scale devices [7,8]. In contrast, here we use a metamaterial device to demonstrate sub-picosecond all-optical switching in the near-infrared region in nano-sized devices.

Metamaterials are a new class of nanostructured materials that offer novel optical properties such as a negative index of refraction and new capabilities for optical-optical interactions. To date, much effort has been devoted to the fabrication of these materials, the characterization of their linear optical properties, and the extension of their wavelength range to the near-infrared and visible [9]. However, only limited results have been presented on the modulation of these properties in the terahertz ( $\sim 20$  ps response) [10,11] and near-infrared ( $\sim 60$  ps response) [12] spectral regions. In these reports, as in this work, the metamaterial includes a subwavelength *LC* resonance tank circuit with metal and semiconductor components to provide the negative permeability. Here, we use optical carrier injection to modify the conductivity of the semiconductor and dynamically affect the resonance behavior. With  $\sim 60$  fs pulses and  $\sim 3$  nJ of pump pulse energy absorbed across the  $\sim 700 \mu\text{m}^2$  probe beam area, we photoexcite large peak carrier densities in the amorphous silicon layer of a silver/amorphous silicon/silver (Ag/ $\alpha$ -Si/Ag) fishnet structure. These large carrier densities lead to a regime of sub-picosecond carrier dynamics [13-15]. Thereby, we achieve a transmission modulation ( $\Delta T/T$ ) of up to  $\sim 20\%$  (experimentally limited) in section 5.2 and of up to  $\sim 70\%$  in section 5.3 with an ultrafast response time of  $\sim 600$  fs in a pump-probe experiment. Qualitative agreement with simulations using a finite integration technique (FIT) is obtained. The sub-picosecond pump-probe response has the potential for all-optical Tb/s communication, while the nanometer-scale thickness results in a compact device easily integrated with other photonic devices and applications. Further we demonstrate a dual band of negative index resonance in this device associated with periodic nanostructure coupling to the gap surface plasmon polaritons (gap-SPPs) between the two metal films. . For the present structures, these resonances are at  $\sim 1.13$ ,  $\sim 1.68 \mu\text{m}$  ( $\sim 1.06$ ,  $\sim 1.58 \mu\text{m}$ ) in



section 5.2 (section 5.3), respectively. By scaling metamaterial dimensions, one can tune the negative index resonances, and thus the device response, over the near-infrared spectrum leading to a nanometer-scale, near-infrared tunable, sub-picosecond photonic device.

## 5.2 First Experimental Demonstration

### 5.2.1 Design and Dimensions

The metamaterial structure (Fig. 5.1) is composed of two 28 nm thick Ag films separated by a 60 nm thick  $\alpha$ -Si film for a total thickness of 116 nm. A two-dimensional square periodic array of elliptical holes penetrates all three layers, providing an elliptical negative-index metamaterial (eNIM), where the “elliptical” refers to the structure geometry [16]. The detailed fabrication steps are described in section 5 of Chapter 2.

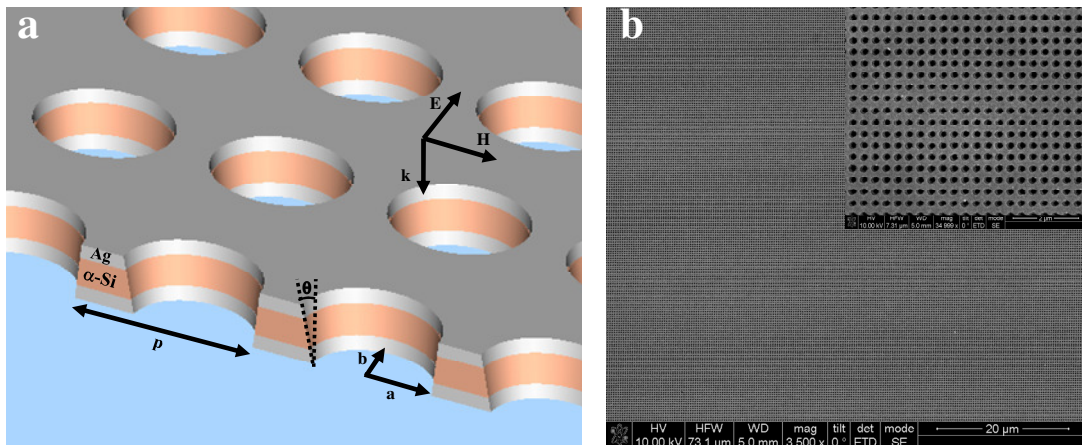


Fig. 5.1 Diagram and SEM image of fabricated elliptical negative-index metamaterial. (a) Geometry and dimensions of elliptical negative-index metamaterial,  $p = 340$  nm;  $2a = 227$  nm;  $2b = 164$  nm; and  $\theta$  (sidewall-angle) =  $8^\circ$ . The structure is constituted of three layers, 28 nm

thick Ag; 60 nm thick  $\alpha$ -Si; and 28 nm thick Ag. In addition, the configuration of polarization and polarization propagation is depicted ( $E$ ,  $H$  and  $k$  denote electric field, magnetic field, and wave vector, respectively) and is denoted by  $E_{\parallel}$  with the perpendicular polarization denoted by  $E_{\perp}$ . (b) Top view SEM image of three-layered eNIM.

## 5.2.2 Measurement and Simulation

Figure 5.2 shows the measured transmission of this structure along with the modeled transmission (CST Microwave Studio [17]) and the effective refractive index for light polarized with the  $E$ -field parallel to the minor axis of the holes (Fig. 5.1) and the propagation direction ( $k$ ) is across the film thicknesses. We denote this polarization by  $E_{\parallel}$  and the perpendicular polarization by  $E_{\perp}$ . The longer wavelength negative index resonance, previously reported in similar structure [18], is at  $\sim 1.68 \mu\text{m}$ . There is a second, shorter wavelength negative index resonance at  $\sim 1.13 \mu\text{m}$ . The wavelength ratio of the two resonances,  $\sim \sqrt{2}$ , suggests that the long wavelength resonance is associated with the periodicity of the holes ( $p = 340 \text{ nm}$ ) while the shorter one is associated with the periodicity along the diagonals ( $\sim \frac{p}{\sqrt{2}} \sim 240 \text{ nm}$ ). This identification is confirmed by the FIT modeling. Figure 5.3 shows the simulated magnetic field strength at the two resonances with the periodicities indicated. As an aside this result suggests that the fishnet structure is not a “true” metamaterial in the sense that the resonances are not independent of the periodicity. This is consistent with the observation that the negative permeability is associated with periodic nanostructure coupling to the gap-mode surface plasma wave between the two metal films [19].

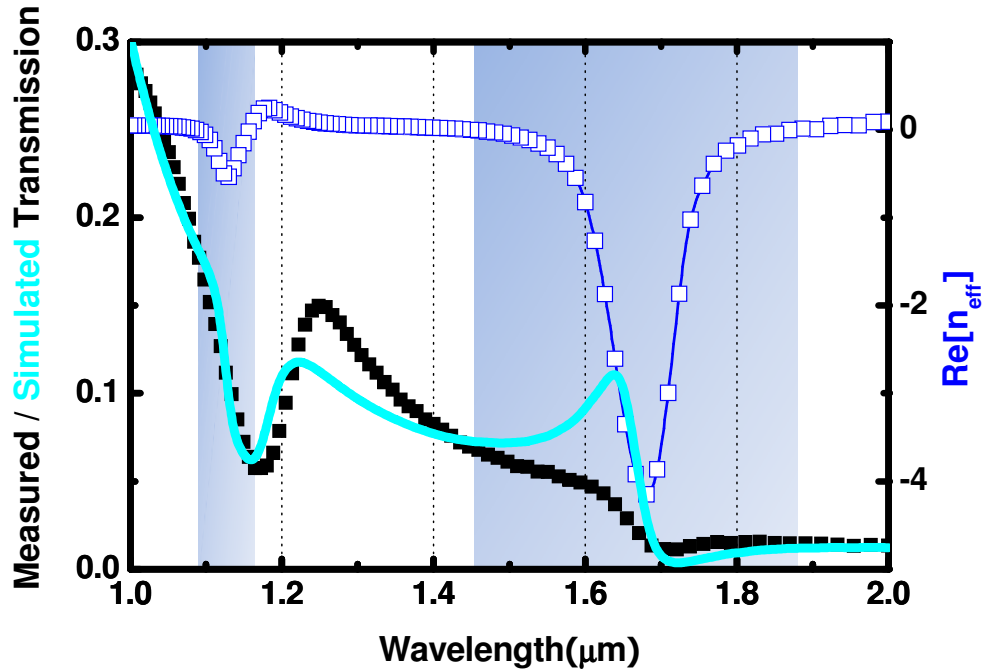


Fig. 5.2 Experimental normal incidence transmission spectrum (FTIR) with polarization direction indicated in Fig. 5.1. The simulated transmission curve is obtained with CST Microwave Studio, which gives a good fit to the measured transmission using 2.5 times the scattering frequency of bulk Ag [20]. The shaded areas represent wavelength regions of negative index as shown (FIT simulation). The simulation is optimized for the region around 1.13  $\mu\text{m}$  where the nonlinear pump-probe measurements are made.

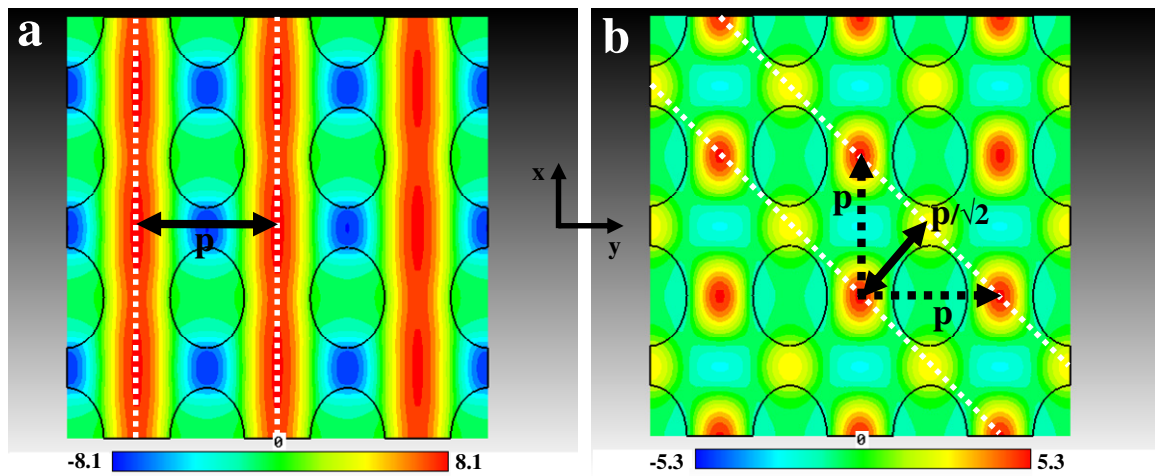


Fig. 5.3 The simulated magnetic field ( $H_x$ ) distribution for eNIM in the  $x, y$  plane through the middle of the structure at the corresponding resonances. (a) Longer wavelength at 1.68  $\mu\text{m}$ . (b) Shorter wavelength at 1.13  $\mu\text{m}$ .

Ultrafast modulation of the eNIM optical properties was studied using a sub-100 fs, visible pump pulse to photoexcite carriers above the  $\alpha$ -Si bandgap ( $\sim 731$  nm), and the time resolved change in transmission was measured with a near infrared probe pulse. The visible pump and near infrared probe pulses were obtained by using a 100 kHz, sub-60 fs, 800 nm regenerative amplifier to simultaneously seed visible and near infrared optical parametric amplifiers (OPA). The pump beam was focused to a spot of  $\sim 80$   $\mu\text{m}$  diameter with a maximum energy of  $\sim 70$  nJ per pulse (i.e., fluence of  $\sim 1.35$   $\text{mJ}/\text{cm}^2$ ). The probe beam was focused to a much smaller  $\sim 30$   $\mu\text{m}$  diameter spot to sample only the area uniformly photoexcited by the pump beam. The central  $\sim 700$   $\mu\text{m}^2$  spot absorbs only  $\sim 3$  nJ/pulse of pump energy with 60% reflection and 10% transmission. By further focusing of the pump and probe spots, the pump energy required for modulating the probe beam can be scaled into the pJ/bit regime as will be discussed

later. Further details of the experimental setup have been presented elsewhere [21]. The pump-induced percentage change in transmission ( $\Delta T/T$ ), that is, the switching ratio, is measured as a function of pump-probe ( $\Delta t$ ), pump fluence, pump wavelength, probe wavelength (1.0 – 1.5  $\mu\text{m}$ ), and probe polarization. The incident pump fluence at the sample was experimentally limited to 1.35  $\text{mJ}/\text{cm}^2$  (for 450 to 700 nm) and 3.9  $\text{mJ}/\text{cm}^2$  at 400 nm.

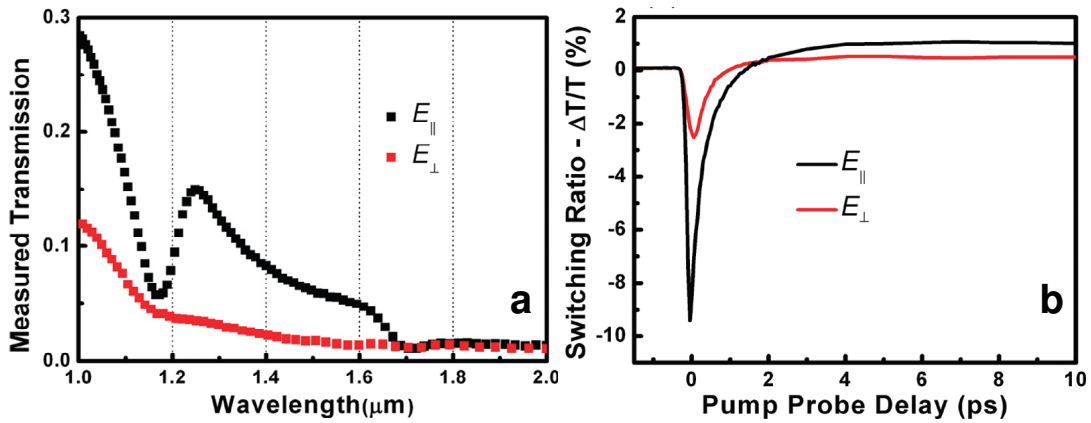


Fig. 5.4 Comparison of device response for different probe polarization. (a) The FTIR transmission shows strong dips (characteristic of the strong negative index resonance; see Fig. 5.2) only for the case  $E_{\parallel}$  (see Fig. 5.1). (b) Correspondingly, we see a weaker nonlinear response, that is, smaller switching ratio, for the polarization  $E_{\perp}$ . (pump/probe wavelength 550/1090 nm).

Because of the elliptical geometry of the holes in the metamaterial, the response of the metamaterial at normal incidence is different for the two polarizations. In particular, we see strong negative index resonances at  $\sim 1.13 \mu\text{m}$  and  $\sim 1.68 \mu\text{m}$  only for the polarization  $E_{\parallel}$  (see Fig. 5.1). Figure 5.4 (a) shows the experimentally measured normal incident transmission (FTIR) through the metamaterial for both polarizations. For the  $E_{\perp}$  geometry, the negative index region

is shifted and much weaker so that the dips in transmission associated with this region (Fig. 5.2) are significantly smaller.

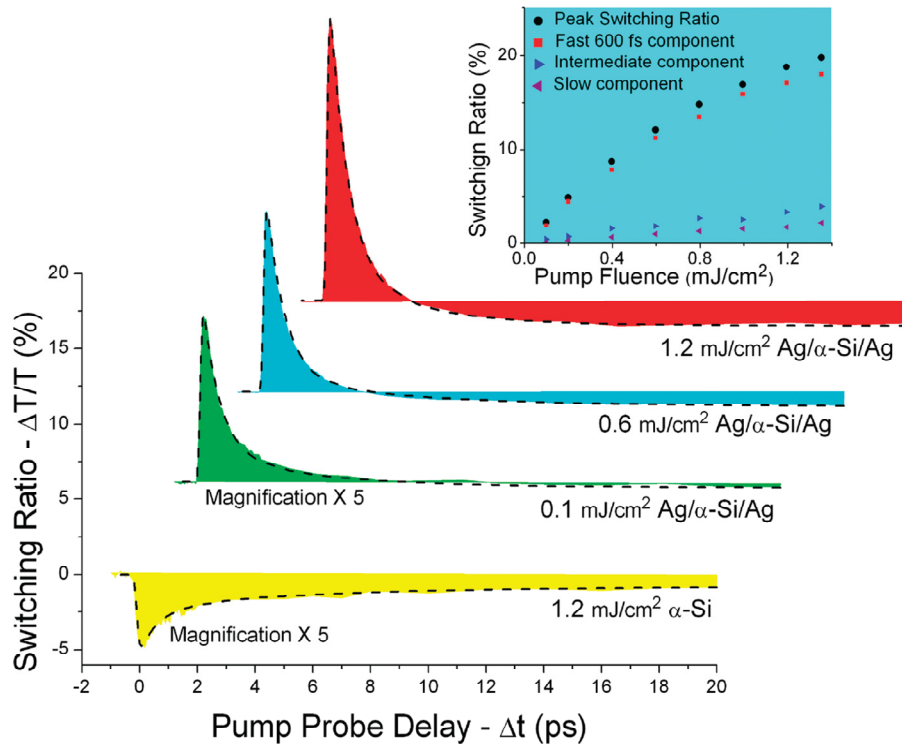


Fig. 5.5 Comparison of pump-probe signal decay times for the eNIM and an unstructured  $\alpha$ -Si film (pump (probe) wavelength 550 (1180) nm). The data (solid colors) is fit to a triple exponential decay function convoluted with a Gaussian function (dashed lines). ( $X$ -offset between traces = 2.2 ps;  $Y$ -offset = 6%) We observe a fast 600 fs component, an intermediate few-picosecond component and a slow nanosecond component in all traces. The dashed lines show a numerical fit to the data using a triple exponential decay function convoluted with a Gaussian function to account for the 120 fs risetime, which corresponds to the finite width of the pump-probe cross-correlation. Inset: peak switching ratio and amplitudes of each component versus fluence.

With a weaker negative index resonance, the electromagnetic nonlinearities are significantly smaller for this perpendicular polarization, resulting in a weaker pump-probe signal, i.e. smaller switching ratio [Fig. 5.4 (b)]. For the remainder of the paper, we focus our attention on the  $E_{\parallel}$  case.

In Fig. 5.5, the metamaterial  $\Delta T/T$  versus pump-probe delay at three different pump fluencies is plotted. Here, the pump (probe) is at 550 nm (1180 nm). A fast 600 fs component, an intermediate few-picosecond component and a slow nanosecond component are observed. The nanosecond decay time cannot be resolved within the limitations of our experiment and is accounted for as a constant negative background. The inset shows the peak switching ratio versus pump fluence and the contributions of each component as extracted from the numerical fits. Over 80% of the signal amplitude is due to the fast 600 fs component, which increases rapidly with pump fluence. A  $\Delta T/T$  of ~20% was obtained at the highest available 550 nm pump fluence of  $1.35 \text{ mJ/cm}^2$ , corresponding to ~3 nJ of pump energy absorbed (and ~6/~1 nJ reflected/transmitted) over the ~30  $\mu\text{m}$  diameter of the probe spot. The 340 nm pitch of our device potentially allows for further focusing of the probe spot, whereby a realistic ~5  $\mu\text{m}^2$  spot size gives us a theoretical lower limit of ~20 pJ for the energy required to modulate a single bit. This is comparable to the current state of the art in energy requirements [4,5]. Pumping at 400 nm with ~2.5  $\text{mJ/cm}^2$  resulted in a 40% switching ratio. However, the 400 nm pump degraded the Ag layer of the sample over time due to the strong metal absorption at this wavelength. The solid yellow curve shows the magnified pump-probe signal from an unstructured 60 nm thick  $\alpha$ -Si film for comparison. A triple exponential decay (dashed line) fits the curve well with a fast

sub-picosecond component, an intermediate few picoseconds component, and a slow component that lasts for >100 ps. The close correspondence of the fast and intermediate decay-time components of  $\alpha$ -Si and the metamaterial suggests that the change in optical properties of the metamaterial is due to the dynamics of the photoexcited carriers in the dielectric  $\alpha$ -Si layer. Further, an unstructured 28 nm film of Ag shows no measurable pump-probe signal under identical conditions. Previous studies on ultrafast carrier dynamics in  $\alpha$ -Si have observed such multi-component decay times and have identified different regimes in the dynamics based on the peak carrier densities [13-15,22]. In particular, for photoexcitation densities  $>\sim 5 \times 10^{19}$ , sub-picosecond decay times were observed in some studies [13-15] and attributed to an Auger recombination process [15]. For a pump fluence of  $1.35 \text{ mJ/cm}^2$  with 60 fs pulses, we obtain a carrier density of  $N = 1.8 \times 10^{20} \text{ cm}^{-3}$  and thereby access this fast recombination regime. To the best of our knowledge, this is the first use of this regime of  $\alpha$ -Si sub-picosecond dynamics in a functional photonic device.

In Fig. 5.6 (a), the metamaterial pump-probe signal is plotted at different probe wavelengths for a 550 nm,  $1.35 \text{ mJ/cm}^2$  excitation. At zero pump-probe delay ( $\Delta t=0$ ), the peak switching ratio goes from positive to negative as the probe is moved to shorter wavelengths relative to the negative index resonance. Additionally, for a fixed probe wavelength, the pump-probe signal changes from positive to negative (or vice versa) as the pump-probe delay is increased. Around the 1130 nm negative index resonance, we observe a sub-picosecond change in  $\Delta T/T$  from negative to positive. Since photoexcitation of  $\alpha$ -Si changes both the real and the imaginary parts of the refractive index, which in turn tune the negative index resonance, the data is suggestive of a dynamic ultrafast tuning of the resonance.



To understand these experimental results, the optical properties of the metamaterial were simulated using CST Microwave Studio with the specific polarization direction shown in Fig. 5.1 (a) [17]. For details, see Chapter 4. We take the refractive index of unphotoexcited  $\alpha$ -Si,  $n_{\alpha\text{-Si}} = 3.4$  and  $n_{\text{substrate}} = 1.5$ . For photoexcited  $\alpha$ -Si, the Drude model [23] gives

$$n_{\text{photoexcited } \alpha\text{-Si}} = \sqrt{\left( n_{\alpha\text{-Si}}^2 - \frac{\omega_p^2}{\omega(\omega + i\gamma)} \right)} \quad (6.1)$$

where  $\omega_p = \sqrt{\left( \frac{e^2 N}{\epsilon_0 m^*} \right)}$  is the plasma frequency,  $\omega$  is the angular frequency of the probe light,  $m^*$  is the effective mass,  $\epsilon_0$  is the permittivity of free space,  $N$  is the photoexcited carrier density, and  $\gamma$  is the scattering rate. Only the electronic contribution is considered given the larger effective mass [13,24] and lower mobility [13,23] for holes. For  $N = 1.8 \times 10^{20} \text{ cm}^{-3}$ , we relate  $\gamma$  to the free carrier mobility by  $\gamma \sim \frac{e}{\mu m^*}$  [26]. For  $m^* = 0.2m_0$  [13,24,27] and  $\mu = 10 \text{ cm}^2/\text{V}\cdot\text{s}$  [13,25,27], we get  $\frac{1}{\gamma} \sim 1 \text{ fs}$  [13,27,28] and  $n_{\text{photoexcited } \alpha\text{-Si}} = 3.27 + i \cdot 0.08$ . For the silver dielectric function, the Drude model is described by  $\omega_p = 9.02 \text{ eV}$  and  $\gamma = 0.052 \text{ eV}$ , where  $\gamma$  is a factor of 2.5 larger than reported for bulk material [20] to account for additional thin-film scattering and fabrication inhomogeneity [16]. Figure 5.6 (b) shows the calculated transmittance of the metamaterial versus wavelength with and without photoexcitation. As the  $\alpha$ -Si layer becomes more conductive with increasing photoexcitation, the transmittance of the metamaterial changes from that of a negative index material to a more metallic plasmonic resonance. Figure 5.6 (c) shows the calculated switching ratio at zero pump-probe delay.

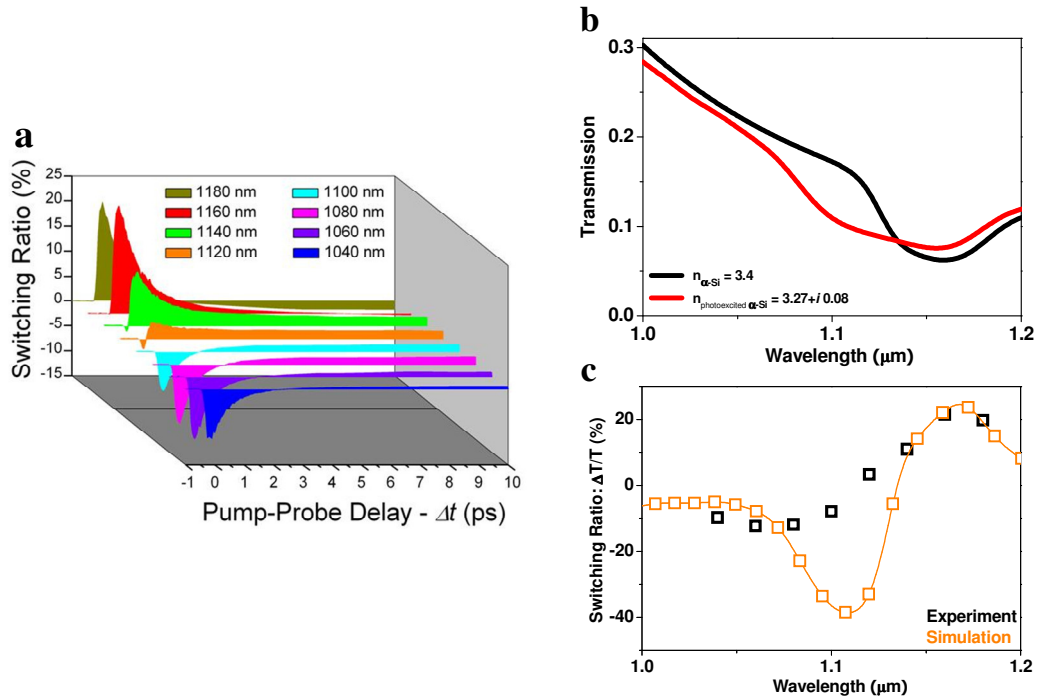


Fig. 5.6 eNIM pump-probe signal at different probe wavelengths (550 nm pump wavelength). (a) Experimental data versus pump-probe delay. (b) Simulated transmittance for photoexcited and unphotoexcited eNIM. (c) Simulated switching ratio versus probe wavelength compared with that measured at zero pump-probe delay.

## 5.3 Second Experimental Demonstration

### 5.3.1 Design and Dimensions

The dual-band ultrafast optical switching device with a negative-index metamaterial (DUOS-NIM) reported here is similar to one as described in section 5.2, except pitch, aperture size, thickness of constituent materials, and fabrication-induced sidewall-angle. The geometrical parameters of the device are indicated in Fig. 5.7 (a). The orthogonal pitches of the two dimensional grating are both fixed at 345 nm. The thicknesses of Ag and  $\alpha$ -Si films are fixed at

28 and 68 nm, respectively. The elliptical aperture size ( $2a_x, 2a_y$ ) is formed with  $0.69 \cdot p$  (238 nm),  $0.47 \cdot p$  (162 nm) in major and minor axis, respectively as shown in Fig. 5.7 (a). The detailed processing steps to fabricate the DUOS-NIM are described in section 5 of Chapter 2.

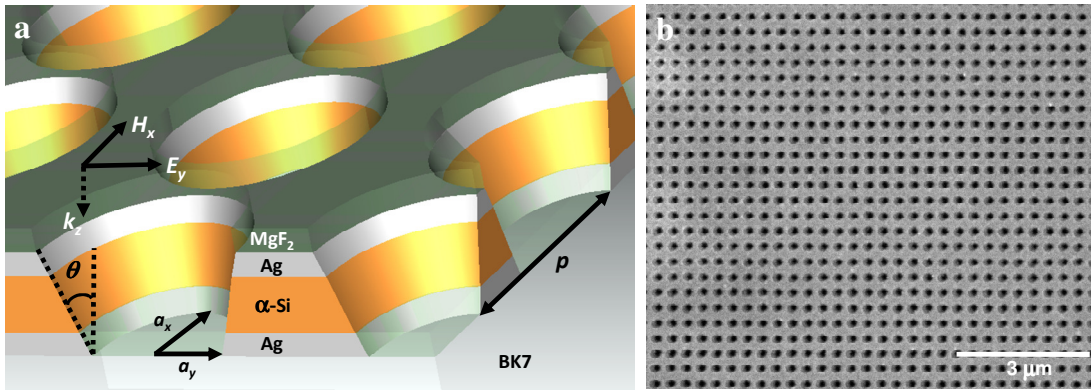


Fig. 5.7 (a) Schematic view of dual-band ultrafast optical switching device with a negative-index metamaterial. Geometrical parameters of elliptical negative-index metamaterial (eNIM),  $p = 345$  nm;  $a_x = 119$  nm;  $a_y = 81$  nm; and  $\theta$  (sidewall-angle) =  $18^\circ$ . The eNIM consists of 28 nm thick Ag; 68 nm thick  $\alpha$ -Si; and 28 nm thick Ag. The direction of polarization incoming light is parallel to the narrower stripe width between apertures (y-axis) and is denoted by  $E_{\parallel}$ . (b) Top view of SEM image of DUOS-NIM.

### 5.3.2 Measurement and Simulation

The transmission was measured using FTIR as explained in section 5.2.2 with the specific polarization ( $E_{\parallel}$ ) as shown in Fig. 5.7 (a). Measured/simulated transmission curve is shown in Fig. 5.8 (a).

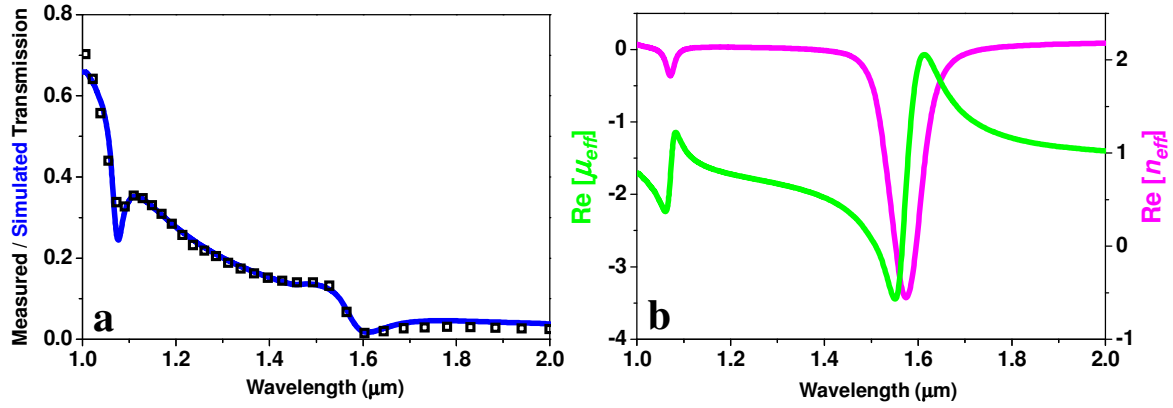


Fig. 5.8 (a) FTIR measured normal incidence transmission spectrum with polarization ( $E_{||}$ ) as indicated in Fig. 5.7 (a). The simulated transmission curve is obtained with CST Microwave Studio [17] using two times the scattering frequency of bulk silver [20] for best fit to the measured transmission. (b) Real part of effective refractive index and permeability.

The optical parameters for constitutive materials ( $n_{\text{substrate}}$ ,  $n_{\text{substrate}}$ ,  $n_{\alpha\text{-Si}}$ ,  $n_{\text{MgF}_2}$ ) are taken from section 5.2. Figure 5.8 (a) gives the best fit between experiment and simulation over 1 to 2  $\mu\text{m}$ , including the range of wavelengths of interest. This gives us sufficient confidence to extract the effective metamaterial parameters (e.g. effective refractive index and permeability) from simulation for the relevant linear polarization as shown in Fig. 5.8 (b). As a result of the structural asymmetry related to the nonzero sidewall-angle ( $\theta = 18^\circ$ ) due to fabrication imperfection as illustrated in Fig. 5.7 (a) [30-32]. For details, see Chapter 4. The structure and design of DUOS-NIM reported here results in two negative index resonances at  $\sim 1.06 \mu\text{m}$  and  $\sim 1.58 \mu\text{m}$  as shown in Fig. 5.8 (b). As explained in section 5.2, the resonances are related to the coupling to the gap-SPPs, which gives rise to a magnetic response and permeability [19,29,33].

### 5.3.3 Pump-Probe Measurement

Figure 5.9 shows the ultrafast pump-probe setup used to study the ultrafast non-linear response of our metamaterial device. Here, a 590 nm pump pulse photoexcites the device and a near-IR probe pulse studies the pump-induced change in properties. Contrary to section 5.2, the signal pulse from the near-IR OPA is tuned to 1200 nm and then frequency doubled to produce the 600 nm visible pump pulse. On the other hand, the idler pulse from the near-IR OPA can range from 930-2300 nm and is tuned to the appropriate wavelength to probe the device response over the entire near-IR. Thereby we access the response of the device over the secondary and fundamental negative index resonances of our device [21,29].

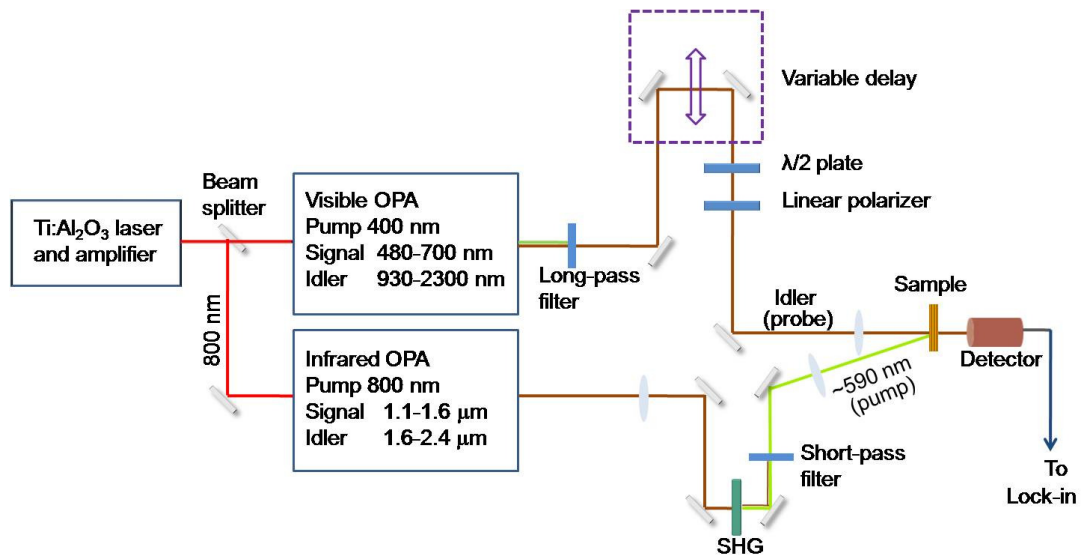


Fig. 5.9 Pump-probe measurement setup

We first study the pump-probe signal for different probe wavelengths, thereby identifying the two negative index resonances. Figure 5.10 shows the time-resolved switching ratio ( $\Delta T/T$ )

versus pump-probe delay for different probe wavelengths around (a) the fundamental and (b) the secondary resonance respectively. As shown in Fig. 5.6 [29], we see positive  $\Delta T/T$  for longer wavelengths around the resonance and negative  $\Delta T/T$  for shorter wavelengths. Figure 5.11 (a) plots the peak switching ratio at zero pump-probe delay versus probe wavelength, where an ‘S’ shaped signature is clearly visible for both the resonances.

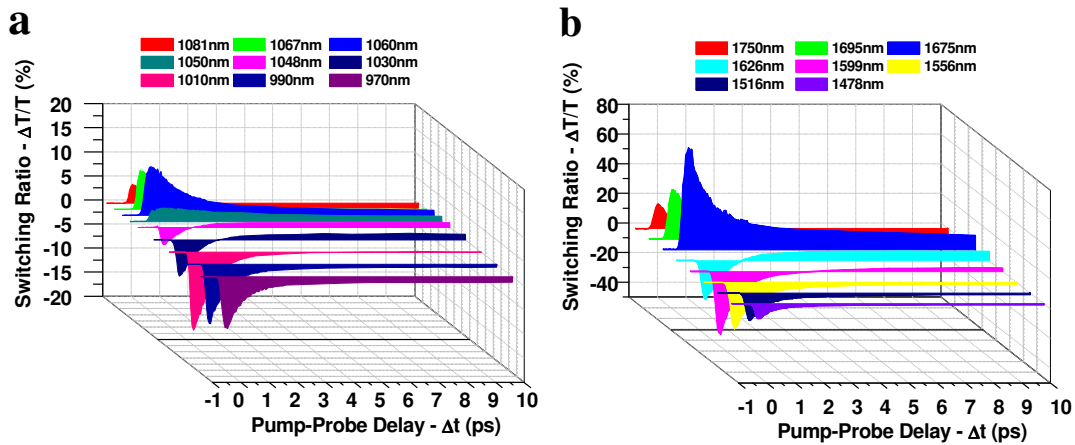


Fig. 5.10 Measured pump-probe response ( $\Delta T/T$ ) versus pump-probe delay ( $\Delta t$ ) for different probe wavelengths around (a) shorter wavelength of negative refractive index resonance ( $\sim 1.06 \mu\text{m}$ ) and (b) longer wavelength of negative refractive index resonance ( $\sim 1.58 \mu\text{m}$ ).

We note that unstructured layers of Ag or  $\alpha$ -Si do not display such a ‘S’-shaped dependence of the peak pump probe signal versus probe wavelength. Moreover,  $\Delta T/T$  for such unstructured layers of Ag or  $\alpha$ -Si is less than 1% as shown in Fig. 5.5 [29]. On the other hand, we see much larger switching ratios with the metamaterial sample. We conclude that the ‘S’ shaped non-linear

response versus probe wavelength is a characteristic signature of the negative index resonance in a fishnet structured metamaterial.

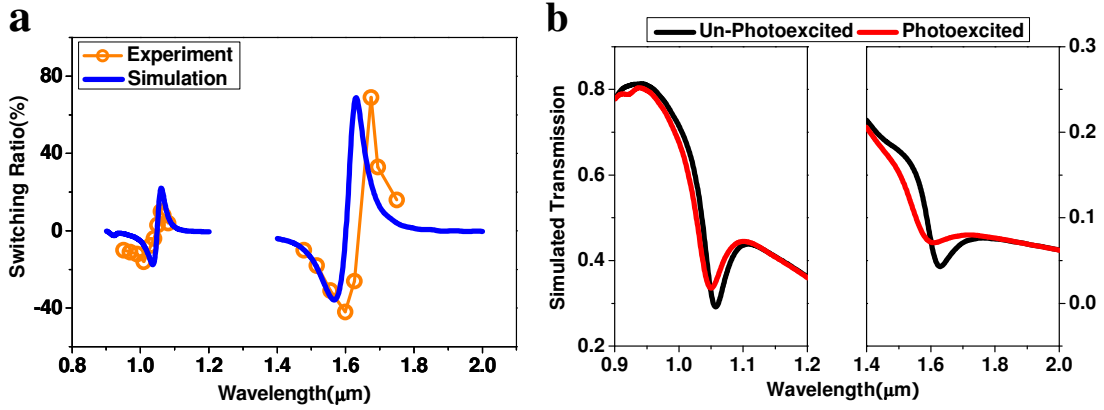


Fig. 5.11 (a) Experimental and simulated peak switching ratios at zero pump delay versus probe wavelength. (b) Comparison of the transmission through the DUOS-NIM around shorter and longer wavelength of negative index.

To numerically calculate the change in refractive index of the  $\alpha$ -Si due to photoexcitation ( $n_{\text{photoexcited } \alpha\text{-Si}}$ ), we apply the Drude model in Eq. 6.1 with parameters: power (7.3mW); spot size (100  $\mu\text{m}$ ); pumping wavelength (590 nm); effective mass ( $0.3m_0$ );  $\gamma^{-1}$  (0.5 fs) at shorter wavelength resonance ( $\sim 1.06 \mu\text{m}$ );  $\gamma^{-1}$  (1 fs) at longer wavelength resonance region; and unphotoexcited  $\alpha$ -Si refractive index (3.35) [13,23-28]. This value of  $n_{\text{photoexcited } \alpha\text{-Si}}$  is then used to calculate the effective parameters of the DUOS-NIM with CST Microwave Studio [17], as was done for the unphotoexcited  $\alpha$ -Si case, which in turn lets us calculate other relevant optical parameters such as transmission. Figure 5.11 (a) shows a comparison between the measured and

simulated pump-probe response at zero time delay over the broad  $1\ \mu\text{m} - 2\ \mu\text{m}$  range. We see very good agreement between experiment and theory. Figure 5.11 (b) compares the transmission through the DUOS-NIM over the  $1\ \mu\text{m} - 2\ \mu\text{m}$  range for the case of photoexcited (red) and unphotoexcited (black)  $\alpha$ -Si layer. We see that for wavelengths just above (below) the negative index resonance, we get increased (decreased) transmission on photoexcitation. Thus, the pump-probe signal at zero time delay versus probe wavelength demonstrates a characteristic ‘S’ shaped signature at the negative index resonance. As the photoexcited carriers decay back to the ground state, one recovers the properties of the unphotoexcited metamaterial as can be seen from the decaying pump probe signals as shown in Fig. 5.10. We note that we get significantly higher switching ratios at the fundamental resonance (+70% and -40% for the positive and negative peaks, respectively) versus the secondary resonance (+10% and -18%) as shown in Fig. 5.11 (a). The significantly larger switching ratio at the fundamental resonance is a result of stronger negative index at fundamental resonance as shown in Fig. 5.8 (b).



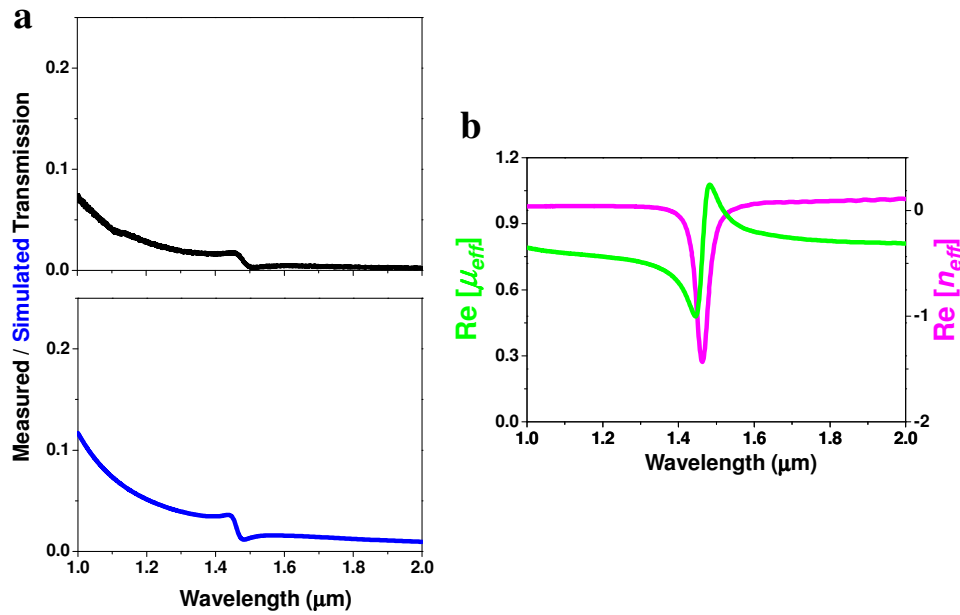


Fig. 5.12 (a) FTIR measured / FIT simulated normal incidence transmission spectra with polarization ( $E_{\perp}$ ). (b) Real part of effective refractive index and permeability using same polarization direction as (a).

The elliptical nature of holes results in a different polarization response in our DUOS-NIM. For the two different polarization samples, the light sees different thickness of the continuous wires that determine the effective permittivity. This results in a negative refractive index that is shifted in frequency as well as of lower figure of merit. Figure 5.8 (b) and Fig. 5.12 (b) show the simulations associated with the negative index resonance for the two polarizations. We see the shifted negative index associated with  $E_{\perp}$  [ $E$ -field perpendicular to the minor axis of the holes shown in Fig. 5.7 (a)] as well as the small resonance. Figure 5.8 (a) and Fig. 5.12 (a) also show the measured/simulated transmission through the DUOS-NIM for the two polarizations. For  $E_{\perp}$ , we see a significantly lowered transmission and the characteristic structure

(dips and peaks) associated with the negative index resonance become less distinct for  $E_{\parallel}$  [16,29]. The simulation is able to well reproduce the features of the FTIR measured curves for both polarizations.

## 5.4 Summary

In summary, we demonstrate a nanometer-scale, sub-picosecond metamaterial device capable of over terabit/second all-optical communication in the near infrared spectrum.

We achieve a 600 fs device response by utilizing a regime of sub-picosecond carrier dynamics in  $\alpha$ -Si and  $\sim 70\%$  modulation in a path length of only 124 nm by exploiting the strong nonlinearities in metamaterials. We identify a characteristic signature associated with the negative index resonance in the pump-probe signal of a fishnet structure. We achieve much higher switching ratios at the fundamental resonance ( $\sim 70\%$ ) relative to the secondary resonance ( $\sim 20\%$ ) corresponding to the stronger negative index at the fundamental resonance.

This device opens the door to other compact, tunable, ultrafast photonic devices and applications.

## 5.5 References

1. M. Saruwatari, "All-optical signal processing for terabit/second optical transmission," *IEEE J. Sel. Top. Quantum Electron.* **6**, 1363–1374 (2000)
2. C. Langrock, S. Kumar, J. McGeehan, A. E. Willner, and M.M. Fejer, "All-Optical Signal Processing using  $\chi^{(2)}$  Nonlinearities in Guided Wave Devices," *J. Lightwave Technol.* **24**, 2579–2592 (2006).
3. C. Manolatou and M. Lipson, "All-optical silicon modulators based on carrier injection by two-photon absorption," *J. Lightwave Technol.* **24**, 1443–1439 (2006).
4. V. R. Almeida, C. A. Barrios, R. R. Panepucci, and M. Lipson, "All-optical control of light on a silicon chip," *Nature* **431**, 1081–1084 (2004).
5. S. F. Preble, Q. Xu, B. S. Schmidt, and M. Lipson, "Ultrafast all-optical modulation on a silicon chip," *Opt. Lett.* **30**, 2901–2893 (2005).
6. A. Y. Elezzabi, Z. Han, S. Sederberg and V. Van, "Ultrafast all-optical modulation in silicon-based nanoplasmonic devices," *Opt. Express* **17**, 11045–11056 (2009).
7. D. Pacifici, H. J. Lezec, and H. A. Atwater, "All-optical modulation by plasmonic excitation of CdSe quantum dots," *Nat. Photonics* **1**, 402–406 (2007).
8. K. F. MacDonald, Z. L. Samson, M. I. Stockman, and N. I. Zheludev, "Ultrafast Active Plasmonics," *Nat. Photonics* **3**, 55–58 (2009).
9. V. M. Shalaev, "Optical negative-index metamaterials," *Nat. Photonics* **1**, 41–48 (2007).
10. W. J. Padilla, A. J. Taylor, C. Highstrete, M. Lee, and R. D. Averitt, "Dynamical Electric and Magnetic Metamaterial Response at Terahertz Frequencies," *Phys. Rev. Lett.* **96**, 107401 (2006).
11. H. T. Chen, W. J. Padilla, J. M. O. Zide, S. R. Bank, A. C. Gossard, A. J. Taylor, and R. D. Averitt, "Ultrafast optical switching of terahertz metamaterials fabricated on ErAs/GaAs nanoisland superlattices," *Opt. Lett.* **32**, 1620–1622 (2007).
12. E. Kim, Y. R. Shen, W. Wu, E. Ponizovskaya, Z. Yu, A. M. Bratkovsky, S. Y. Wang, and R. S. Williams, "Modulation of negative index metamaterials in the near-IR range," *Appl. Phys. Lett.* **91**, 173105 (2007).
13. P. M. Fauchet, D. Hulin, R. Vanderhaghen, A. Mourchid, and W. L. Nighan Jr., "The properties of free carriers in amorphous silicon," *J. Non-Cryst. Solids* **141**, 76–87 (1992).

14. A. Mouchid, R. Vanderhaghen, D. Hulin, C. Tanguy, and P. M. Fauchet, "Femtosecond optical spectroscopy in  $\alpha$ -Si:H and its alloys," *J. Non-Cryst. Solids* **114**, 582–584 (1989).
15. A. Esser, K. Seibert, H. Kurz, G. N. Parsons, C. Wang, B. N. Davidson, G. Lucovsky, and R. J. Nemanich, "Ultrafast recombination and trapping in amorphous silicon," *Phys. Rev. B* **41**, 2879–2884 (1990).
16. Z. Ku and S. R. J. Brueck, "Comparison of negative refractive index materials with circular, elliptical and rectangular holes," *Opt. Express* **15**, 4515–4522 (2007).
17. CST Studio Suite 2006B, <www.cst.com>.
18. S. Zhang, W. Fan, N. C. Panoiu, K. J. Malloy, R. M. Osgood, and S. R. J. Brueck, "Experimental demonstration of near-infrared negative-index metamaterials," *Phys. Rev. Lett.* **95**, 137404 (2005).
19. A. Mary, S. G. Rodrigo, F. J. Garcia-Vidal, and L. Martin-Moreno, "Theory of negative-refractive-index response of double fishnet structures," *Phys. Rev. Lett.* **101**, 103902 (2008).
20. P. B. Johnson and R. W. Christy, "Optical Constants of the Noble Metals," *Phys. Rev. B* **6**, 4370–4379 (1972).
21. R. P. Prasankumar, S. Choi, S. A. Trugman, S. T. Picraux, and A. J. Taylor, "Ultrafast Electron and Hole Dynamics in Germanium Nanowires," *Nano Lett.* **8**, 1619–1624 (2008).
22. I. A. Shkrob and R. A. Crowell, "Ultrafast charge recombination in undoped amorphous hydrogenated silicon," *Phys. Rev. B* **57**, 12207–12218 (1998).
23. M. Dressel and G. Gruner, "Electrodynamics of Solids" Cambridge University Press, New York, Chapter 5 (2002).
24. J. I. Pankove, "Hydrogenated Amorphous Silicon," Academic Press, Orlando (1984).
25. R. A. Street, "Hydrogenated Amorphous Silicon," Cambridge University Press, New York (1991).
26. J. Singleton, "Band Theory and Electronic Properties of Solids," Oxford University Press, New York, Chapter 9.3 (2001).
27. T. Y. Choi, D. J. Hwang, and C. P. Grigoropoulos, "Ultrafast laser-induced crystallization of amorphous silicon films," *Opt. Eng.* **42**, 3383–3388 (2003).
28. K. Sokolowski-Tinten and D. Von der Linde, "Generation of dense electron-hole plasmas in silicon," *Phys. Rev. B* **61**, 2643–2650 (2000).

29. Keshav M. Dani, Zahyun Ku, Prashanth C. Upadhya, Rohit P. Prasankumar, S. R. J. Brueck, and Antoinette J. Taylor, "Subpicosecond Optical Switching with a Negative Index Metamaterial," *Nano Lett.* **9**, 3565-3569 (2009).
30. Zahyun Ku and S. R. J. Brueck, "Experimental demonstration of sidewall-angle-induced bianisotropy in multiple-layer negative-index metamaterials," *Appl. Phys. Lett.* **94**, 153107 (2009).
31. Zahyun Ku, J. Zhang, and S. R. J. Brueck, "Bianisotropy of multiple-layer fishnet negative-index metamaterials due to angled sidewalls," *Opt. Express* **17**, 6782–6789 (2009).
32. Zahyun Ku, Keshav M. Dani, Prashanth C. Upadhya, and S. R. J. Brueck, "Bi-anisotropic negative-index metamaterial embedded in a symmetric medium", *Journal of the Optical Society of America B* **26**, B34-B38 (2009).
33. R. Ortuno, C. Garcia-Meca, F. J. Rodriguez-Fortuno, J. Marti, and A. Martinez, "Role of surface plasmon polaritons on optical transmission through double layer metallic hole arrays," *Phys. Rev. B* **79**, 075425 (2009).

## Chapter 6 Future Work

In this chapter, we propose the integration of surface plasmonic structure to infrared focal plane array in section 6.1 and the polarization-dependent dual-band near-infrared metamaterial-absorber in section 6.2.

### 6.1 Infrared Focal Plane Array integrated with a Surface Plasmonic Structure

In the past few years, there has been increasing interest in surface plasmon polaritons (SPPs), as a result of the strongly enhanced electric fields in the local vicinity of a resonant coupling structure such as a metal film perforated with a 1D or 2D hole arrays [1]. Various optoelectronic devices such as lasers, detectors, filters and solar cells are expected to benefit from this enhancement which allows spectro-polarimetric control over emission and detection process [2,3]. For example, resonance enhancement of the photocurrent in single pixel detectors using various plasmonic structures has been demonstrated [4-6]. Here, we demonstrate the first monolithically integrated plasmonic focal plane array (FPA) in the mid-infrared spectral region, using a metal with a 2D hole array on top of an intersubband quantum-dots-in-a-well (DWELL) heterostructure coupled to a read-out integrated circuit (ROIC).

#### 6.1.1 Design and Fabrication of Surface Plasmonic Structure

In order to determine the optimized surface plasmonic (SP) structure to integrate with the FPA, a series of 2D square titanium (Ti)/gold (Au) SP hole arrays with various pitches (i.e.  $p =$

1.79, 1.89, 2.0, 2.08, 2.33  $\mu\text{m}$ ) were fabricated on substrate consisting of a 1  $\mu\text{m}$  thick n-type gallium arsenide (GaAs) layer with a free electron density of  $n = 2 \times 10^{18} \text{ cm}^{-3}$  grown on a semi-insulating GaAs (SI-GaAs) wafer by molecular beam epitaxy (MBE). A 2D square array of circular apertures was formed with a nominal ratio of diameter  $d$  to lattice spacing  $p$ ,  $d/p \sim 0.5$ . The processing steps to fabricate the SP structure with circular aperture are as follows. (I) A positive-tone photoresist (PR) was spin-coated at 4K rpm for 30 s and oven-baked at 95°C for 3 min. (II) Interferometric lithography (IL) procedure is discussed in Chapter 2 except post-baking at 110°C for 1 min and developing for 1 min; a periodic circular post pattern is shown in Fig. 6.1 (a). (III) After the PR pattern was defined, e-beam evaporation was used to deposit a 5-nm thick adhesion layer of Ti, followed by 45 nm of Au. (IV) Liftoff processing with an acetone; finally, SP structure with 2  $\mu\text{m}$  pitch is shown in Fig. 6.1 (b). In addition, IL was used to fabricate large-area (1.5 $\times$ 1.5  $\text{cm}^2$ ), uniform samples, and making sample characterization convenient as described in Chapter 3 [7-9].

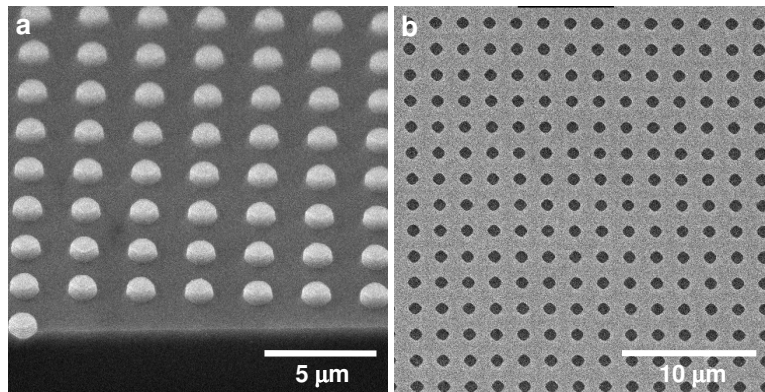


Fig. 6.1 Scanning electron microscopy (SEM) image of (a) a periodic circular post PR pattern defined by IL. (b) Ti/Au samples with circular holes.

### 6.1.2 Measurement and Simulation to Find an Optimized SP structure

The transmission was recorded with a Nicolet FTIR spectrometer with a KBr beam splitter and a DTGS-KBr detector. The linear transmission spectra were carried out a normal incidence to the samples and normalized to the transmission through a bare substrate (as explained above) as shown in Fig. 6.2. In case of symmetric SP structure with circular apertures, an unpolarized FTIR beam was used to measure the transmission.

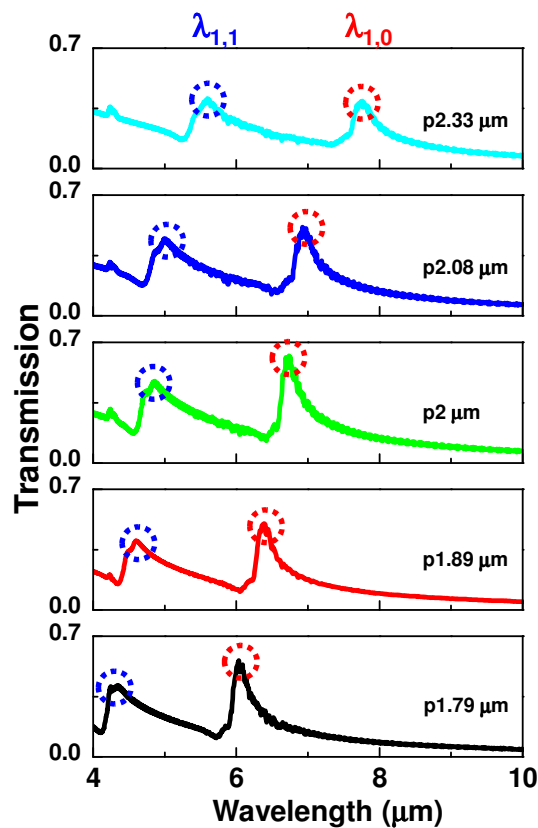


Fig. 6.2 FTIR linear transmission of SP structure with variable pitches (1.79, 1.89, 2.0, 2.08, 2.33 μm) with first and second order SP resonances.



For normal incidence, the SP resonance wavelengths are given by

$$\lambda_{i,j} = \frac{p \cdot \text{Re} \left( \sqrt{\frac{\epsilon_d \cdot \epsilon_m}{\epsilon_d + \epsilon_m}} \right)}{\sqrt{i^2 + j^2}} \quad (6.1)$$

where  $i$  and  $j$  are integer indices indicating the order of the coupling,  $p$  is the pitch of SP structure,  $\epsilon_k$  is the complex permittivity [ $\epsilon_k = \epsilon_k' + i\epsilon_k''$ , where  $k = d$  (*dielectric*) or  $m$  (*metal*)] [3,10,11]. SP structure fabricated on substrate is embedded in asymmetric medium, i.e. air and substrate. As illustrated in Fig. 6.3, there are two SP modes – SP mode at interface between air and Au ( $\text{SP}_{\text{air/Au}}$ ), and SP mode at interface between Au and substrate ( $\text{SP}_{\text{Au/substrate}}$ ). Here, only  $\text{SP}_{\text{Au/substrate}}$  is observed because the first order resonance of  $\text{SP}_{\text{air/Au}}$  is away from wavelength of interest here, e.g.  $\lambda_{1,0}$  of  $\text{SP}_{\text{air/Au}} \sim p$ .

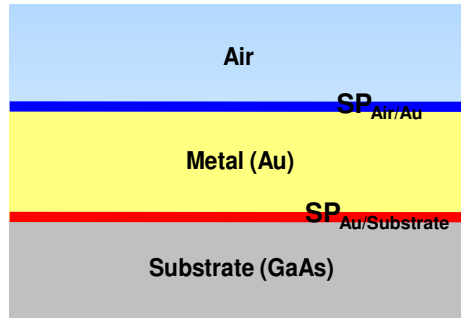


Fig. 6.3 SP mode at each interfaces (Air/Au or Au/Substrate).

In order to obtain the electromagnetic response of the SP structures, they were modeled using a both finite integration technique (CST Microwave Studio) and a rigorous coupled wave

analysis (RCWA) [12-14]. Detailed simulations were described in previous Chapters. The Drude model for Au permittivity at frequencies of interest here is described by  $\omega_p$  (plasma frequency) = 9.02 eV and  $\omega_c$  (collision frequency) = 0.027 eV [15]. The refractive index of the material ( $n_{eff}$ ) was taken as the effective index of the first order ( $i, j = 1, 0$  or  $0, 1$ ) response of the surface plasmon modes,  $n_{eff} = \sqrt{\epsilon'_d} \sim \frac{\lambda_{1,0}}{p}$  because of  $|\epsilon'_m| \gg \epsilon'_d, \epsilon''_m \gg \epsilon''_d$  and  $\epsilon'_d \gg \epsilon''_d$  as shown in Fig. 6.4 [16]. Figure 6.2, Fig. 6.4 and Eq. 6.1 show the resonance wavelengths increased with the pitch, experimentally and theoretically. Figure 6.5 shows the FTIR measured transmission and simulated transmission/absorption for SP structure with 1.79  $\mu\text{m}$ . Due to the absorption shown in Fig. 6.5, it is expected that the spectral response of FPA with SP structure (SP-FPA) is enhanced at  $\lambda_{1,0}, \lambda_{1,1}$  corresponding to first/second order resonance of 1.79  $\mu\text{m}$  pitch-SP structure, respectively. Moreover, good agreement for first/second order of 1.79  $\mu\text{m}$  pitch-SP structure is obtained between the transmission measurement and simulation result. Because the quantum dot infrared detector (QDIP) of interest here was designed to have the strongest spectral response at  $\sim 6.1 \mu\text{m}$ , a pitch of 1.79  $\mu\text{m}$  was chosen for the SP structure.

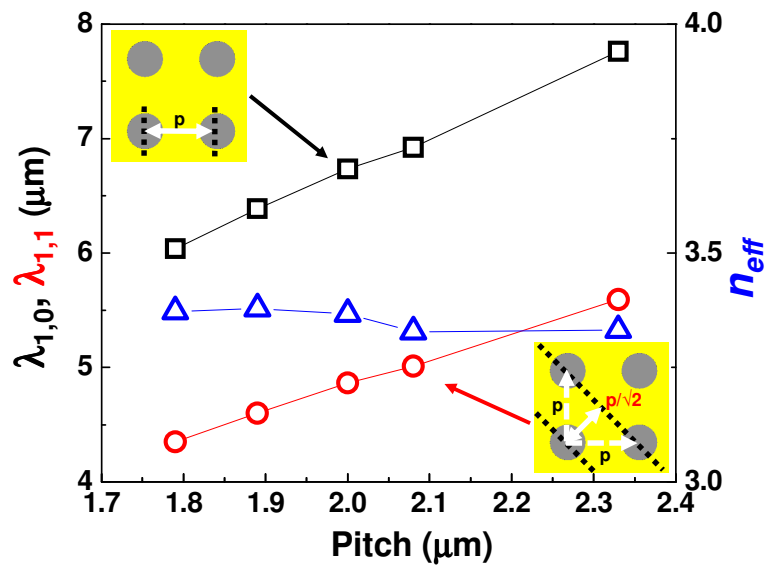


Fig. 6.4 Measured first/second order SP resonance wavelengths from FTIR transmission spectra as shown in Fig. 6.2 and calculated effective refractive index of substrate. Insets represent the first/second order resonance of  $\text{SP}_{\text{Au/substrate}}$ .

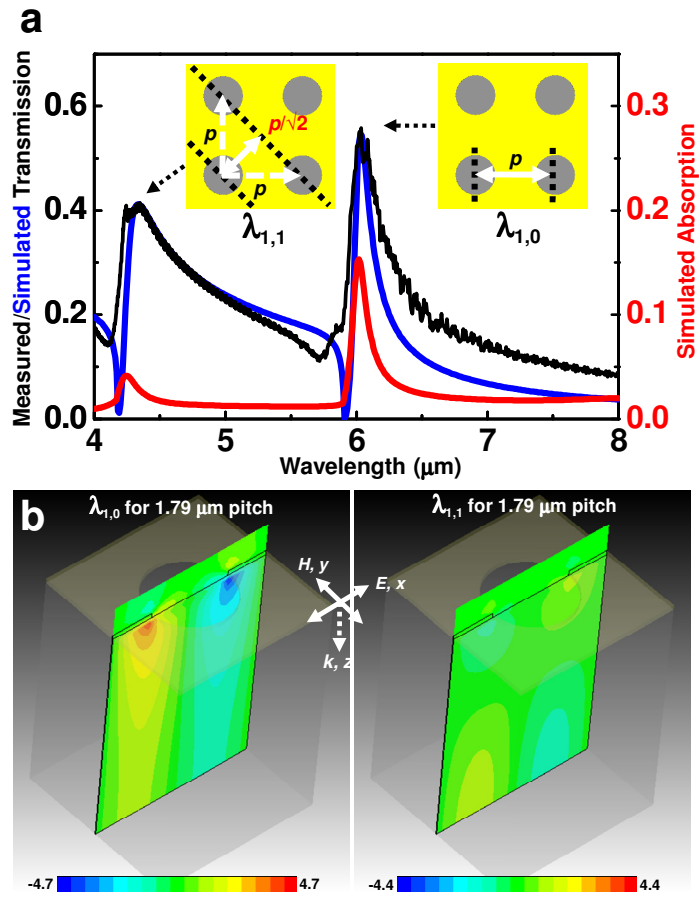


Fig. 6.5 (a) Measured transmission and simulated transmission/absorption of SP structure (1.79  $\mu\text{m}$  pitch shown in Fig. 6.2) on 1  $\mu\text{m}$  n-type GaAs/SI-GaAs using FTIR and a RCWA simulation. (b) Simulated the  $z$ -component of electric field distribution ( $E_z$ ) in  $xz$ -plane through middle of structure (along with diameter) at the corresponding resonant frequencies ( $\lambda_{1,0} \sim 6.1 \mu\text{m}$  and  $\lambda_{1,1} \sim 4.3 \mu\text{m}$  modes as shown in (a)). A pitch of 1.79  $\mu\text{m}$  was used in the fabrication of the SP on the DWELL-FPA.

### 6.1.3 FPA integrated with SP

The absorber consists of 20 stacks of a InAs/In<sub>0.15</sub>Ga<sub>0.85</sub>As DWELL structure sandwiched between two n-GaAs contact layers of 200 nm (top) and 1000 nm (bottom), respectively, and separated from the substrate by a 30 nm AlAs etch-stop barrier.

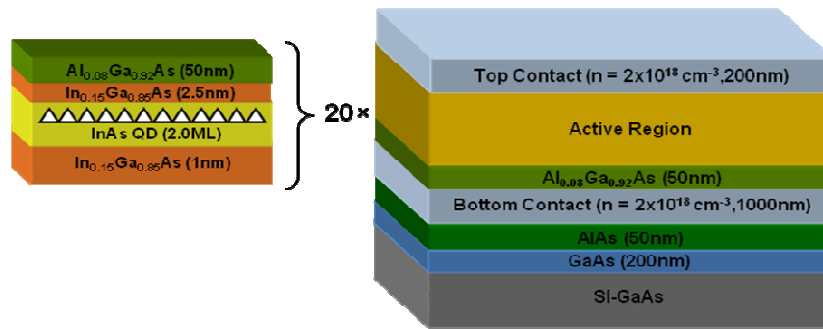


Fig. 6.6 Quantum dot infrared photodetector (QDIP) structure with the absorption region consisting of 20 stacks of InAs quantum dots.

After the epitaxial growth, the wafer was processed into a 320×256 FPA with a 30 μm pixel pitch using standard semiconductor processing (standard optical lithography, inductively coupled plasma etching, plasma enhanced chemical vapor deposition, contact metal and under-bump metal deposition). After this, indium bumps were deposited and the FPA was hybridized to an Indigo 9705 ROIC, and the substrate was removed using a series of mechanical polishing and dry etching steps ending at the 50 nm AlAs etch-stop layer. Following the substrate removal, 1.79 μm pitch-SP structure was fabricated using IL as explained in section 6.1.1. Half of the FPA was protected with a thick polymer layer as the sacrificial layer during this fabrication, leading to final structure as shown in Fig. 6.7.

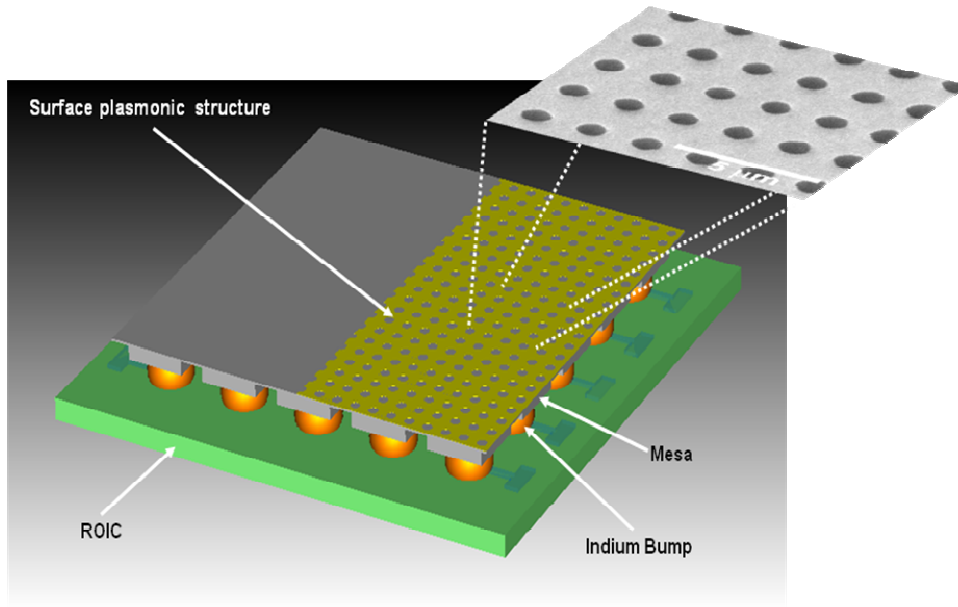


Fig. 6.7 Schematic view of the SP structure integrated with DWELL-FPA.

#### 6.1.4 Measurement and Simulation of SP-FPA

Figure 6.8 (a) represents the measured spectral responses for SP-FPA and FPA (without SP structure) by monochromator. Enhanced spectral responses were observed at first and second order SP resonances,  $\sim 6.1 \mu\text{m}$  (f) and  $\sim 4.3 \mu\text{m}$  (e), respectively. In Fig. 6.8 (b), the simulated absorption (using different  $k$  at (1,0) and (1,1) resonances) provides a good quantitative agreement in terms of resonance wavelengths, linewidth and relative strengths. The indicated absorption (corresponding to  $n+ik$ ) is due to the QDIP material; was adjusted to fit to the measurement; and provides a qualitative estimate of the propagation length along the pixel. A  $k = 0.04$  corresponds to a SP absorption length of  $\sim 12 \mu\text{m}$ , less than the pixel linear dimension. Moreover, it is clear that at  $5.95 \mu\text{m}$  ( $\sim$  first resonance) and  $4.54 \mu\text{m}$  ( $\sim$  second resonances), the

response of the SP-FPA is brighter than that of the FPA [as shown in (e), (f)], whereas the effect is reversed off resonance [as shown in (d), (g)].

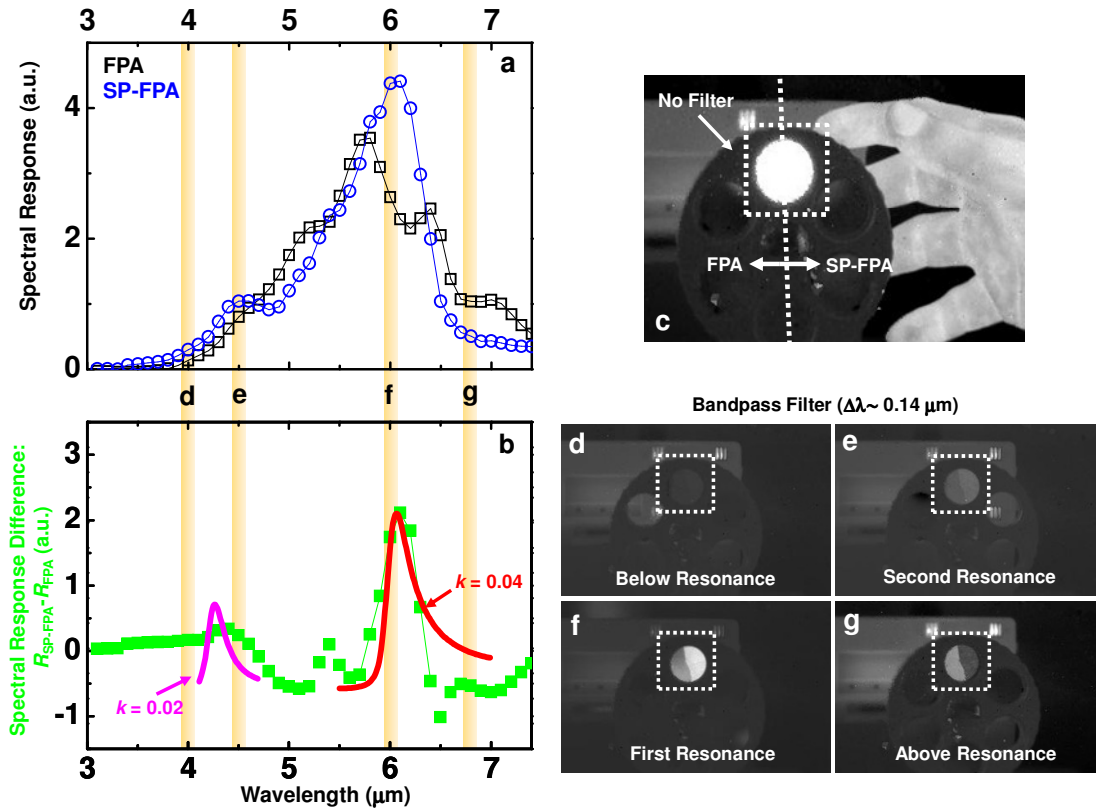


Fig. 6.8 (a) Spectral response of the two halves of the SP-FPA using a monochromator system. (b) Difference of spectral responses showing the experimentally observed peaks. Theoretically modeled first and second SP resonances are also shown using  $k = 0.04$  and  $k = 0.02$ , respectively ( $k$  is the absorption coefficient of QD layer). (c) Representative image of blackbody seen through the open slot (no filter). Infrared image of the blackbody (d) below the (1,1) resonance at  $3.99 \mu\text{m}$ , (e) near the (1,1) resonance at  $4.54 \mu\text{m}$ , (f) close to the (1,0) resonance at  $5.95 \mu\text{m}$  and (g) beyond the (1,0) resonance at  $6.83 \mu\text{m}$ .

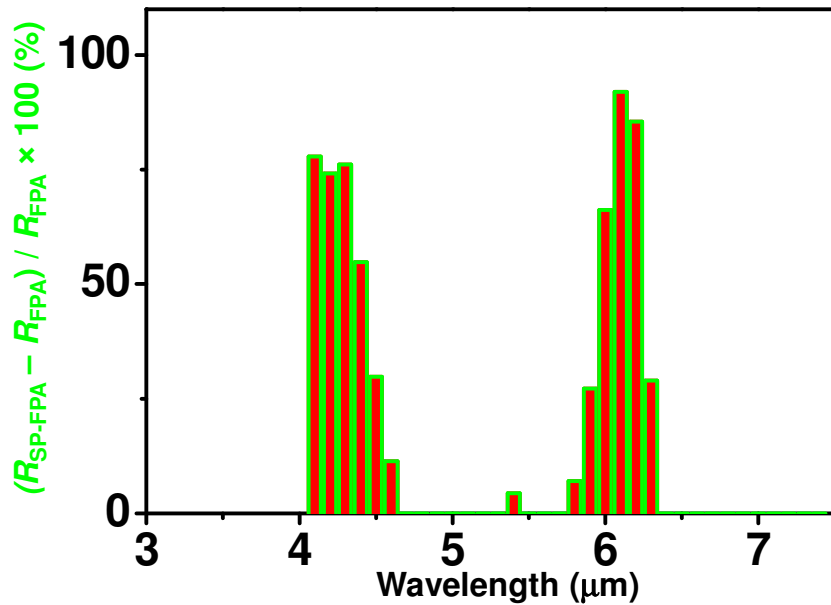


Fig. 6.9 Enhancement of the spectral responses owing to SP structure versus wavelength.

Figure 6.9 is expressed as a percentage, which allows clearer enhancement of spectral response resulting from SP structure. Compared with FPA (FPA without SP structure), response with SP-FPA (FPA with 1.79 μm pitch-SP structure) is increased by ~90% at first order SP resonance wavelength (~6.1 μm) and is enhanced by ~75% at second order SP resonance wavelength (~4.3 μm).

It is worth pointing out that the ratio of the signal voltage ( $V_s$ ) to the noise voltage ( $V_n$ ) whose enhancement is more than 160%.

This work is the first demonstration of a monolithically integrated plasmonic FPA in the mid-infrared spectral region. As compared with conventional FPA (without SP structure), SP-



FPA results in  $\sim 2\times$  ( $\sim 1.8\times$ ) enhancement at first (second) order SP resonance. In addition, results and analyses here could be improved by

1. Thinner bottom contact layer: closer the SP structure to the active region.
2. More information of FPA constituents for simulation: better analyses of SP-FPA.
3. Thinner active region: less dark current. As the compensator to prevent less probability to generate the photocurrent in active region, SP structure can be used with infrared photodetector.

We would like to acknowledge Sanjay Krishna's group for this work.

## **6.2 Polarization-Dependent Dual-band Near-Infrared Metamaterial-Absorber**

### **6.2.1 Basic idea**

The schematic view of proposed metamaterial-absorber (MAA) structure is shown in Fig. 6.10 (a). Due to the presence of the thick Au, the transmission of the structure is totally eliminated across the entire near-infrared frequency regime, yielding absorption to be  $1 - R$  (reflectance). Therefore, in order to have high absorption, MMA can be designed by manipulating the effective permittivity ( $\epsilon$ ) and permeability ( $\mu$ ) to have low reflectance associated with good impedance ( $\xi$ ) matching with free space at absorption resonance. In addition, magnetic resonant frequency can be tuned by varying the capacitance in an equivalent  $LC$  circuit as shown in Fig. 6.10 (b). Capacitance defined by  $C = \epsilon \frac{A}{d}$ , depends on both structural geometry and refractive index of materials between metal plates. Here,  $A$  is the area of metal plates,  $d$  is the distance between metal plates, and  $\epsilon$  is the permittivity of material between metal

plates.  $A$  and  $d$  are all fixed, however  $\epsilon$  can be controlled by the shape and the thickness of polymeric material using an  $O_2$  plasma reactive ion etch (RIE) processing.

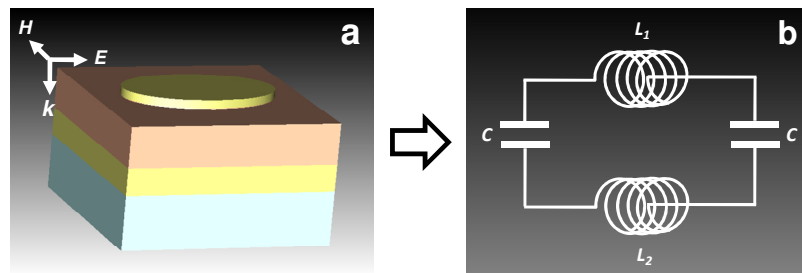


Fig. 6.10 (a) Schematic view of proposed structure. (b) Equivalent  $LC$  circuit of (a).

The decrease of an effective refractive index between metal plates can be explained with RIE processing time as described in Fig. 6.11. It results in a moving absorption resonance to shorter wavelength, i.e.  $\lambda \propto \frac{1}{\omega} \propto \sqrt{LC} \propto \sqrt{\epsilon_d}$ , where  $\epsilon_d$  is the relative permittivity of material between metal plates ( $n_{\text{eff}} = \sqrt{\epsilon_d}$ ).

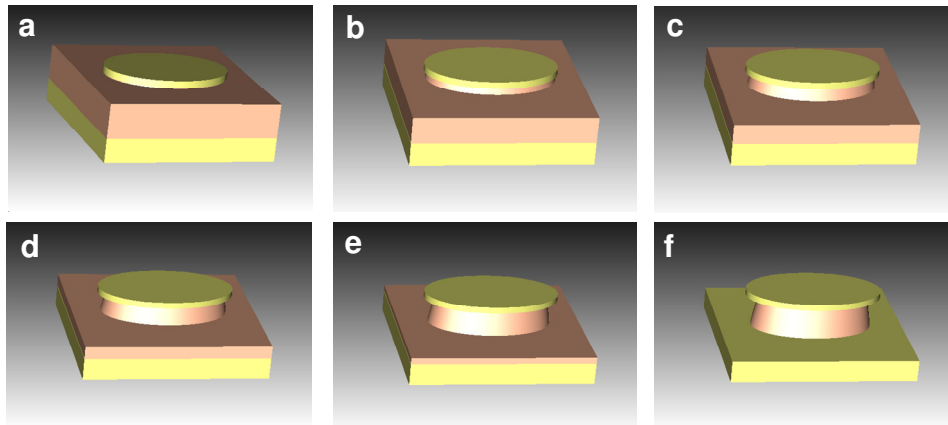


Fig. 6.11 Sequence of schematic views of changing shape and thickness of MMA depending on RIE processing. For example, (a) shows no etched MMA and (f) shows fully RIE etched MMA. The variety results in change of effective refractive index between metal plates.

## 6.2.2 Dimension, Fabrication and SEM images

Figure 6.12 illustrates the geometry of the MMA structure and the incident light polarization configuration. It consists of two functional layers. The top layer is a two-dimensional square periodic array of elliptical Au disks and the bottom layer is thick continuous layer as a mirror. These two layers are separated by a polymeric material (BARC) spacer. Detailed information of BARC is described in Chapter 2. The orthogonal pitches of the 2D gratings are both fixed at 800 nm ( $p$ ). The elliptical disk size ( $a, b$ ) is 570 nm and 375 nm in major and minor axes. The thickness of an elliptical Au disk, a polymeric material film and a thick Au film (as the mirror) are 30 nm, 50nm, and 100 nm, respectively.

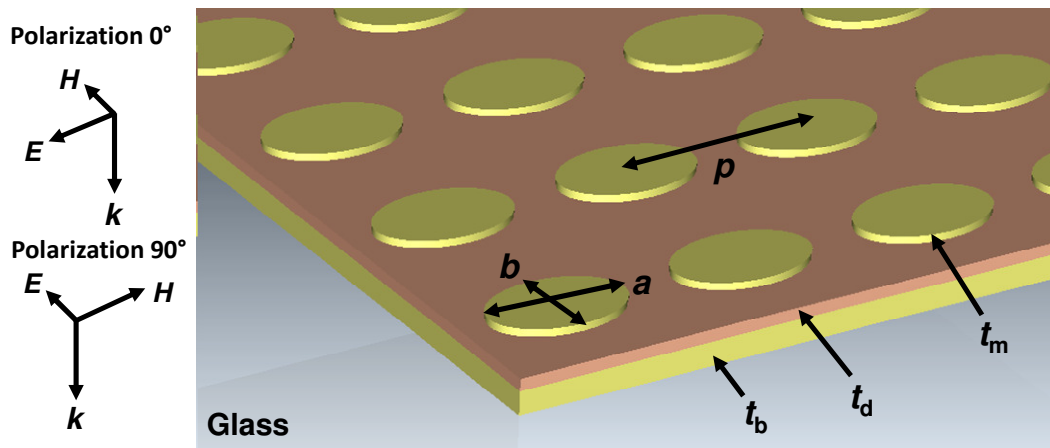


Fig. 6.12 Schematic tilted view of the MMA with geometrical parameters. In addition, the configuration of polarization and propagation is depicted ( $E$ ,  $H$ , and  $k$  denote electric field, magnetic field, and wave vector, respectively) and is denoted by polarization  $0^\circ$  ( $E$  perpendicular to the minor axis) with perpendicular polarization denoted by polarization  $90^\circ$  ( $E$  parallel to the minor axis).

Pitch	Elliptical disk size	Thickness of Elliptical Au disk	Thickness of Polymeric film	Thickness of bottom Au plate
$p$	$a, b$	$t_m$	$t_d$	$t_b$
800	570, 375	30	50	100

Table 6.1 MMA geometrical parameters (all dimensions in nm)

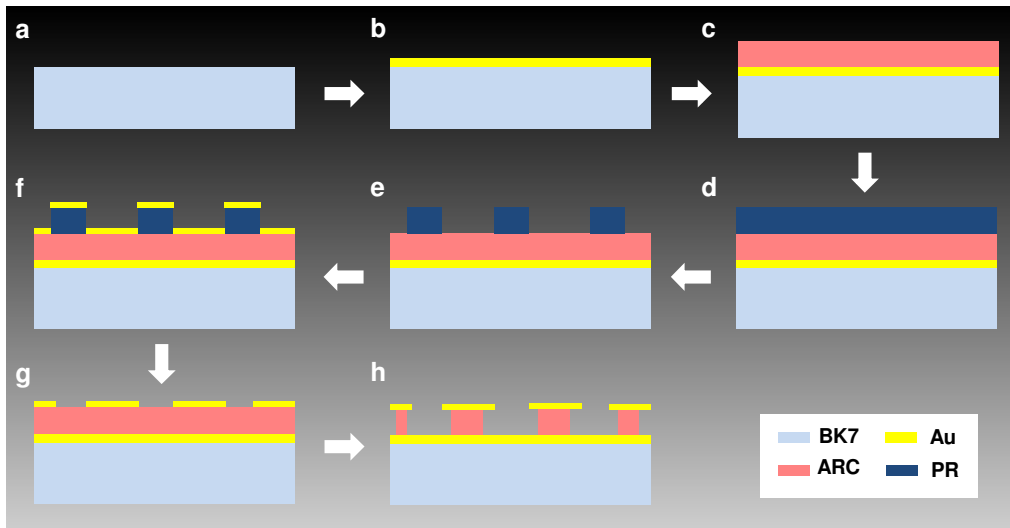


Fig. 6.13 Schematic view of fabrication procedure.

In brief, the processing steps to fabricate the MMA are as follows. (I) Clean BK7 glass substrate. (II) e-beam evaporation of Au as the mirror. (III) Coat the bottom anti-reflection coating (BARC) and negative-tone photoresist (NPR) in sequence. (IV) Patterning of 2D hole array in PR layer by interferometric lithography (IL). (V) e-beam deposition of Au. (VI) Lift-off processing with acetone. (VII) An O<sub>2</sub> plasma RIE processing (0 s, 45 s, 90 s, 135 s) was used to change the shape and thickness of the polymeric film between an elliptical Au disk and an Au mirror, leading to final structure, as shown in Fig. 6.14.

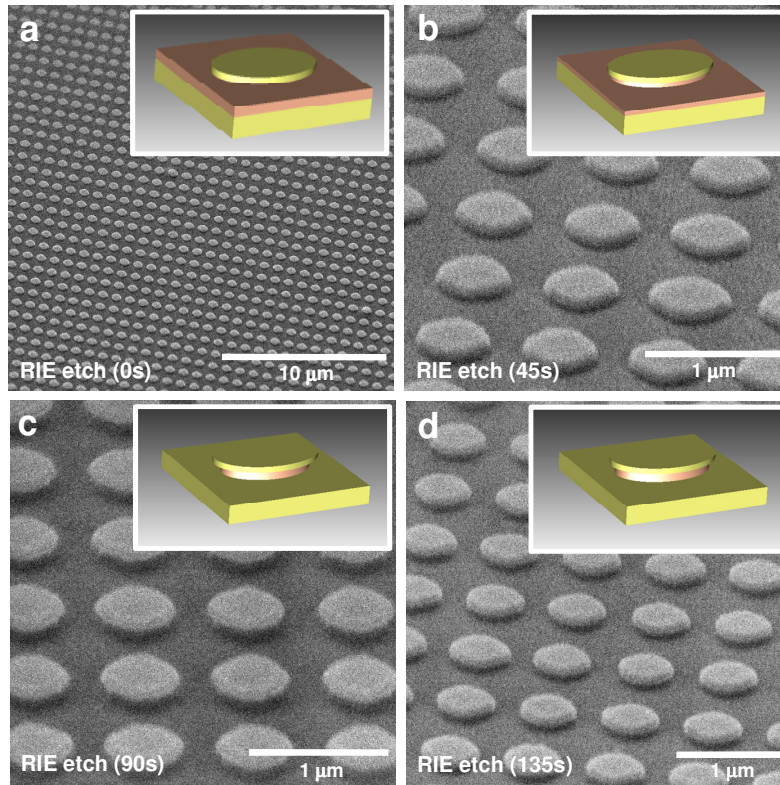


Fig. 6.14 SEM images (tilted view) of MAA depending on O<sub>2</sub> plasma RIE processing for (a) 0 s, (b) 45 s, (c) 90 s, (d) 135 s.

### 6.2.3 Measurement and Simulation

The transmission and the reflectance were measured with a Nicolet FTIR spectrometer with the specific polarization shown in Fig. 6.15, a quartz beam splitter, and a DTGS-KBr detector. The reflectance was measured with an 11° off-normal incident beam and was normalized with respect to the spectrum reflected from an Au mirror as the reference. The top row of Fig. 6.15 shows the measured reflectance depending on the polarization direction and RIE processing time.

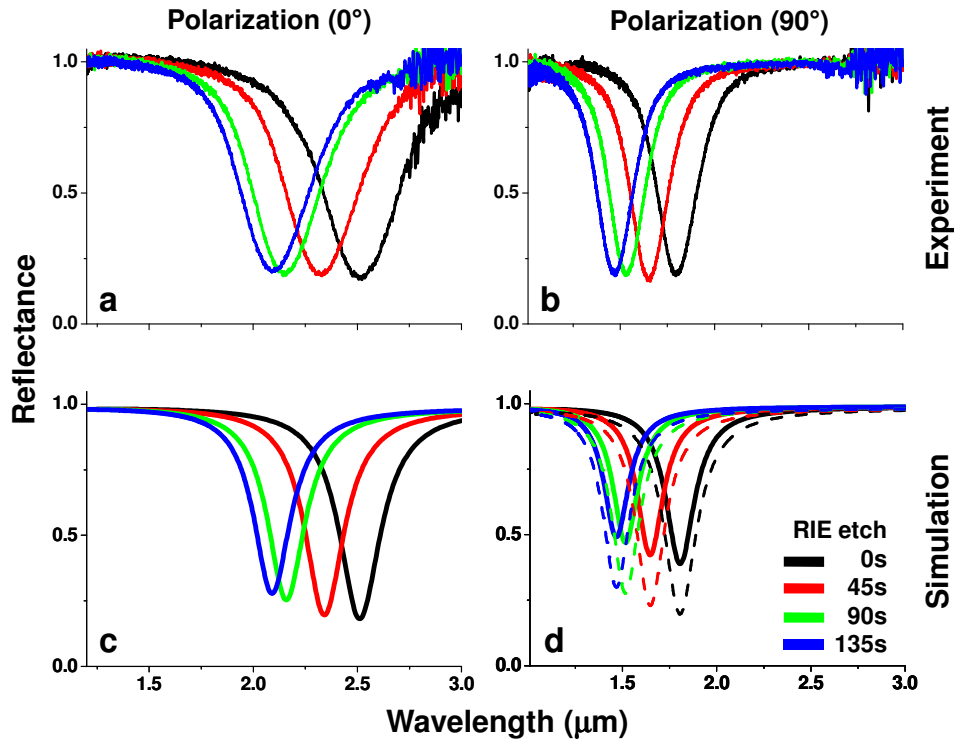


Fig. 6.15 (a), (b) Measured (top) and (c), (d) Simulated (bottom) reflectance spectra for MMA with polarization  $0^\circ$ ,  $90^\circ$ , and  $O_2$  RIE processing for 0 s, 45 s, 90 s, 135 s. The simulated reflectance curves are obtained with CST Microwave Studio [12], which are in good agreement with the FTIR measured reflectances for polarization  $0^\circ$  ( $90^\circ$ ) using 1.5 (2.5) times the scattering frequency ( $\omega_c$ ) of bulk Au [15]. In (d), solid and dashed lines represent  $1.5 \times \omega_c$ ,  $2.5 \times \omega_c$ , respectively.

To investigate the resonant behavior of the MMA structure, numerical simulations were performed by employing a FIT method (CST Microwave Studio) [12]. We used PEC and PMC boundary conditions between unit cells with  $\epsilon_{ARC} = 2.89$ ,  $\epsilon_{substrate} = 2.25$  and Drude model for Au permittivity, where plasma frequency  $\omega_p = 9.02$  eV and scattering frequency  $\omega_c = 0.041$  (0.068)

eV for polarization  $0^\circ$  ( $90^\circ$ ). Higher scattering frequency is explained with details in Chapter 3. 1.5 (2.5) times the scattering frequency of bulk Au was found to give the best fit between experiment and simulation using polarization  $0^\circ$  ( $90^\circ$ ) over  $1\ \mu\text{m}$  to  $3\ \mu\text{m}$  as shown in Fig. 6.15.

For more RIE processing time, absorption resonances ( $1 - R$ ) is shifted towards shorter wavelength due to less effective refractive index in material between elliptical Au disks and thick Au film as explained in section 6.2.1. However, absorption resonance from 90 s to 135 s is not shifted as much as other cases. The shape of polymeric material between Au plates is hardly changed because MMA structure is already, fully RIE-etched for 90 s. It results in a small shift of absorption resonance.

So far, we have experimentally and numerically demonstrated the metamaterial-absorber depending on the polarization and the RIE processing in the near-infrared region. Further numerical studies to calculate the effective parameters using the modified retrieval method are needed to interpret the behavior of metamaterial-absorber in detail.



## 6.3 References

1. T. W. Ebbesen, H. J. Lezec, H. F. Ghaemi, T. Thio, and P. A. Wolff, "Extraordinary optical transmission through subwavelength hole arrays," *Nature* **391**, 667-669 (1998).
2. T. Xu, Y.-K. Wu, X. Luo, and L. J. Guo, "Plasmonic nanoresonators for high-resolution color filtering and spectral image," *Nature Communications* **1**, 1-5 (2010).
3. C. Genet and T. W. Ebbesen, "Light in tiny holes," *Nature* **445**, 39-46 (2007).
4. J. Rosenberg, R. V. Shenoi, T. E. Vandervelde, S. Krishna, and O. Painter, "A multispectral and polarization-selective surface-plasmon resonant midinfrared detector," *Appl. Phys. Lett.* **95**, 161101 (2009).
5. C. C. Chang, Y. D. Sharma, Y.-S. Kim, J. A. Bur, R. V. Shenoi, S. Krishna, D. Huang, and S.-Y. Lin, "A surface Plasmon enhanced infrared photodetector based on InAs quantum dots," *Nano Lett.* **10**, 1704-1709 (2010).
6. S. C. Lee, S. Krishna, and S. R. J. Brueck, "Quantum dot infrared photodetector enhanced by surface plasmon wave excitation," *Opt. Exp.* **17**, 23160-23168 (2009).
7. S. R. J. Brueck, "Optical and Interferometric Lithography-Nanotechnology Enablers," *Proc. IEEE* **93**, 1704-1721 (2005).
8. Z. Ku and S. R. J. Brueck, "Comparison of negative refractive index materials with circular, elliptical and rectangular holes," *Opt. Express* **15**, 4515-4522 (2007).
9. D. Xia, Z. Ku, S. C. Lee, and S. R. J. Brueck, "Nanostructures and Functional Materials Fabricated by Interferometric Lithography," *Adv. Mater.* to be published.
10. E. A. Shaner, J. G. Cederberg, and D. Wasserman, "Electrically tunable extraordinary optical transmission gratings," *Appl. Phys. Lett.* **91**, 181110 (2007).
11. W. L. Barnes, A. Dereux, and T. W. Ebbesen, "Surface plasmon subwavelength optics," *Nature* **424**, 824-830 (2003).
12. CST Studio Suite 2006B, <[www.cst.com](http://www.cst.com)>.
13. M. G. Moharam and T.K. Gaylord, "Rigorous coupled-wave analysis of planar-grating diffraction," *J. Opt. Soc. Am.* **71**, 811-818 (1981).
14. B. K. Minhas, W. Fan, K. Agi, S. R. J. Brueck, and K. J. Malloy, "Metallic inductive and capacitive grids: theory and experiment," *J. Opt. Soc. Am. A* **19**, 1352-1359 (2002).

15. M. A. Ordal, L. L. Long, R. J. Bell, S. E. Bell, R. R. Bell, R. W. Alexander, and C. A. Ward, "Optical properties of the metals Al, Co, Cu, Au, Fe, Pb, Ni, Pd, Pt, Ag, Ti and W in the infrared and far infrared," *Appl. Opt.* **22**, 1099 (1983).

16. J. Rosenberg, R. V. Shenoi, S. Krishna, and O. Painter, "Design of plasmonic photonic crystal resonant cavities for polarization sensitive infrared photodetectors," *Opt. Express* **18**, 3672-3686 (2010).